The Pennsylvania State University
The Graduate School
Department of Mechanical and Nuclear Engineering

VEHICLE ROLLOVER PREDICTION FOR BANKED SURFACES

A Dissertation in
Mechanical Engineering
by
Sittikorn Lapapong

Submitted in Partial Fulfillment
of the Requirements
for the Degree of

Doctor of Philosophy

December 2010

The thesis of Sittikorn Lapapong was reviewed and approved* by the following:

Sean N. Brennan
Associate Professor of Mechanical Engineering
Dissertation Advisor, Chair of Committee

Henry J. Sommer III
Professor of Mechanical Engineering

Christopher D. Rahn
Professor of Mechanical Engineering

Eric T. Donnell
Assistant Professor of Civil Engineering

Karen A. Thole
Professor of Mechanical Engineering
Head of the Department of Mechanical and Nuclear Engineering

*Signatures are on file in the Graduate School.

Abstract

Rollover accidents are one of the leading causes of death on the highway due to their very high fatality rate. A key challenge in preventing rollover via chassis control is that the prediction of the onset of rollover can be quite difficult, especially in the presence of terrain features typical of roadway environments. These road features include superelevation of the road (e.g. road bank), the median slope, and the shoulder down-slope. This work develops a vehicle rollover prediction algorithm that is based on a kinematic analysis of vehicle motion, a method that allows explicit inclusion of terrain effects. The solution approach utilizes the concept of zero-moment point (ZMP) that is typically applied to walking robot dynamics. This concept is introduced in terms of a lower-order model of vehicle roll dynamics to measure the vehicle rollover propensity, and the resulting ZMP prediction allows a direct measure of a vehicle rollover threat index. Both simulation and field experimental results show the effectiveness of the proposed algorithm during different road geometry scenarios and driver excitations.

Table of Contents

Chapter 6

Appendix A

Appendix B

List of Figures

List of Tables

Acknowledgments

Firstly, I would like to thank all the Thai taxpayers who have funded my higher education through the Thailand's Ministry of Science and Technology. I am very honored to receive this scholarship, and now I am looking forward to serving you all.

I am grateful to my advisor, Dr. Sean Brennan, for allowing me to work in his research group and letting me have intellectual freedom to pursue my passion. I greatly appreciate his mentoring during my six-year involvement in the group. I also would like to thank Dr. H.J. Sommer III, Dr. C.D. Rahn, and Dr. E.T. Donnell for their collaboration and support.

Thanks to the Thomas D. Larson Pennsylvania Transportation Institute and the Department of Mechanical and Nuclear Engineering for facilities and funding that I used to conduct my experiments.

Million thanks to fellow control-freaks, especially Alex, Pramod, and Kshitij. You guys are like my family members. Alex's help was crucial in conducting all the rollover tests. He might be the only group member who had the guts to pull the "trigger". Without his support, this thesis could not have been completed. Pramod, he has changed my view of the world. Kshitij, I do not know why, but I like to annoy you whenever you are around.

To my friends from all throughout my life, particularly those at Penn State, thank you for your invaluable friendship. I really appreciate it!!! Special thanks to P'Jum for his unquestionable support.

I would like to thank all my teachers to date who have given me such a strong intellectual foundation. I would also like to express my gratitude to Prof. Weerachai Kaensup, Prof. Djitt Laowattana, and Prof. Siam Charoenseang of King Mongkuts University of Technology Thonburi. I am whom I am because of their advice.

To my girlfriend, Gade. You are the most wonderful person in the world. Thanks for your warm love, care, encouragement, and support. I would not be where I am now without you.

Finally, I would like to thank my family who always stands beside me, motivates me at every step of my life, and supports my pursuits with complete resolve.

Dedication

To my mom, Oranuch Lapapong.

Chapter 1

Introduction

Vehicle rollover is one of the major causes of injury and death in motor vehicle accidents. As a consequence of more people traveling on highways each year and increasing numbers of Sport Utility Vehicles (SUVs) and large trucks which are typically more rollover-prone than conventional passenger cars, the number of people injured and lives claimed by rollover incidents is also increasing. One of the first steps in the effort to prevent vehicle rollover is to predict when the incident is imminent. This thesis utilizes a technique called the Zero-Moment Point (ZMP) to predict the onset of vehicle rollover. Rollover threat indices are derived based on two different types of vehicle models with the inclusion of terrain beneath the vehicle. The fidelity of the indices is then confirmed by various simulations and field experiments under different vehicle excitations on several road profiles.

1.1 Motivation

According to the U.S. Department of Health and Human Services [1], motor vehicle accidents are the leading cause of death in the United States when causes of death by disease are not included. In 2007, automobile crashes claimed 41,059 lives, and 2,491,000 people were injured in 6,024,000 police-reported motor vehicle traffic crashes [2]. These reports reveal that 8,940 out of 41,059 lives were lost in rollover accidents, indicating that vehicle rollover is one of the major causes of death for highway accidents. To reduce the number of deaths due to vehicle rollover accidents, it is very important to improve vehicle safety, especially roll stability of the vehicle.

The first rollover testing involving automobiles ever recorded were conducted at a GM testing facility in 1934 [3]. At that time, the tests primarily focused on the structural integrity of vehicles. The work since then has increasingly focused on measuring and predicting vehicle rollover propensity to produce rollover threat metrics that are useful for predicting rollover onset, thus providing a measurement for indicating a rollover-prone vehicle, for alerting the driver during a rollover-prone situation, or even for active chassis control to prevent rollover. In an attempt to predict vehicle rollover propensity, rollover threat metrics that have been found in the literature can be categorized as follows: static or steady-state rollover metrics, dynamic rollover metrics, rollover metrics based on thresholds of vehicle states or combinations of the vehicle states, rollover metrics based on forces acting on tires or moments generated by those forces, and energy-based rollover metrics. Moreover, there were many studies that aimed to understand mechanisms behind vehicle rollover and were concurrent with above efforts.

Examples of static or steady-state rollover metrics include the Static Stability Factor (SSF) [4, 5], the Side-Pull Ratio (SPR) [4, 5], the Tilt-Table Ratio (TTR) [4, 5], the centrifuge test [5], the Bickerstaff's rollover index [6], and related rollover thresholds for a suspended vehicle model [7]. These metrics codify rollover propensity as a ratio between a force that attempts to roll a vehicle over and a force that attempts to recover the vehicle in a static equilibrium or steady-state turning in which the vehicle is about to rollover, e.g. forces acting on tires on one side of the vehicle are equal to zero. The Static Stability Factor (SSF) [4, 5] is the most common rollover metric used to study vehicle rollover propensity. Furthermore, this metric has been adopted by the National Highway Traffic Safety Administration (NHTSA)'s rating system for rollover resistance [5]. The SSF is the lateral acceleration in g's at which a vehicle will roll over on a flat road in a steady-state turn. The scenario of this situation is illustrated in Figure 1.1. In case of the assumption of the vehicle behaving as a rigid body (no suspension, tires with on compliances, and sufficient tire/road friction), the SSF is defined as one half of the average front and rear track width divided by the total vehicle center of gravity height [4, 5]. To obtain the SSF for the rigid vehicle model, the moment equation about the center of the right tire/road contact patch (point P in Figure 1.1) is

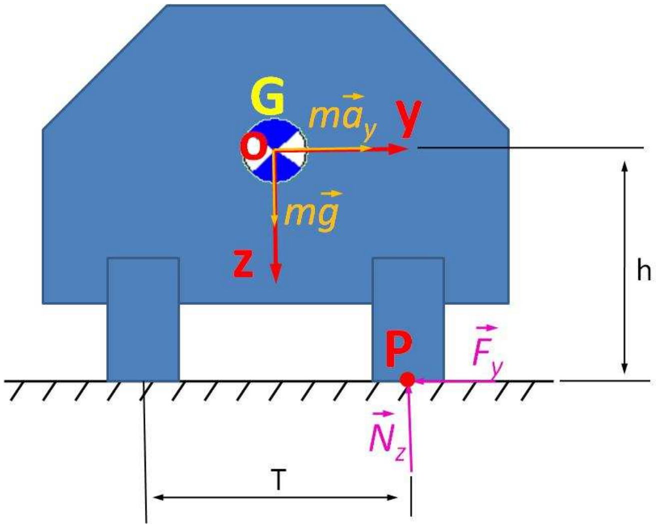

Figure 1.1: Free-body diagram of vehicle in steady-state turning and about to rollover.

considered and can be expressed as:

$$\sum M_P = ma_y h - mg\frac{T}{2} = 0 \tag{1.1}$$

Rearranging the above equation leads to:

$$SSF = \frac{a_y}{g} = \frac{T}{2h} \tag{1.2}$$

In the above equation, a_y is the steady-state acceleration, g is the gravitational acceleration, T is the average of the front and rear track widths of the vehicle, and h is the height of the vehicle's center of gravity from ground.

Illustrated in Figure 1.2, the side-pull test setup is used to measure the Side-Pull Ratio (SPR). The test was introduced by General Motors in 1960's [4]. The setup simulates a steady-state cornering that induces a lateral acceleration by pulling a vehicle laterally at the total vehicle center of gravity. The test is quasi-static. A force that lifts wheels off the ground on the far side is recorded, and the ratio between the force and its own vehicle weight is the SPR.

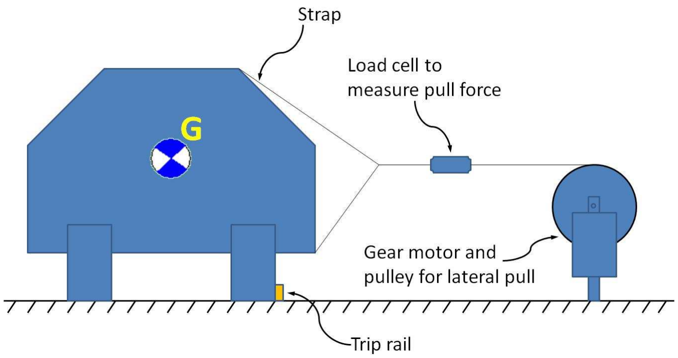

Figure 1.2: Simplified side-pull setup.

The Tilt-Table Ratio (TTR) [4, 5] is determined by a tilt-table setup shown in Figure 1.3. The purpose of the tilt-table setup is to simulate a lateral acceleration required to cause vehicle rollover. The vehicle is positioned at rest on the tilt table, and the table is tilted up until the vehicle is about to rollover. The TTR is defined as a ratio between a force that tries to roll over a vehicle and a force that tries to recover the vehicle from rollover. From static equilibrium, the TTR, which is expressed in Eq. 1.3, is the tangent of the angle of the when the front and rear wheels on the uphill side of the vehicle first lift up [5].

$$TTR = \frac{mg\sin\phi_t}{mg\cos\phi_t} = \tan\phi_t \tag{1.3}$$

In Eq. 1.3, m is the vehicle mass, g is the gravitational acceleration, and ϕ_t is the tilt table's inclination angle at which the vehicle almost rolls over. If the suspensions and tires of the vehicle are assumed to be rigid, the TTR will be the same as the SSF.

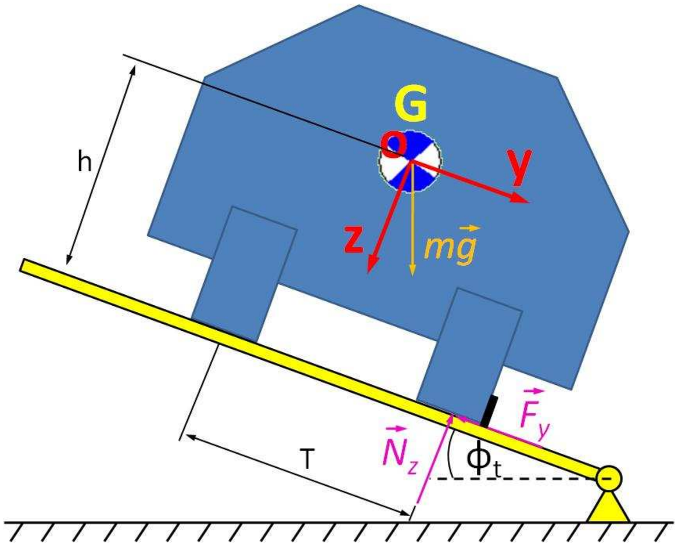

Figure 1.3: Tilt-table test.

The setup for a centrifuge test is presented in Figure 1.4. Like other setups, this setup is used to mimic the situation of steady-state cornering. To perform a centrifuge test, a vehicle is placed on a level platform. Once the platform rotates, the vehicle is subject to the lateral acceleration field. If the acceleration is high enough, the vehicle will start rolling over.

In 1976, Bickerstaff [6, 8] proposed a rollover index that is empirically valid for a range of CG heights for light trucks. The rollover index is defined as the lateral acceleration in g's at which a vehicle is about to roll over on a flat road during steady-state turning. To determine the Bickerstaff's rollover index that is

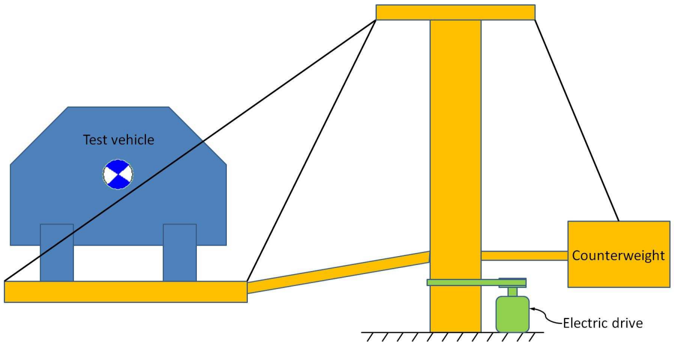

Figure 1.4: Centrifuge test.

hereafter called RI_B, a vehicle in Figure 1.5 is modeled similar to a vehicle roll model except the unsprung mass is ignored. The vehicle is divided into two parts: an unsprung mass and sprung mass. In the figure, point G is the overall vehicle

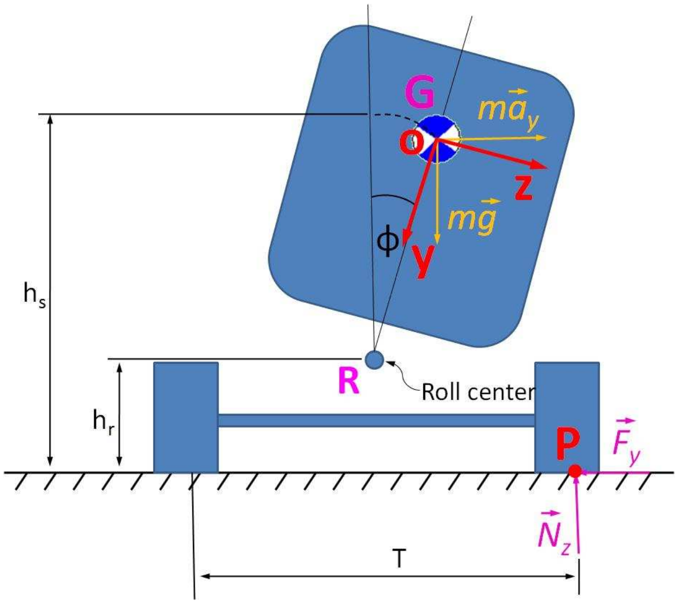

Figure 1.5: Free-body diagram of vehicle with suspension system in steady-state turning and about to rollover.

center of gravity, and point R is a roll center. The vehicle has a sprung-mass roll flexibility gradient γ, which is defined as:

$$\gamma = \frac{\phi}{a_y/g} \tag{1.4}$$

This roll flexibility gradient has the unit of rad/g's. Parameters h_r and h_s are the heights of the the roll center and the center of gravity, respectively. The track width of the vehicle is T. In the figure, the vehicle is assumed to perform a steady-state left turn. Lateral acceleration and gravitational acceleration are denoted by a_y and g, respectively. By taking moments about the center of the right tire/road contact patch (point P in Figure 1.5), we obtain:

$$\sum M_P = ma_y \left[h_r + (h_s - h_r)\cos\phi\right] - mg\left[\frac{T}{2} - (h_s - h_r)\sin\phi\right] = 0 \tag{1.5}$$

After applying the small-angle approximation ($\sin\phi \approx \phi$ and $\cos\phi \approx 0$) and the definition of the roll flexibility gradient in Eq. 1.4 and regrouping, the above equation results in the Bickerstaff's rollover index, which is:

$$RI_B = \frac{a_y}{g} = \frac{T}{2h_s}\left[\frac{1}{1 + \left(\frac{h_s - h_r}{h_s}\right)\gamma}\right] \tag{1.6}$$

The last steady-state rollover index considered here is the rollover threshold for the suspended vehicle model [7], which is shortly called RT_{SVM} from now on. The threshold is derived from a steady-state turning analysis. To obtain the threshold, a vehicle is modeled as illustrated in Figure 1.6. The vehicle has mass m, track

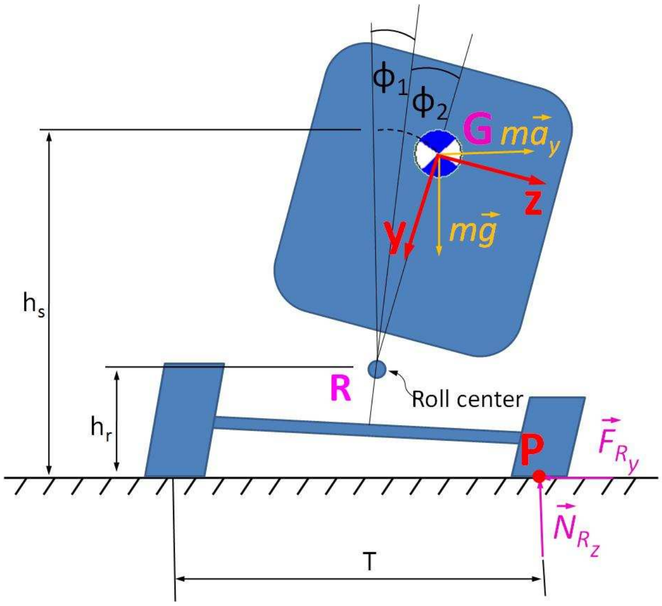

Figure 1.6: Free-body diagram of suspended vehicle near rollover.

width T, and height of the center of gravity h_s. The vehicle consists of an unsprung mass and sprung mass; however, the inertia of the unsprung mass of the vehicle is ignored. The vehicle body is supported on suspensions. In the figure, the vehicle is assumed to be steadily turning left on a flat road and is close to rollover. During the turn, due to an inertial force, the outside tires are being compressed, and the inside tires are being released, resulting in a deflection angle between the two sides of tires denoted by ϕ_1. The same effect of the inertia force also leads to another deflection angle between the left and right sides of the suspensions denoted by ϕ_2. a_y and g are the lateral acceleration and gravitational acceleration, respectively. Point R in the figure is a roll center of the vehicle. Its height is denoted by h_r. Summing moments about the center of right tire/road contact patch (point P in

Figure 1.6) leads to:

$$\begin{aligned}\sum M_P &= ma_y\left[h_r\cos(\phi_1)+(h_s-h_r)\cos(\phi_1+\phi_2)\right]\\ &\quad -mg\left[\frac{T}{2}-h_r\sin(\phi_1)-(h_s-h_r)\sin(\phi_1+\phi_2)\right]=0 \end{aligned} \tag{1.7}$$

By rearranging Eq. 1.7 and applying the small-angle approximation ($\cos(\phi_1) \approx \cos(\phi_1+\phi_2) \approx 1$, $\sin(\phi_1) \approx \phi_1$, and $\sin(\phi_1+\phi_2) \approx \phi_1+\phi_2$), the rollover threshold for the suspended vehicle is described as:

$$RT_{SVM} = \frac{a_y}{g} = \frac{T}{2h_s} - \phi_1 - \frac{(h_s-h_r)}{h_s}\phi_2 \tag{1.8}$$

There are certain inherent disadvantages in using these static or steady-state rollover metrics. First, obviously, since the metrics are derived from the static, quasi-static, or steady-state analyses, these metrics do not include the dynamic effects of the vehicle into consideration. Moreover, according to NHTSA [5], it is possible to artificially improve the outcomes of the tests, particularly in the side-pull, tilt-table, and centrifuge tests, with suspension modifications that degrade vehicle directional stability. Another issue with these types of static metrics is that the metrics do not provide an online warning capability that reflects driving inputs or road conditions. This issue can be addressed by using the vehicle states at a particular driving situation to anticipate rollover events.

To derive rollover metrics that are dynamic in nature, one can use rollover metrics that are based on the Newton's second law of motion. An example of the dynamic rollover metric is the the Dynamic Stability Index (DSI) [7]. The DSI is derived from the free-body diagram shown in Figure 1.7. In the figure, the vehicle is assumed to be a rigid body and is moving on a flat surface. The vehicle has the mass m, the x-axis mass moment of inertia I_{xx}, the track width T, and the height of the center of gravity h. One may also assume symmetries in all directions of the vehicle, resulting in negligible product mass moments of inertia. Further, the vehicle in the figure is assumed to make a left turn and is on the threshold of wheel lift; thus, there are no forces acting on the left tires. The moment equation about the center of the right tire/road contact patch (point P in Figure 1.7) is:

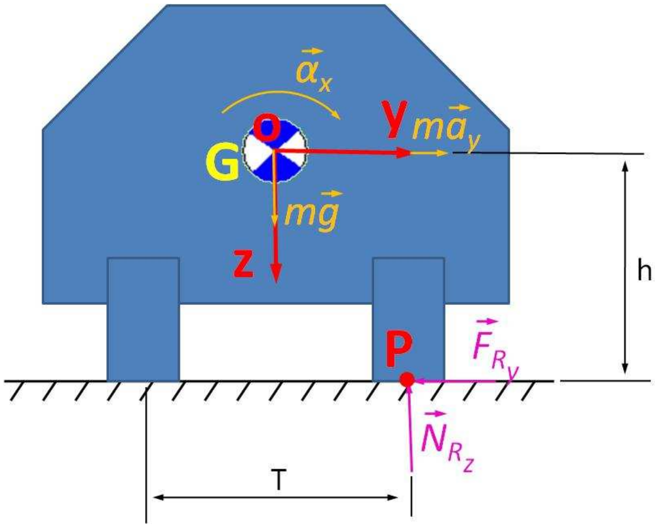

Figure 1.7: Free-body diagram of rigid vehicle model near rollover.

$$\sum M_P = -mg\frac{T}{2} + ma_y h = I_{xx}\alpha_x \tag{1.9}$$

where a_y is the lateral acceleration, α_x is the roll acceleration, and g is the gravitational acceleration. By rearranging the above equation, the DSI is defined as follows:

$$DSI = \frac{T}{2h} = \frac{a_y}{g} - \frac{I_{xx}\alpha_x}{mgh} \tag{1.10}$$

Often, vehicle states, for example, roll angle, roll rate, lateral acceleration, etc. or combinations thereof, are used to detect vehicle rollover either directly or with ad-hoc metrics. Wielenga [9, 10] used lateral acceleration as a rollover index and checked contact in rebound bumpers to sense wheel lift-off. Carlson and Gerdes [11] implemented a roll model controller that actively limits a peak roll angle of a vehicle. Yoon *et al.* [12] designed a rollover index that is a combination of states of roll angle, roll rate, lateral acceleration, and Time-To-Wheel-Lift (TTWL). In application to heavy vehicles, Gillespie and Verma [8] used a lateral acceleration that makes an outrigger to touch down as a dynamic rollover threshold. A group at the University of Cambridge in England designed an active roll control for a tanker based on a rollover threshold that is defined from a lateral acceleration limit [13, 14, 15]. Polkovics *et al.* [16] used a lateral acceleration threshold and difference in slip between two-sided wheels to detect rollover. Another rollover index [17] that is a combination of roll angle, roll rate, and lateral acceleration was introduced by Eisele and Peng.

Moreover, one can extend the prediction of vehicle states, forces, or moments into the future to anticipate rollover events. Examples include Chen and Peng who proposed the Time-To-Rollover (TTR) [18, 19, 20, 21, 22]. In their work, wheel liftoff is defined as an unacceptable rollover event. The TTR is the time that takes the vehicle's sprung mass to reach a critical roll angle by assuming the input steering angle stays constant at its current value during the time duration of prediction. The TTR is a model-based technique, relying on a 3-degree-of-freedom yaw-roll vehicle model.

Similarly, rollover metrics can be based on situation-dependent tire forces and/or moments. Examples include the Load Transfer Ratio (LTR) [23], the Stability Moment (SM) [24], and the indirect stability moment [24]. The LTR was defined by Ervin [23] at the University of Michigan Transportation Research Institute (UMTRI) in 1986. The LTR is a ratio of a difference of the normal forces on the right and left tires divided by the sum of the normal forces on the right and left tires, which is:

$$LTR = \frac{F_{z_R} - F_{z_L}}{F_{z_R} + F_{z_L}} \tag{1.11}$$

where F_z is the normal force acting on the tires, and subscripts R and L indicate the right and left tires, respectively. From the equation, one can see that the numerical value of the LTR can vary between -1 and 1. Once wheel liftoff occurs, the numerical value of the LTR is either -1 or 1, depending on which side of the vehicle lifts off. Since it is not trivial to measure the tire/ground interaction forces, a practical implementation of the LTR is still an issue. Hence, Odenthal *et al.* [25] proposed a technique to estimate the LTR from the equilibrium of vertical forces and roll moments. Another example of an indirect application of the LTR is the work done by Gaspar *et al.* [26] who designed an an observer-based rollover prediction algorithm. By using the similar concept, Peters and Iagnemma [24] developed the Stability Moment (SM), and used a ratio between the difference of the SMs on the left and right sides of a vehicle and the sum of the SMs on the left and right sides of the vehicle to predict vehicle rollover. The SM is a moment produced by wheel-terrain contact forces about every tip-over axis of the vehicle that does not pass through the forces' line of action [24]. The tip-over axis is defined as a line that connects between contact points. In the same work, due to the difficulty of measuring contact forces, Peters and Iagnemma also presented the indirect stability moment. The indirect stability moment is an estimation of the SM and is calculated from the general moment equation. Another example using moments would be the study by Cameron [27] who predicted a minimum steering angle that caused vehicle rollover by determining the existence of a slide-before-roll condition.

The next type of the rollover metric is obtained from the conservation of energy. Using conversion of energy and angular momentum, Jones introduced the Critical Sliding Velocity (CSV) [28, 29, 30, 5] in 1973. The CSV is the minimum lateral velocity required to tip a vehicle over when the vehicle is sliding sideways and impacting a low fixed obstacle such as a curb. To derive the CSV, consider Figure 1.8. The height of the curb and the thickness of the tires is negligible when compared the size of the vehicle. The critical sliding velocity is denoted by v_c. Since the angular momentum about point O is conserved during the impact, the following relation holds:

$$mv_ch = I_o\omega_o \tag{1.12}$$

where m is the vehicle mass, I_o is the roll-axis mass moment of inertia about the contact point (point O), ω_o is the angular velocity after the impact, and h is the height of the vehicle center of gravity from ground. In order for the vehicle to tip over with the minimum lateral velocity, the vehicle's center of gravity must rise vertically over the curb. After the impact, the rotational kinetic energy of the vehicle completely converts to the potential energy, leading to:

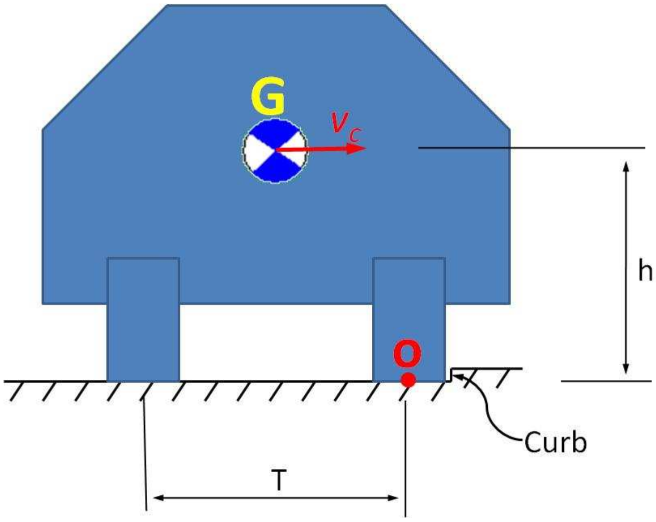

Figure 1.8: Vehicle sliding laterally and about to hit curb.

$$\frac{1}{2}I_o\omega_o^2 = mg\left(\sqrt{h^2+\frac{T^2}{4}}-h\right) \tag{1.13}$$

where T is the track width of the vehicle and g is the gravitational acceleration. By substituting the angular velocity from Eq. 1.12 into Eq. 1.13, the CSV is:

$$CSV = v_c = \sqrt{\frac{2I_o g}{mh}\left[\sqrt{1+\left(\frac{T}{2h}\right)^2}-1\right]} \tag{1.14}$$

Another energy-based metric is the Rollover Prevention Energy Reserve (RPER) [31, 32, 7], which is presented in Eq.1.15. The index is defined as the difference between the potential energy, E_v, required to bring a vehicle to its tip-over position and the sum of the instantaneous linear and rotational kinetic energy, E_k.

$$RPER = E_v - E_k \tag{1.15}$$

where

$$E_k = \frac{1}{2}mv^2 + \frac{1}{2}I_o p^2 \tag{1.16}$$

In Eq. 1.16, m, V, and p are the vehicle mass, the lateral velocity, and the roll rate, respectively. I_o is the mass moment of inertia about the axis about which the vehicle is rolling over. From Eq. 1.15, one can see that if the RPER is positive, the kinetic energy is not large enough to roll the vehicle over. Further, if the RPER is negative, the kinetic energy is beyond the potential energy needed to roll the vehicle over; hence, the rollover can occur. A concern about the RPER is that it is very conservative, since the vehicle that is sliding sideways is not always on the threshold of rollover, but often has sufficient kinetic energy to do so.

Also in this category, Choi [33] proposed a rollover potentiality index; however, to make the index practical, Choi also had a correction factor that is based on lateral acceleration. Dahlberg [34] applied the energy approach to commercial vehicles (e.g. a tractors-trailers). In this work, the idea of dynamic rollover energy margin was presented, wherein the potential energy of suspensions was included. To define an unstable equilibrium point in a multi-body system, Dahlberg identified a saddle point that gave the lowest non-zero value of a potential-energy function.

For a rollover metric to be useful, the prediction of rollover behavior needs to be accurate, particularly the onset of rollover such as tire lift. Since, referring to a National Highway Traffic Safety Administration (NHTSA)'s report [35], 75% of all fatal accidents took place off the road on which the terrain plays a significant role, this research differentiates itself from previous studies by including the effects of terrain and is therefore able to develop a more accurate tire-lift prediction. There are quite a few rollover metrics (load transfer ratio and stability moment) that concern the influences of the terrain; however, the implementation of those metrics is still an issue, since it is not easy to measure wheel/terrain contact tires on which these metrics are based. Additionally, once wheel liftoff occurs, the numerical values of these metrics saturate (be either -1 or 1) due to the ways that these metrics are defined. Under this circumstance, the metrics are deprived of the sense of the severity of the encountering rollover situation. To deal with these matters, a method used by walking robots called the Zero-Moment Point (ZMP) is adopted. The concept of ZMP is introduced later in Chapter 2.

1.2 Literature Review on Rollover Prevention Technologies

In order to mitigate vehicle rollover, there are four types of actuation mechanism for passenger cars proposed in the literature [21]: differential braking, active and/or four-wheel steering, active suspension, and active stabilizer. Douglas and Modlin [36] developed the Douglas stabilizer to prevent a vehicle from rollover during braking test situations. The stabilizer consists of a free-rolling wheel attached to a simple arm which is pivoted about the rear bumper. Introduced by Wielenga, the Anti-Rollover Braking (ARB) [9, 10] applied brakes on either an outside front wheel or both front wheels to generate a restoring torque that tries to straighten the vehicle's turn, which is basically the concept of differential braking. Moreover, Chen and Peng designed a time-to-rollover-based anti-rollover control algorithm that used differential braking as the primary means to prevent vehicle rollover [20, 21]. In 2000, BMW developed 'Dynamic Drive', which is an active roll stabilization system. This system allows a vehicle to withstand more lateral acceleration, improving rollover threshold [37]. Carlson and Gerdes [11] integrated steer-by-wire with differential braking to improve vehicle rollover propensity. Cameron

[27] used a steer-by-wire system incorporated with various filter techniques and model reference control to reduce a likelihood of wheel-lift. Yoon *et al.* presented a differential-braking control law designed by a direct yaw control method [12].

Similar technologies implemented in passenger cars have also been applied to heavy vehicles. Woodrooffe *et al.* [38] investigated the effects of a double drawbar dolly on a tractor-trailer combination and found out that the double drawbar dolly with appropriate steering system stiffness can reduce lateral acceleration, resulting in rollover mitigation of a tractor-trailer. Rakheja and Piché [39] developed an early warning safety device based on a microprocessor that can detect and warn drivers of impending dynamic instabilities of articulated freight vehicles. Dunwoody and Froese [40] proposed fifth-wheel and rear axle tilting mechanism as an active roll control system that can increase rollover threshold by up to 30% compared to the a tractor/semi-trailer with conventional suspension. Cebon *et al.* invented an active roll control system at each axle that consists of an anti-roll bar and a pair of hydraulic actuators [13, 41, 14, 15]. Polkovics *et al.* [16] implemented the Electronic Brake System (EBS) and the Drive Stability Control (DSC) system to prevent rollover in heavy vehicles. Eisele and Peng [17] applied differential braking to enhance roll stability of articulated heavy trucks. A combined control structure with active anti-roll bars and an active brake mechanism was presented by Gaspar *et al.* [26] to decrease the rollover risk of heavy vehicles.

1.3 Thesis Overview

The remainder of this thesis is organized as follows: Chapter 2 introduces the concept of the Zero-Moment Point (ZMP). The concept is then used to acquire a rollover threat index based on two different vehicle models that are explicitly aware of terrain. Furthermore, this chapter shows that some of the other existing rollover metrics in the literature are special cases of the ZMP-based rollover index when certain assumptions are applied. Chapter 3 contains the derivations of low-order dynamic models: a planar vehicle dynamic model and an out-of-plane vehicle dynamic model. These models are later used to validate vehicle parameters estimated in Chapter 4. Additionally, Chapter 4 focuses on measuring and estimating the values of the physical parameters of the test vehicle. These vehicle parameters are then extensively validated by the frequency-response technique, and the experimental validation results are shown in the chapter. In Chapter 5, the fidelity of the ZMP-based rollover threat index is investigated, first with simulations and later through field experiments. This chapter also provides an analysis on rollover mechanisms. Chapter 6 outlines the final conclusions and indicates the direction of future work.

Chapter 2

Zero-Moment Point (ZMP) and Its Application as Vehicle Rollover Threat Index

In this chapter, the concept of the Zero-Moment Point (ZMP) is introduced and applied as a vehicle rollover threat index that takes the effects of terrain into consideration. The rollover index is derived based on two different vehicle models and is then used to predict vehicle rollover propensity. In this work, wheel liftoff of both tires on one side of the vehicle is defined as the onset of an unwanted rollover situation. Moreover, this chapter provides proofs, showing that many of the rollover indices found in the literature are special cases of the ZMP-based rollover index when appropriate assumptions are considered.

2.1 Zero-Moment Point (ZMP)

The concept of Zero-Moment Point (ZMP) was developed and introduced by Vukobratovic in 1968 [42, 43, 44, 45]. This concept has been very useful and widely used in bipedal robotics research. Biped robotics scientists have applied the concept to preserve robots' dynamic balance during walking, or, in other words, to maintain stability of the robots, preventing the robots from overturning. For a bipedal walking robot to be dynamically stable, the location of the ZMP must lie within the support polygon. However, if the support polygon is not large enough to encompass the location of the ZMP to balance the action of external moments, this can result in the robot's overturning [45]. There are hundreds of biped walking robots today that employ an implementation of this algorithm, for instance, Honda's humanoid robots [46]. Moreover, many researchers have used the ZMP as a stability constraint for mobile manipulators to prevent the overturn of the mobile manipulators due to their own dynamics [47, 48, 49, 50, 51].

By definition, the zero-moment point is the point on the ground where the summation of the tipping moments acting on an object, due to gravity and inertia forces, equals zero. Here, the tipping moments are defined as the components of the moments that are tangential to the supporting surface [52]. This ZMP must be within the support polygon of the mechanisms; otherwise, this point does not physically exist. If the location of the ZMP is outside the support polygon, then it is considered as a Fictitious Zero-Moment Point (FZMP) [45]. Furthermore, it should be noted that the term ZMP can be considered as a misnomer, since the normal component of the moment generated by the inertia forces acting on an object is not necessarily zero. Hence, we should keep in mind that the term ZMP abridges the exact expression “zero tipping-moment point” [52].

2.1.1 Concept of Zero-Moment Point

The concept of zero-moment point is simple and intuitive. As defined at the beginning of this section, the zero-moment point is the point on the ground where the summation of the tipping moments acting on an object, due to gravity and inertia forces, equals zero. To explain this, let us consider an object that is at rest on a tilt table that has adequate friction as shown in Figure 2.1, assuming that there are no external forces acting on the object except gravity. The free-body diagrams of the object at various inclination angles are illustrated in Figure 2.2. In Figure 2.2(a), the tilt table is level; thus, to satisfy the conditions for the ZMP, the reaction force $\vec{N}$ must be at the center of the object, and the point where the reaction acts is the ZMP. When the tilt table is lifted up as shown in Figures 2.2(b), 2.2(c),

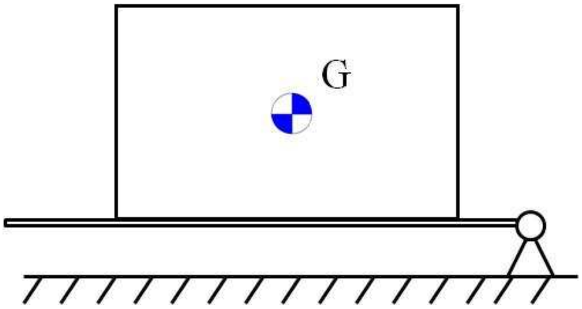

Figure 2.1: Mass at rest on a tilt table.

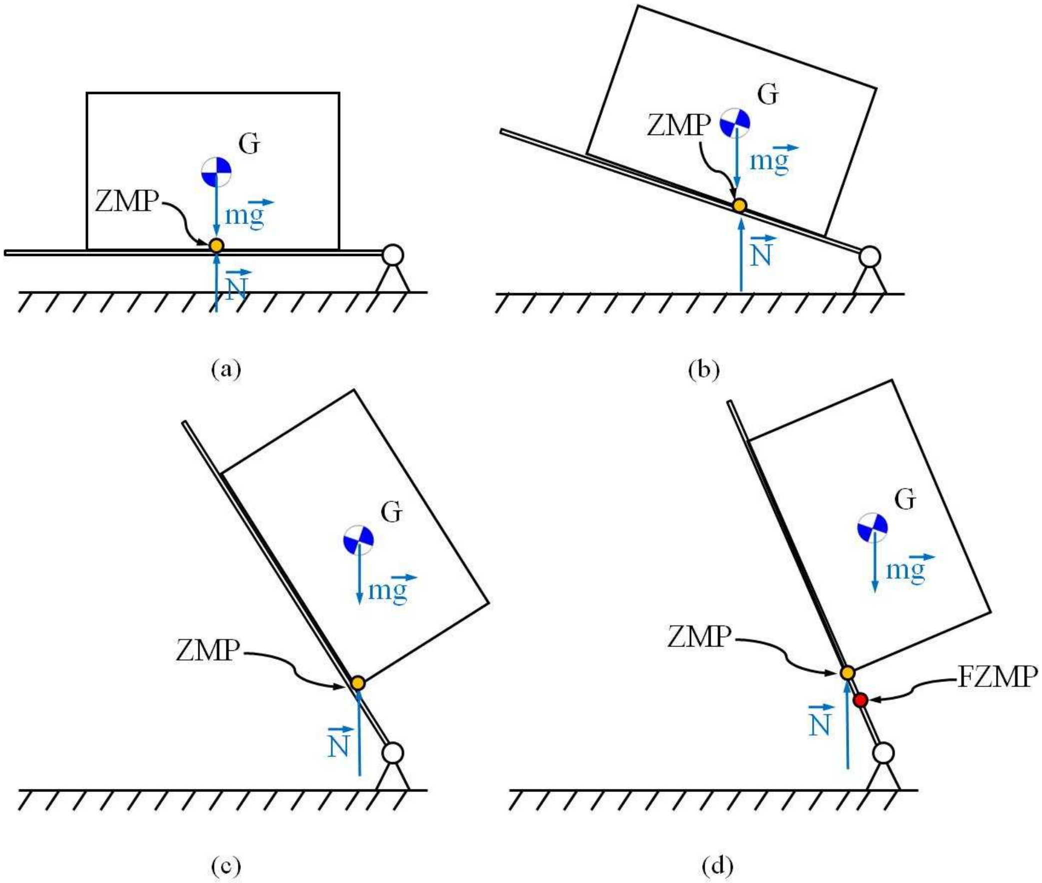

Figure 2.2: Free-body diagrams of the mass on the tilt table at different inclination angles.

and 2.2(d), the reactions must be shifted to the right-hand side to compensate the gravity-induced moments and to satisfy the ZMP conditions. Figure 2.2(c) is the situation right before the object losses the static-equilibrium conditions, and the location of the ZMP is on the edge of the object. Once the tilt table is lifted such that the location of the center of gravity of the object lies outside the base of the object as presented in Figure 2.2(d), the location of the ZMP will be outside the base of the mass. However, since it is impossible that the reaction may act outside the support of the object, this ZMP will be considered as a fictitious point known as a Fictitious Zero Moment Point (FZMP). The true location of the ZMP is still on the edge of the object. Under this situation (Figure 2.2(d)), it is obvious to see that the reaction moment produced by the reaction force cannot completely counteract the moment produced by its own weight, allowing the object to overturn.

2.1.2 General Formulation of Zero-Moment Point

To generalize the idea of the ZMP to a multi-body system, we note that, regardless of mass-to-mass constraint forces, the inertia forces of each mass in a body must be stabilized by a net moment on the ground surface. In Figure 2.3, the i$^{\text{th}}$ body of

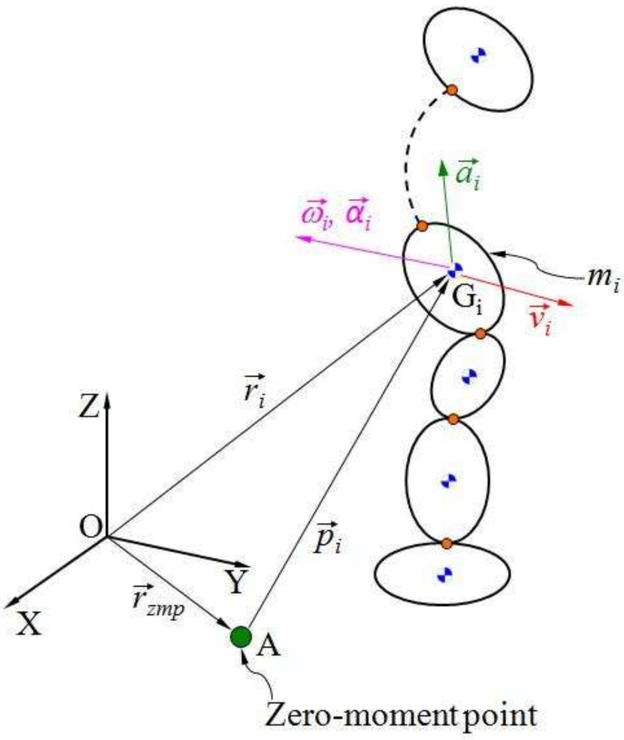

Figure 2.3: Kinematic chain.

the kinematic chain has a mass m_i and an inertia tensor $\mathbf{I}_i$ about its center of mass. The i$^{\text{th}}$ body is assumed to move with velocity $\vec{v}_i$ and acceleration $\vec{a}_i$ and to rotate at angular velocity $\vec{\omega}_i$ and angular acceleration $\vec{\alpha}_i$. The center of mass of the i$^{\text{th}}$ body relative to an inertial frame (OXYZ)is located by $\vec{r}_i$. Using general equations of motion [53, 54, 51] and D'Alembert's principle [30], the moment equation about point A induced by inertial forces and gravity is:

$$\vec{M}_A = \sum_i (\vec{p}_i \times m_i \vec{a}_i) + \sum_i (\mathbf{I}_i \vec{\alpha}_i + \vec{\omega}_i \times \mathbf{I}_i \vec{\omega}_i) - \sum_i (\vec{p}_i \times m_i \vec{g}) \tag{2.1}$$

where $\vec{p}_i = \vec{r}_i - \vec{r}_{zmp}$ and $\vec{g}$ is gravitational acceleration. If $\vec{M}_A = [0\ 0\ M_{A_z}]^{\text{T}}$, the point A becomes a zero-moment point.

2.1.3 Example of Application of Zero-Moment Point

To better understand the concept of the zero-moment point, the technique is applied to the situation in Figure 2.1 in which a block is at rest on a tilt table. Adequate surface friction is assumed so that the block does not slide down when the table is tilted. The block has the width w and the height of the center of gravity from the ground h. A tilt angle of the tilt table is denoted by ϕ. These parameters are also depicted in Figure 2.4. Point G is the center of gravity of the object. Point Q in the figure indicates the location of the zero-moment point. With the fact that the ZMP must be always maintained on the ground, the location vector

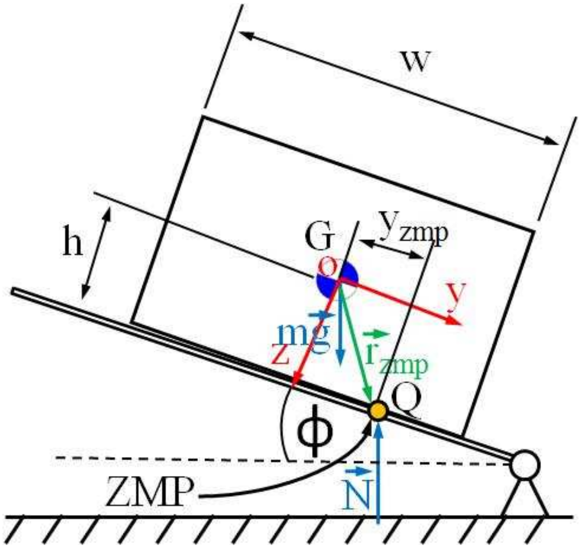

Figure 2.4: Free-body diagram of object on a tilt table.

of the ZMP may be expressed as:

$$\vec{r}_{zmp} = y_{zmp}\vec{j} + h\vec{k} \tag{2.2}$$

where $\vec{j}$ and $\vec{k}$ are unit vectors along the y- and z- axes, respectively. The gravitational acceleration with respect to the coordinates shown in Figure 2.4 is:

$$\vec{g} = g\sin(\phi)\vec{j} + g\cos(\phi)\vec{k} \tag{2.3}$$

Since the block is at rest and there is no external force exerting the block except the gravity, the linear and rotational velocities of the block are zero, leading to a reduced form of Eq. 2.1. The reduced equation can be presented as follows:

$$\vec{M}_Q = -\vec{p} \times m_i\vec{g} \tag{2.4}$$

where $\vec{p} = -\vec{r}_{zmp}$ because the coordinates are at the object's center of gravity. By substituting Eqs. 2.2 and 2.4 into Eq. 2.4 and setting $\vec{M}_Q = [0\ 0\ M_{Q_z}]^{\mathrm{T}}$, the $\vec{j}$ component of $\vec{r}_{zmp}$ can be found as:

$$y_{zmp} = h\tan(\phi) \tag{2.5}$$

2.2 Application of Zero-Moment Point as Vehicle Rollover Threat Index

This section details the application of the ZMP as a vehicle rollover metric. Two different types of vehicle models are introduced. These models explicitly include the effects of terrain. In this thesis, the definition of the terrain is a relatively smooth driving surface with any inclination, and that surface allows a simple tire/terrain interaction. The derivation of the location of the ZMP for the rigid vehicle model is developed first. In this model, the vehicle is modeled as a rigid body. Later in the section, the ZMP is applied to the other model that is called the vehicle roll model. The model contains two parts: sprung mass and unsprung mass. The sprung mass behaves as an inverted pendulum that sits on the unsprung mass, which is considered as a moving cart.

2.2.1 Derivation of Location of Zero-Moment Point for Rigid Vehicle Model

In this section, the concept of the zero-moment point is applied to a vehicle modeled as a rigid body shown in Figure 2.5. The vehicle model in the figure is assumed to have no suspension and compliance in its tires. Point Q in the figure is a zero-moment point on the ground plane located from the vehicle's center of gravity by $\vec{r}_{zmp}$. From the figure, the coordinates oxyz are fixed with the vehicle at the center of gravity of the vehicle (point G). The convention of the coordinates is defined by the Society of Automotive Engineering (SAE) [55]. The nomenclature used in this section is defined in Table 2.1, Figure 2.5, and Figure 2.6. The surface of the incline in Figure 2.6 is assumed to be relatively smooth and rigid.

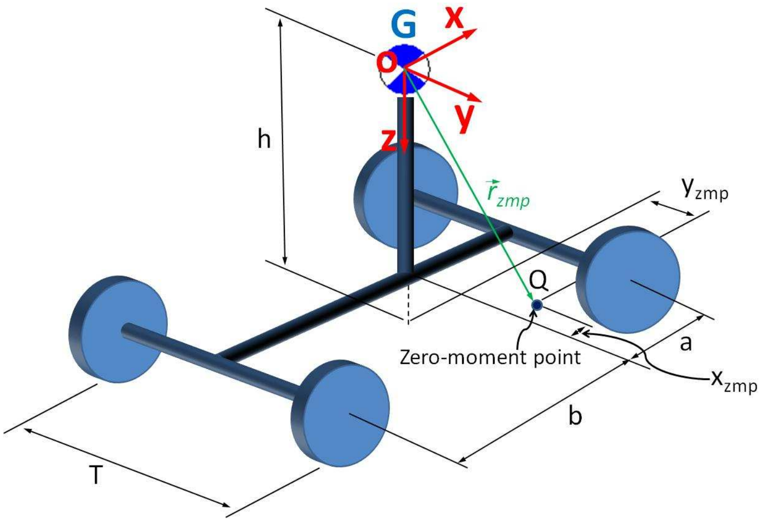

Figure 2.5: Rigid vehicle model.

To calculate the location of the zero-moment point, the angular velocities as

Table 2.1: Nomenclature used in derivation of location of zero-moment point for rigid vehicle model.

Symbol	**Definition**
m	mass of vehicle
a	distance from the center of gravity to the front axle along the x-axis
b	distance from the center of gravity to the rear axle along the x-axis
h	height of the center of gravity from ground
T	track width
I_{xx}	x-axis mass moment of inertia about the center of gravity
I_{yy}	y-axis mass moment of inertia about the center of gravity
I_{zz}	z-axis mass moment of inertia about the center of gravity
I_{xz}	mass product of inertia about the center of gravity
I_{yz}	mass product of inertia about the center of gravity
ϕ_r	roll angle of vehicle
ϕ_t	roll angle of terrain
θ	pitch angle of vehicle
ψ	yaw angle of vehicle
p	roll rate of vehicle
q	pitch rate of vehicle
r	yaw rate of vehicle
α_x	roll acceleration of vehicle
α_y	pitch acceleration of vehicle
α_z	yaw acceleration of vehicle
$a_{Gx,y,z}$	x-, y-, and z-axis accelerations at the center of gravity of vehicle
$\vec{i}$, $\vec{j}$, $\vec{k}$	unit vectors along the x-, y-, and z-axes

well as the linear and angular accelerations of the vehicle must be assumed. From the definition of the zero-moment point, one can see that its location must be defined on the ground so the z_{zmp}, which is the location of the ZMP along the z-axis, can be expressed in terms of vehicle properties, vehicle states, and terrain beneath the vehicle. Then, the location of the ZMP along the x- and y-axes (x_{zmp} and y_{zmp}) can be solved by using Eq. 2.1 in which the summations of moments about the x- and y-axes are equal to zero.

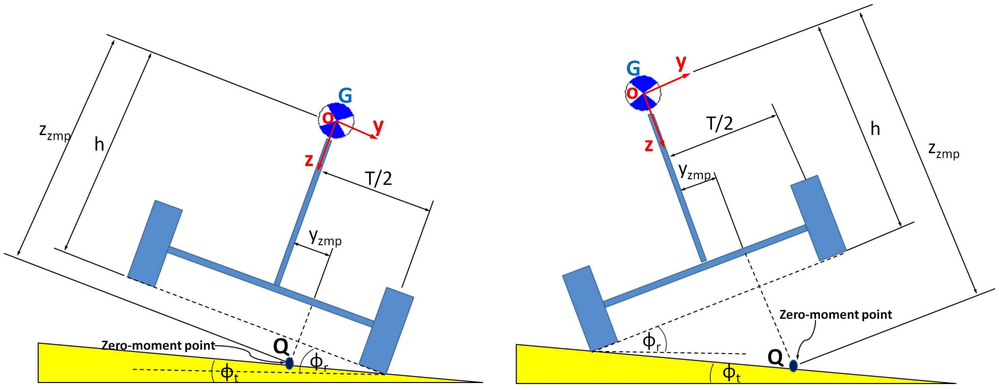

(a) (b)

Figure 2.6: Rigid vehicle model on terrain. (a) $\phi_r \geq \phi_t$ (b) $\phi_r < \phi_t$

The vehicle is free to move in any direction; thus, the angular velocity and acceleration of the vehicle about the center of gravity are as follows:

$$\vec{\omega} = p\vec{i} + q\vec{j} + r\vec{k} \tag{2.6}$$

$$\vec{\alpha} = \alpha_x\vec{i} + \alpha_y\vec{j} + \alpha_z\vec{k} \tag{2.7}$$

The vehicle's linear acceleration at the center of gravity can be written as:

$$\vec{a}_G = a_{Gx}\vec{i} + a_{Gy}\vec{j} + a_{Gz}\vec{k} \tag{2.8}$$

For simplicity, we assume that the vehicle is symmetric about the xz-plane ($I_{xy} =$

0); hence, the inertia tensor of the vehicle is:

$$\mathbf{I} = \begin{bmatrix} I_{xx} & 0 & -I_{xz} \\ 0 & I_{yy} & -I_{yz} \\ -I_{xz} & -I_{yz} & I_{zz} \end{bmatrix} \tag{2.9}$$

To include the effect of the rotating coordinates, the gravitational acceleration must be:

$$\begin{aligned} \vec{g} &= [\mathbf{R_x}(\phi_r)]\,[\mathbf{R_y}(\theta)]\,[\mathbf{R_z}(\psi)] \cdot \vec{g}_{Earth} \\ &= \begin{bmatrix} 1 & 0 & 0 \\ 0 & \cos(\phi_r) & \sin(\phi_r) \\ 0 & -\sin(\phi_r) & \cos(\phi_r) \end{bmatrix} \begin{bmatrix} \cos(\theta) & 0 & -\sin(\theta) \\ 0 & 1 & 0 \\ \sin(\theta) & 0 & \cos(\theta) \end{bmatrix} \\ &\quad \begin{bmatrix} \cos(\psi) & \sin(\psi) & 0 \\ -\sin(\psi) & \cos(\psi) & 0 \\ 0 & 0 & 1 \end{bmatrix} \begin{Bmatrix} 0 \\ 0 \\ g \end{Bmatrix} \\ &= -g\sin(\theta)\vec{i} + g\sin(\phi_r)\cos(\theta)\vec{j} + g\cos(\phi_r)\cos(\theta)\vec{k} \end{aligned} \tag{2.10}$$

where $[\mathbf{R_x}(\phi_r)]$, $[\mathbf{R_y}(\theta)]$, and $[\mathbf{R_z}(\psi)]$ are the rotation matrices about x-, y-, and z-axes, respectively. The sequence of the rotation is defined in the Society of Automotive Engineering's (SAE) standard [56]. The location of the zero-moment point is:

$$\vec{r}_{zmp} = x_{zmp}\vec{i} + y_{zmp}\vec{j} + z_{zmp}\vec{k} \tag{2.11}$$

To determine the location of the zero-moment point in the z-direction (z_{zmp}), let us consider Figure 2.6. From the figure, the rigid vehicle model rolls at the angle ϕ_r, and the roll angle of terrain at that instant is ϕ_t. It is obvious from the figure that the terrain will influence the parameter z_{zmp}. If $\phi_r \geq \phi_t$ (Figure 2.6(a)), the parameter z_{zmp} may be expressed in terms of vehicle parameters, vehicle states, and terrain as:

$$z_{zmp} = h + \left(\frac{T}{2} - y_{zmp}\right)\tan(\phi_r - \phi_t) \tag{2.12}$$

Similarly, if $\phi_r < \phi_t$ (Figure 2.6(b)), the parameter z_{zmp} is:

$$z_{zmp} = h + \left(\frac{T}{2} + y_{zmp}\right)\tan(-\phi_r + \phi_t) \tag{2.13}$$

Eqs. 2.12 and 2.13 can also be unified, which is:

$$z_{zmp} = h + \frac{T}{2}\left|\tan(\phi_r - \phi_t)\right| - y_{zmp}\tan(\phi_r - \phi_t) \tag{2.14}$$

Eq. 2.11 becomes:

$$\vec{r}_{zmp} = x_{zmp}\vec{\imath} + y_{zmp}\vec{\jmath} + \left[h + \frac{T}{2}\left|\tan(\phi_r - \phi_t)\right| - y_{zmp}\tan(\phi_r - \phi_t)\right]\vec{k} \tag{2.15}$$

Using the definition of the zero-moment point and Eq. 2.1, the general equation to locate the zero-moment point of the rigid vehicle model is:

$$M_{Q_z}\vec{k} = \vec{p} \times m\vec{a}_G + \mathbf{I}\vec{\alpha} + \vec{\omega} \times \mathbf{I}\vec{\omega} - \vec{p} \times m\vec{g} \tag{2.16}$$

where $\vec{r} = 0$ since the coordinates are located at the vehicle's center of gravity, and $\vec{p} = \vec{r} - \vec{r}_{zmp} = -\vec{r}_{zmp}$. Hence, by substituting Eqs. 2.6, 2.7, 2.8, 2.9, 2.10, and 2.15 into Eq. 2.16 and equating $\vec{i}$ and $\vec{j}$ components in Eq. 2.16 to zero, the location of the zero-moment point with respect to the coordinates can be expressed as follows:

$$\begin{aligned} x_{zmp} = & \left\{ \frac{1}{2m\left[-g\cos(\theta)\cos(\phi_r) + a_{Gz}\right]} \right\} \{ -2I_{xz}p^2 - 2I_{yz}pq - 2I_{yy}\alpha_y \\ & -2(I_{xx} - I_{zz})pr + 2I_{xz}r^2 + 2I_{yz}\alpha_z + 2mgh\sin(\theta) \\ & +mgT\left|\tan(\phi_r - \phi_t)\right|\sin(\theta) + 2mha_{Gx} + mTa_{Gx}\left|\tan(\phi_r - \phi_t)\right| \\ & + [\ (g\sin(\theta) + a_{Gx})\ (\ mT\left|\tan(\phi_r - \phi_t)\right|(-g\cos(\theta)\sin(\phi_r) + a_{Gy}) \\ & +2\ (\ I_{xx}\alpha_x - I_{xz}pq - I_{yz}q^2 - (I_{yy} - I_{zz})qr + I_{yz}r^2 - I_{xz}\alpha_z \\ & -mgh\cos(\theta)\sin(\phi_r) + mha_{Gy}\ )\ )\tan(\phi_r - \phi_t)\ ] \\ & /\left[g\cos(\theta)\cos(\phi_t)\sec(\phi_r - \phi_t) - a_{Gz} - a_{Gy}\tan(\phi_r - \phi_t)\right]\ \} \end{aligned} \tag{2.17}$$

$$\begin{aligned} y_{zmp} = & \{\ mg\cos(\theta)\sin(\phi_r)\left[T\left|\tan(\phi_r - \phi_t)\right| + 2h\right] - ma_{Gy}\left[T\left|\tan(\phi_r - \phi_t)\right| + 2h\right] \\ & -2I_{xx}\alpha_x + 2I_{xz}\alpha_z + 2I_{yz}(q^2 - r^2) + 2(I_{xz} + I_{yy} - I_{zz})qr\ \} \\ & /\ \{\ 2m\ [\ g\cos(\theta)\cos(\phi_t)\sec(\phi_r - \phi_t) - a_{Gy}\tan(\phi_r - \phi_t) - a_{Gz}\ ]\ \} \end{aligned} \tag{2.18}$$

We know that, in this work, the main focus is on vehicle rollover; thus, only the expression of y_{zmp} is necessary to determine vehicle rollover propensity. The expression of x_{zmp} is shown for the sake of completeness. The x_{zmp} will be very useful when considering longitudinal overturn of a vehicle. Additionally, it is useful to notice one of the advantages of the ZMP technique from the derivation process. Since the ZMP is a point on the ground, by summing the moments about this point, the moments induced by the longitudinal/lateral tire forces have no contributions to the tipping moments. Therefore, the proposed rollover prediction algorithm does not rely on any tire/terrain force models. The diagram in Figure 2.7 shows the flow of information that is necessary for the calculation of ZMP.

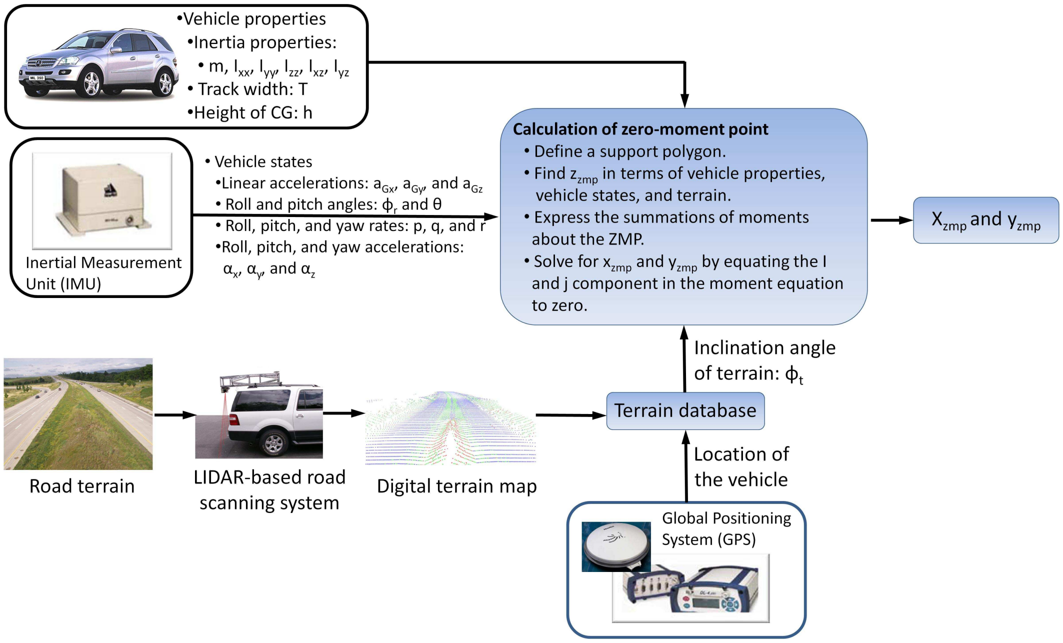

Figure 2.7: Information flow relevant to calculation of zero-moment point.

2.2.2 Derivation of Location of Zero-Moment Point for Vehicle Roll Model

In this section, a vehicle is modeled as illustrated in Figure 2.8. The vehicle consists of two parts: an unsprung mass and sprung mass. Both masses are linked together at the point called a roll center (point R in Figure 2.8). The roll center allows the sprung mass to rotate only in the roll direction (about the x-axis); thus, both unsprung mass and sprung mass have the same pitch and yaw rates as well as the same pitch and yaw accelerations. The sprung mass is supported by a roll spring (K_ϕ) and roll damper (D_ϕ) that represent the net effect of the vehicle's suspensions. In the figure, point G is the location of the whole vehicle's center of gravity (CG). Point $\mathrm{G_u}$ and point $\mathrm{G_S}$ are the center of gravity of the unsprung mass and sprung mass, respectively. The sprung mass's CG is located by $\vec{r}_s$. The

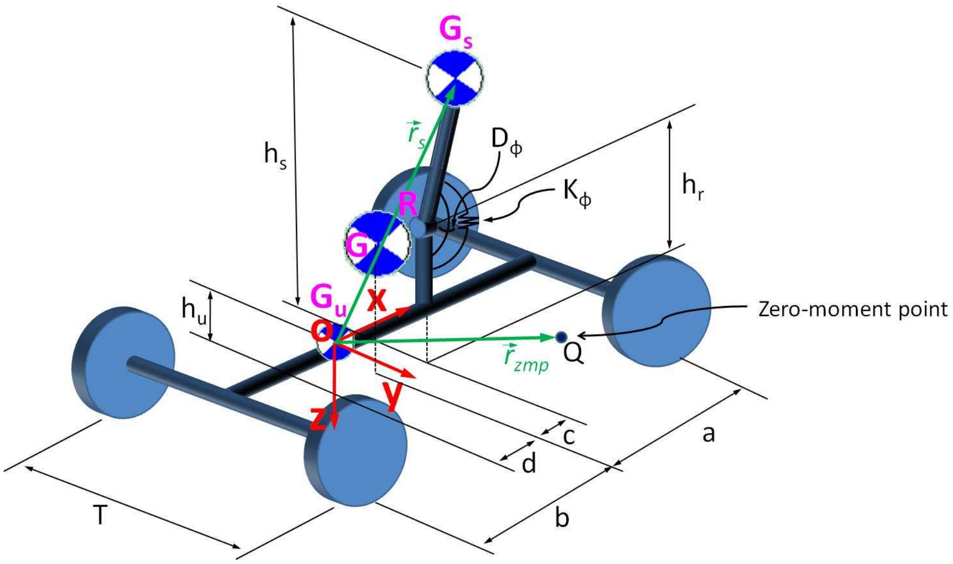

Figure 2.8: Roll model.

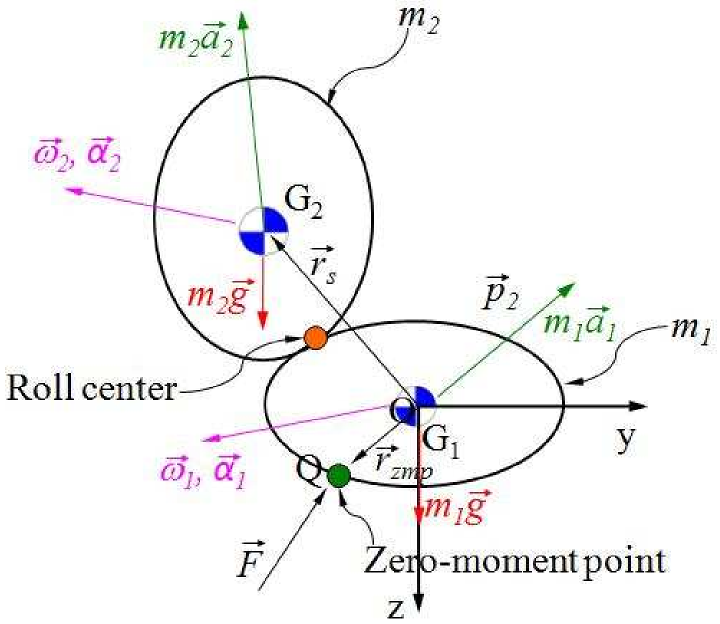

Figure 2.9: Free-body diagram of two-link kinematic chain.

coordinates (oxyz) are attached with the unsprung mass's center of gravity whose distance is d measured from the vehicle's CG. Point Q in the figure is the zero-moment point, which is located by $\vec{r}_{zmp}$. Without any loss of generality, the vehicle roll model can be simplified as a two-link kinematic chain shown in Figure 2.9 in which mass m_1 and mass m_2 respectively represent the unsprung mass and sprung mass. The notation used in the following derivations is defined in Table 2.2 and Figures 2.8, 2.10, and 2.11. In Figure 2.10, the driving surface of the incline allows a simple tire/terrain interaction such as no tire sinkage, no large tire deformation, etc.

With the assumption that the roll center kinematically constrains the movement of both unsprung and sprung masses in pitch and yaw directions, both masses

Table 2.2: Nomenclature used in derivation of location of zero-moment point for vehicle roll model.

Symbol	**Definition**
m_u	unsprung mass
m_s	sprung mass
a	distance from the center of gravity to the front axle along the x-axis
b	distance from the center of gravity to the rear axle along the x-axis
c	distance from the vehicle's center of gravity to the sprung mass's center of gravity along the x-axis
d	distance from the vehicle's center of gravity to the unsprung mass's center of gravity along the x-axis
h_u	height of the unsprung mass's center of gravity from ground
h_s	height of the sprung mass's center of gravity from ground
h_r	height of the roll center from ground
T	track width
$I_{xx_{u,s}}$	x-axis mass moment of inertia about the unsprung mass's and sprung mass's centers of gravity
$I_{yy_{u,s}}$	y-axis mass moment of inertia about the unsprung mass's and sprung mass's centers of gravity
$I_{zz_{u,s}}$	z-axis mass moment of inertia about the unsprung mass's and sprung mass's centers of gravity
$I_{xz_{u,s}}$	mass product of inertia about the unsprung mass's and sprung mass's centers of gravity
$I_{yz_{u,s}}$	mass product of inertia about the unsprung mass's and sprung mass's centers of gravity
ϕ_u	roll angle of unsprung mass
ϕ_s	roll angle of sprung mass
ϕ_t	roll angle of terrain
ϕ	relative roll angle $(\phi_s - \phi_u)$
θ	pitch angle of vehicle
ψ	yaw angle of vehicle
p_u	roll rate of unsprung mass
p_s	roll rate of sprung mass
q	pitch rate of vehicle
r	yaw rate of vehicle
α_{ux}	roll acceleration of unsprung mass
α_{sx}	roll acceleration of sprung mass
α_y	pitch acceleration of vehicle
α_z	yaw acceleration of vehicle
$a_{ux,y,z}$	x-, y-, and z-axis accelerations at the center of gravity of unsprung mass
$a_{sx,y,z}$	x-, y-, and z-axis accelerations at the center of gravity of sprung mass
$\vec{i}$, $\vec{j}$, $\vec{k}$	unit vectors along the x-, y-, and z-axes

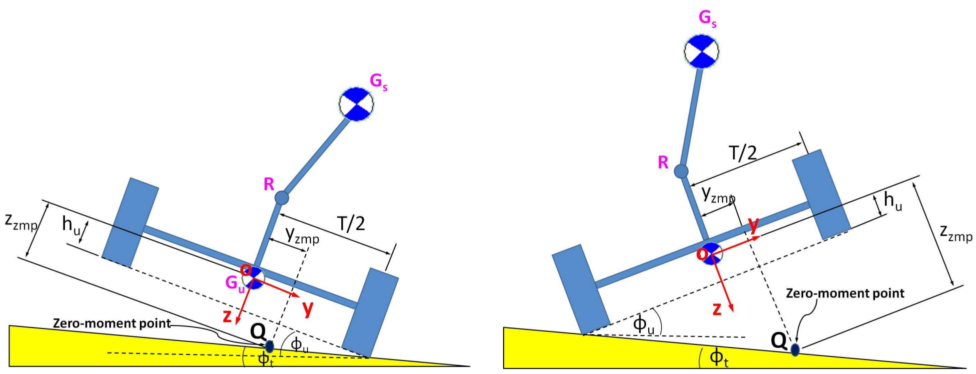

(a) (b)

Figure 2.10: Roll model on terrain. (a) $\phi_r \geq \phi_t$ (b) $\phi_r < \phi_t$

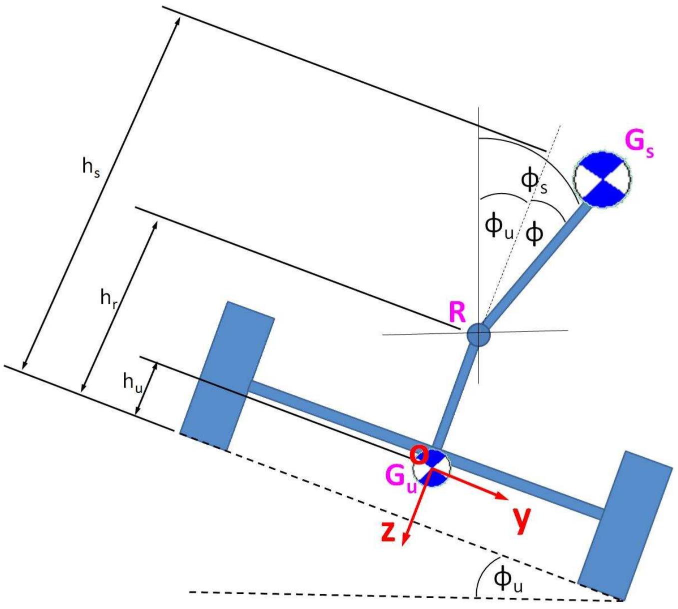

Figure 2.11: Parameters relevant to $\vec{r}_s$.

have the same pitch and yaw rates. The angular velocity and angular acceleration of the unsprung mass may be expressed as:

$$\vec{\omega}_u = p_u\vec{i} + q\vec{j} + r\vec{k} \tag{2.19}$$

$$\vec{\alpha}_u = \alpha_{ux}\vec{i} + \alpha_y\vec{j} + \alpha_z\vec{k} \tag{2.20}$$

The same assumption also leads to the angular velocity and angular acceleration of the sprung mass:

$$\vec{\omega}_s = p_s\vec{i} + q\vec{j} + r\vec{k} \tag{2.21}$$

$$\vec{\alpha}_s = \alpha_{sx}\vec{i} + \alpha_y\vec{j} + \alpha_z\vec{k} \tag{2.22}$$

The linear accelerations of the unsprung mass's CG (point $\mathrm{G_u}$) and the sprung mass's CG (point $\mathrm{G_s}$) can be respectively written as:

$$\vec{a}_{Gu} = a_{ux}\vec{i} + a_{uy}\vec{j} + a_{uz}\vec{k} \tag{2.23}$$

$$\vec{a}_{Gs} = a_{sx}\vec{i} + a_{sy}\vec{j} + a_{sz}\vec{k} \tag{2.24}$$

The inertia tensors of the unsprung and sprung masses are:

$$\mathbf{I}_u = \begin{bmatrix} I_{xx_u} & 0 & -I_{xz_u} \\ 0 & I_{yy_u} & -I_{yz_u} \\ -I_{xz_u} & -I_{yz_u} & I_{zz_u} \end{bmatrix} \tag{2.25}$$

$$\mathbf{I}_s = \begin{bmatrix} I_{xx_s} & 0 & -I_{xz_s} \\ 0 & I_{yy_s} & -I_{yz_s} \\ -I_{xz_s} & -I_{yz_s} & I_{zz_s} \end{bmatrix} \tag{2.26}$$

To take the effects of the rotating coordinates into account, the gravitational acceleration must be:

$$\vec{g} = -g\sin(\theta)\vec{i} + g\sin(\phi_u)\cos(\theta)\vec{j} + g\cos(\phi_u)\cos(\theta)\vec{k} \tag{2.27}$$

The location of the zero-moment point is:

$$\vec{r}_{zmp} = x_{zmp}\vec{i} + y_{zmp}\vec{j} + z_{zmp}\vec{k} \tag{2.28}$$

With the same fashion as in Eqs. 2.12, 2.13, and 2.11, Eq. 2.28 can be rewritten as:

$$\vec{r}_{zmp} = x_{zmp}\vec{i} + y_{zmp}\vec{j} + \left[h_u + \frac{T}{2}\left|\tan(\phi_u - \phi_t)\right| - y_{zmp}\tan(\phi_u - \phi_t)\right]\vec{k} \tag{2.29}$$

Using the definition of the zero-moment point, Eq. 2.1, and Figure 2.9, the general equation to locate the zero-moment point of the roll model is:

$$\begin{aligned} M_{Q_z}\vec{k} &= \vec{p}_u \times m_u\vec{a}_{G_u} + \mathbf{I}_u\vec{\alpha}_u + \vec{\omega}_u \times \mathbf{I}_u\vec{\omega}_u - \vec{p}_u \times m_u\vec{g} \\ &\quad + \vec{p}_s \times m_s\vec{a}_{G_s} + \mathbf{I}_s\vec{\alpha}_s + \vec{\omega}_s \times \mathbf{I}_s\vec{\omega}_s - \vec{p}_s \times m_s\vec{g} \end{aligned} \tag{2.30}$$

where $\vec{r}_u = 0$, $\vec{p}_u = \vec{r}_u - \vec{r}_{zmp} = -\vec{r}_{zmp}$, $\vec{r}_s = (c+d)\vec{i} + (h_s - h_r)\sin(\phi)\vec{j} + [h_u + h_r(\cos(\phi) - 1) - h_s\cos(\phi)]\,\vec{k}$, $\vec{p}_s = \vec{r}_s - \vec{r}_{zmp}$, and $\phi = \phi_s - \phi_u$. The parameters relevant to $\vec{r}_s$ are defined in Figure 2.11. Also, the definitions of the vectors in Eq. 2.30 are defined in Figure 2.8. Hence, by equating $\vec{i}$ and $\vec{j}$ components in Eq. 2.30 to zero, the location of the zero-moment point with respect to the coordinates can be expressed as follows:

$$
\begin{aligned}
x_{zmp} \;=\;& \{\, -2(I_{yy_s} + I_{yy_u})\alpha_y + 2(I_{xz_s} + I_{xz_u})r^2 + 2(I_{yz_s} + I_{yz_u})\alpha_z \\
& -2m_s g(c+d)\cos(\theta)\cos(\phi_u) + m_s(g\sin(\theta) + a_{sx})T\left|\tan(\phi_t - \phi_u)\right| \\
& +2m_s a_{sz}(c+d) + 4m_s(g\sin(\theta) + a_{sx})h_r \sin^2\left(\frac{\phi}{2}\right) \\
& +2m_s(g\sin(\theta) + a_{sx})h_s\cos(\phi) + m_u(g\sin(\theta) + a_{ux})T\left|\tan(\phi_t - \phi_u)\right| \\
& +2m_u(g\sin(\theta) + a_{ux})h_u - 2I_{yz_s}p_s q - 2(I_{xx_s} - I_{zz_s})p_s r - 2I_{xz_s}p_s^2 - 2I_{yz_u}p_u q \\
& -2(I_{xx_u} - I_{zz_u})p_u r - 2I_{xz_u}p_u^2 + [\,(m_s(g\sin(\theta) + a_{sx}) \\
& +m_u(g\sin(\theta) + a_{ux}))(T\left|\tan(\phi_t - \phi_u)\right|(m_s(g\cos(\theta)\sin(\phi_u) - a_{sy}) \\
& +m_u(g\cos(\theta)\sin(\phi_u) - a_{uy})) + 2((I_{yz_s} + I_{yz_u})q^2 + (I_{yy_s} + I_{yy_u} - I_{zz_s} \\
& -I_{zz_u})qr - (I_{yz_s} + I_{yz_u})r^2 + (I_{xz_s} + I_{xz_u})\alpha_z + m_s h_r(-2g\cos(\theta)\cos\left(\frac{\phi}{2} + \phi_u\right) \\
& \sin\left(\frac{\phi}{2}\right) - 2a_{sy}\sin^2\left(\frac{\phi}{2}\right) + a_{sz}\sin(\phi)) + m_s h_s(g\cos(\theta)\sin(\phi + \phi_u) \\
& -a_{sy}\cos(\phi) - a_{sz}\sin(\phi)) + m_u g h_u\cos(\theta)\sin(\phi_u) - m_u a_{uy}h_u + I_{xz_s}p_s q \\
& I_{xz_u}p_u q - I_{xx_s}\alpha_{sx} - I_{xx_u}\alpha_{ux}))\tan(\phi_t - \phi_u)\,]\,/\,[\,m_s(g\cos(\theta)\cos(\phi_t)\sec(\phi_t - \phi_u) \\
& -a_{sz} + a_{sy}\tan(\phi_t - \phi_u)) + m_u(g\cos(\theta)\cos(\phi_t)\sec(\phi_t - \phi_u) - a_{uz} \\
& +a_{uy}\tan(\phi_t - \phi_u))\,]\,\}\,/\,\{\,2m_s\left[-g\cos(\theta)\cos(\phi_u) + a_{sz}\right] \\
& +2m_u\left[-g\cos(\theta)\cos(\phi_u) + a_{uz}\right]
\end{aligned}
\tag{2.31}
$$

$$\begin{aligned} y_{zmp} \;=\;\; & \{\, m_s g \, [\, T \sin(\phi_u) \cos(\theta) \, |\tan(\phi_t - \phi_u)| - 4h_r \sin\left(\frac{\phi}{2}\right) \cos\left(\frac{\phi}{2} + \phi_u\right) \cos(\theta) \\ & + 2h_s \sin(\phi + \phi_u) \cos(\theta) \,] \\ & + m_u g \, [\, T \sin(\phi_u) \cos(\theta) \, |\tan(\phi_t - \phi_u)| + 2h_u \sin(\phi_u) \cos(\theta) \,] \\ & - m_s a_{sy} \, [\, T \, |\tan(\phi_t - \phi_u)| + 4h_r \sin^2\left(\frac{\phi}{2}\right) + 2h_s \cos(\phi) \,] \\ & - m_u a_{uy} \, [\, T \, |\tan(\phi_t - \phi_u)| + 2h_u \,] \\ & + 2m_s a_{sz} (h_r - h_s) \sin(\phi) - 2I_{xx_s} \alpha_{sx} - 2I_{xx_u} \alpha_{ux} + 2(I_{xz_s} + I_{xz_u}) \alpha_z \\ & + 2(I_{yz_s} + I_{yz_u}) q^2 - 2(I_{yz_s} + I_{yz_u}) r^2 + 2I_{xz_s} p_s q + 2I_{xz_u} p_u q \\ & + 2(I_{yy_s} + I_{yy_u} - I_{zz_s} - I_{zz_u}) q r \,\} \\ & / \{\, 2 \, [\, m_s (g \cos(\theta) \cos(\phi_t) \sec(\phi_t - \phi_u) - a_{sz} + a_{sy} \tan(\phi_t - \phi_u)) \\ & + m_u (g \cos(\theta) \cos(\phi_t) \sec(\phi_t - \phi_u) - a_{uz} + a_{uy} \tan(\phi_t - \phi_u)) \,] \,\} \end{aligned} \qquad (2.32)$$

As noted in Section 2.2.1, the expression of x_{zmp} is for the sake of completeness. The locations of the zero-moment point in both Sections 2.2.1 and 2.2.2 must also be transformed to the coordinates that are fixed to the terrain to make the applications practically sound. The terrain-fixed coordinates are illustrated in Figure 2.12 and denoted as the coordinates $\mathrm{o_1x_1y_1z_1}$. The origin of the coordinates is located at the middle of the track width of the vehicle. Also, as in the case of the rigid vehicle model, the ZMP-based rollover indices do not depend on any tire/terrain force models. This is because the moments induced by the longitudinal/lateral tire forces are not the components of the tipping moments, which is another advantage of this technique.

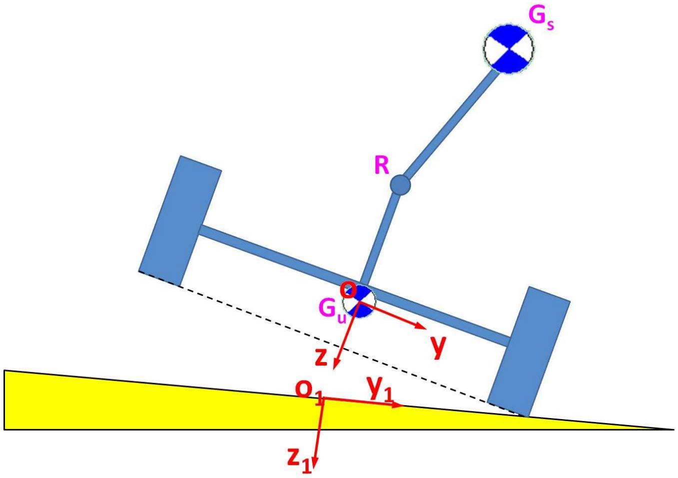

Figure 2.12: Terrain-fixed coordinate system.

2.3 Terrain Information

From Section 2.2, one can see that the knowledge of terrain profile is critical, especially the slope of the road (ϕ_t). Currently, there are many ways to obtain terrain information. One practical way is to use a light-detection-and-ranging (LIDAR) scanning system [57]. In this system, a LIDAR-equipped vehicle scans a road at a particular yaw angle and constructs a terrain database as shown in Figure 2.13. However, for the proposed rollover prediction algorithms described in Section 2.2, a yaw angle of a vehicle implementing the algorithms is not always the same as the one in the terrain database. Therefore, some kind of transformation is needed. The scenario of a vehicle running on a slope is illustrated in Figure 2.14 to facilitate the construction of the transformation. In this figure, the vehicle labeled

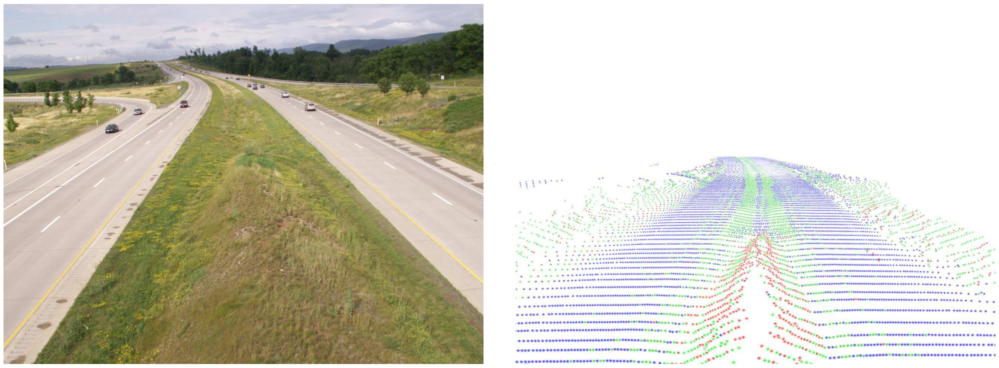
(a) (b)

Figure 2.13: LIDAR-generated map database. (a) Real scene. (b) Scene digitally generated by a LIDAR-scanning system.

as "vehicle implementing algorithms" is heading at the yaw angle ψ while, stored in the terrain database, the slopes of the road in the roll and pitch directions are ϕ_d and θ_d, respectively, with the map creator's heading direction of ψ_d (the subscript d stands for database.). The coordinates $\mathrm{O_1X_1Y_1Z_1}$ in Figure 2.14(c) are the global coordinates in which the $\mathrm{X_1}$-axis indicates the north. To simplify the derivation, the coordinates are set up at the middle of the left front tire/ground contact patch such that the y-axis is parallel to the slope, and fixed to the slope. Parameter T is the track width. The vector $\vec{n}$ in the figure is a unit vector that is perpendicular to the horizontal plane, and the vector $\vec{r}_E$ locates the center of the right contact patch from the coordinates oxyz. The angle ν is an angle between the vectors $\vec{n}$ and $\vec{r}_E$. The vector $\vec{n}$ may be expressed in terms of the terrain information (ϕ_d and θ_d) as:

$$\vec{n} = -\sin(\theta_d)\vec{i} + \sin(\phi_d)\cos(\theta_d)\vec{j} + \cos(\phi_d)\cos(\theta_d)\vec{k} \tag{2.33}$$

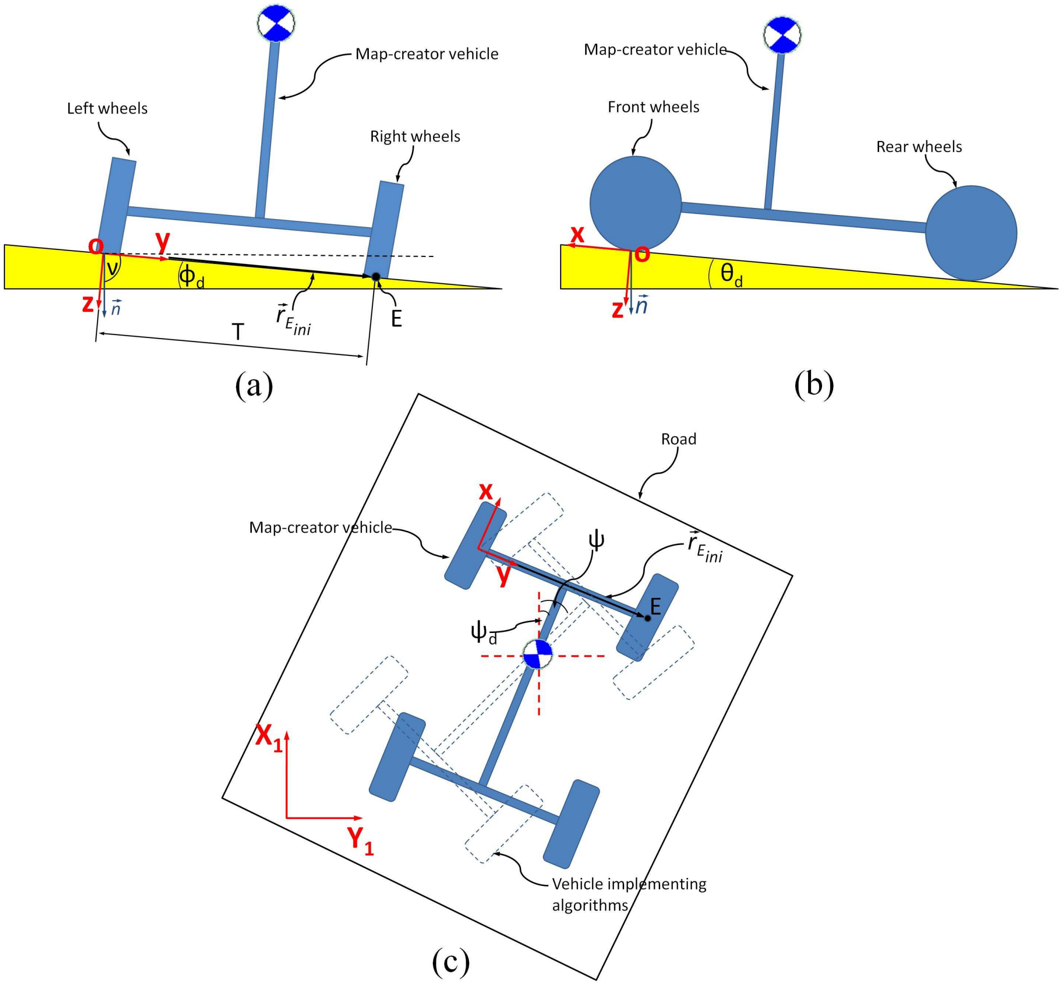

(a) (b)

(c)

Figure 2.14: Vehicle running on a slope. (a) Rear-viewed. (b) Side-viewed. (c) Top-viewed.

where $\vec{i}$, $\vec{j}$, and $\vec{k}$ denote unit vectors along the x-, y-, and z- axes, respectively. Initially, without any rotations, the vector $\vec{r}_E$ is called $\vec{r}_{E_{ini}}$ and can be written as:

$$\vec{r}_{E_{ini}} = T\vec{j} \tag{2.34}$$

After a rotation about the z-axis, the vehicle is heading at the yaw angle of ψ, and the vector $\vec{r}_E$ becomes:

$$\begin{aligned}\vec{r}_E &= \left[\mathbf{R_z}(\psi-\psi_d)\right]^{\mathrm{T}}\vec{r}_{E_{ini}} = \begin{bmatrix}\cos(\psi-\psi_d) & -\sin(\psi-\psi_d) & 0\\ \sin(\psi-\psi_d) & \cos(\psi-\psi_d) & 0\\ 0 & 0 & 1\end{bmatrix}\begin{Bmatrix}0\\ T\\ 0\end{Bmatrix}\\ &= \left[-T\sin(\psi-\psi_d)\right]\vec{i}+\left[T\cos(\psi-\psi_d)\right]\vec{j} \qquad (2.35)\end{aligned}$$

To find a slope at a particular yaw angle ψ, from the definition of dot product [58], the following relation may be expressed:

$$\sin(\phi_t) = \cos(\nu) = \frac{\vec{r}_E \cdot \vec{n}}{|\vec{r}_E|\,|\vec{n}|} \qquad (2.36)$$

Substitution of $\vec{r}_E$ and $\vec{n}$ into Eq. 2.36 leads to:

$$\phi_t = \arcsin\left[\sin(\psi-\psi_d)\sin(\theta_d)+\sin(\phi_d)\cos(\theta_d)\cos(\psi-\psi_d)\right] \qquad (2.37)$$

The above equation will be used later to calculate the slope of a road at any particular yaw angle.

2.4 Relationship Between the ZMP-Based Rollover Index Metric and Other Existing Rollover Metrics

In this section, the main effort is to show that, when applying assumptions specific for each existing rollover metric, the ZMP-based rollover index can be simplified to that particular rollover metric. The rollover metrics considered in this section include the Static Stability Factor (SSF), the Bickerstaff's rollover index (RI_B), the steady-state rollover threshold for a suspended vehicle (RT_{SVM}), and the Dynamic Stability Index (DSI). These metrics were introduced in Section 1.1.

2.4.1 Static Stability Factor (SSF)

The Static Stability Factor (SSF) [4, 5] is the lateral acceleration in g's at which a vehicle will roll over on a flat road in a steady-state turning. The scenario of this situation is illustrated in Figure 2.15. With the assumption that the vehicle is a rigid body, the SSF is derived in Eq. 1.2 and is recalled as follows:

$$SSF = \frac{a_y}{g} = \frac{T}{2h} \tag{2.38}$$

where a_y is the lateral acceleration, g is the gravitational acceleration, T is the track width of the vehicle, and h is the height of the vehicle's center of gravity

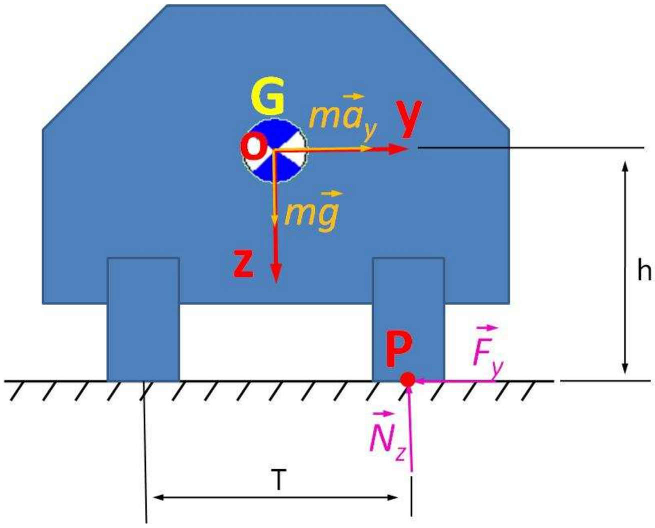

Figure 2.15: Free-body diagram of vehicle in steady-state turning and about to rollover.

from the ground.

Since the vehicle is modeled as a rigid vehicle, let us consider Eq. 2.18 to obtain the SSF from the ZMP-based rollover metric. From Figure 2.15, since the vehicle has no suspension systems and is performing a steady-state turn on the flat road (left turn), the roll and pitch angles of the vehicle are zero ($\phi_r = \theta = 0$), the roll angle of the terrain ($\phi_t = 0$), the roll and pitch rates and the roll, pitch, and yaw accelerations are zero ($p = q = \alpha_x = \alpha_y = \alpha_z = 0$), the linear acceleration in the z-axis is zero ($a_z = 0$), and the linear acceleration in the x-axis is less than zero ($a_y < 0$). Here, the mass product of inertia is ignored ($I_{yz} = 0$). Also, one knows that the right side of the wheels of the vehicle are about to lift off; thus, the constraint can be added that $y_{zmp} = \dfrac{T}{2}$. Substitution of these values into Eq. 2.18

yields the ZMP prediction for the lateral acceleration:

$$\frac{T}{2} = \frac{m a_y h}{m g} \tag{2.39}$$

By rearranging the above equation, the equation becomes:

$$SSF = \frac{a_y}{g} = \frac{T}{2h} \tag{2.40}$$

2.4.2 Bickerstaff's Rollover Index

The Bickerstaff's rollover index (RI_B) [6, 8] is defined as the lateral acceleration in g's at which a vehicle is about to roll over on a flat road during steady-state turning. The free-body diagram of the vehicle undergoing steady-state turning is illustrated in Figure 2.16. With the use of moment equation about point P in Figure 2.16, the Bickerstaff's rollover index can be expressed as:

$$RI_B = \frac{a_y}{g} = \frac{T}{2h_s}\left[\frac{1}{1 + \left(\frac{h_s - h_r}{h_s}\right)\gamma}\right] \tag{2.41}$$

In the above equation, most of the parameters are defined in Figure 2.16 except parameter γ. Parameter γ is the roll flexibility gradient of the vehicle and has the unit of rad/g's.

To derive the Bickerstaff's rollover index from the ZMP-based rollover index,

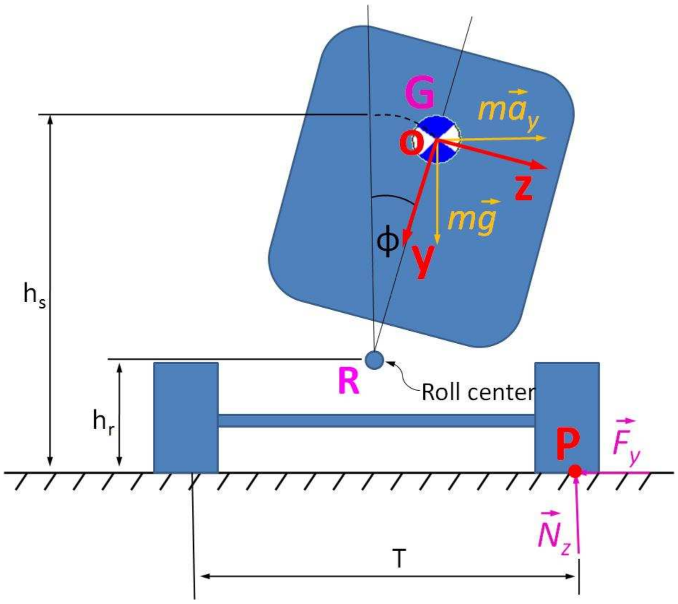

Figure 2.16: Free-body diagram of vehicle with suspension system in steady-state turning and about to rollover.

let us consider Eq. 2.32 of the vehicle roll model. From the derivation of the Bickerstaff's rollover index, one can see that the unsprung mass and all product mass moments of inertia are ignored ($m_u = I_{yz_s} = I_{yz_u} = 0$), the vehicle is performing steady-state left turn on a flat road ($a_{sy} < 0$ and $\phi_u = \phi_t = \theta = p_u = p_s = q = \alpha_{ux} = \alpha_{sx} = \alpha_z = a_{ux} = a_{uz} = a_{sx} = a_{sz} = 0$), and the vehicle is about to roll over ($y_{zmp} = \dfrac{T}{2}$). Substituting all these values into Eq. 2.32 again yields the ZMP relationship:

$$\frac{T}{2} = \frac{m_s h_r \left[-2g \sin\left(\dfrac{\phi}{2}\right) \cos\left(\dfrac{\phi}{2}\right) + 2a_{sy} \sin^2\left(\dfrac{\phi}{2}\right)\right] + m_s h_s \left(g \sin\phi + a_{sy} \cos\phi\right)}{m_s g} \tag{2.42}$$

After applying the definition of the roll flexibility gradient (Eq. 1.4), the the trigonometric identities ($\sin\phi = 2\sin\left(\frac{\phi}{2}\right)\cos\left(\frac{\phi}{2}\right)$ and $\sin^2\left(\frac{\phi}{2}\right) = \frac{1-\cos\phi}{2}$), and the small-angle approximation to Eq. 2.42 and then rearranging the equation, Eq. 2.42 gives the ZMP-predicted acceleration at the threshold of rollover:

$$RI_B = \frac{a_y}{g} = \frac{T}{2h_s}\left[\frac{1}{1+\left(\frac{h_s - h_r}{h_s}\right)\gamma}\right] \tag{2.43}$$

Again, there is a perfect agreement with published values.

2.4.3 Steady-State Rollover Threshold for Suspended Vehicle Model

The steady-state rollover threshold for the suspended vehicle model (RT_{SVM}) [7] is derived from steady-state turning, which is depicted in Figure 2.17. The threshold is recalled in Eq. 2.44. All parameters are defined in Figure 2.17. It is worth noting that, as a result of an inertial force, a deflection angle between the two sides of tires is denoted by ϕ_1. The same effect of the inertia force also leads to another deflection angle between the left and right sides of the suspensions denoted by ϕ_2.

$$RT_{SVM} = \frac{a_y}{g} = \frac{T}{2h_s} - \phi_1 - \frac{(h_s - h_r)}{h_s}\phi_2 \tag{2.44}$$

To analytically obtain this rollover threshold from the ZMP-based rollover in-

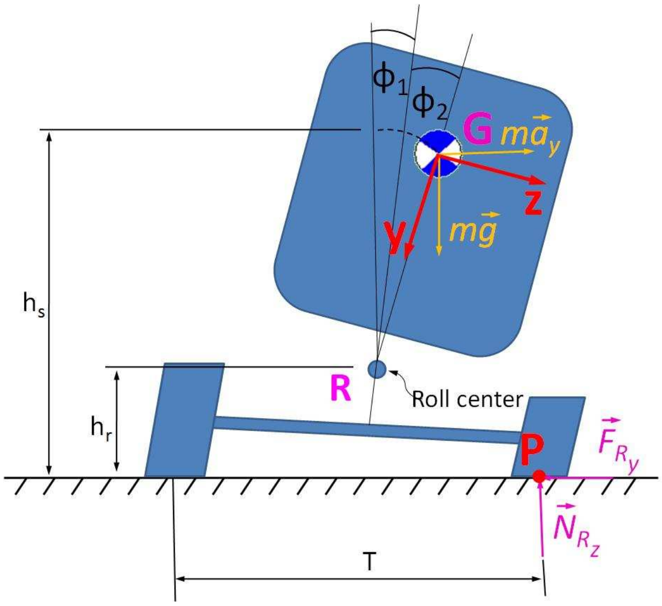

Figure 2.17: Free-body diagram of suspended vehicle near rollover.

dex, the rollover threshold for the suspended vehicle model will be a special case in which the angle ϕ_1 is equal to zero, since the roll model in Section 2.2.2 does not consider the deflection angle due to the tire compression and release. By applying the following assumptions: the unsprung mass and product mass moments of inertia are ignored ($m_u = I_{xz} = I_{yz} = 0$) and the vehicle is performing a steady-state left turn on the flat road near rollover ($y_{zmp} = \frac{T}{2}$, $a_{sy} < 0$, and $\phi_u = \phi_t = \theta = p_u = p_s = q = \alpha_{ux} = \alpha_{sx} = \alpha_z = a_{sx} = a_{sz} = 0$) to Eq. 2.32, Eq. 2.32 becomes:

$$\frac{T}{2} = \frac{h_r\left\{-g\sin(\phi_s) + a_{sy}\left[1-\cos(\phi_s)\right]\right\} + h_s\left[g\sin(\phi_s) + a_{sy}\cos(\phi_s)\right]}{g} \tag{2.45}$$

After applying the small-angle approximation ($\sin(\phi_s) \approx \phi_s$ and $\cos(\phi_s) \approx 1$), the above equation can be rewritten as:

$$RT_{SVM} = \frac{a_y}{g} = \frac{T}{2h_s} - \frac{h_s - h_r}{h_s}\phi_s \tag{2.46}$$

One can see that Eq. 2.46 is a special case of the rollover threshold for the suspended vehicle model in which the tires are assumed to be rigid (no deflection angle between two sides of tires).

2.4.4 Dynamic Stability Index (DSI)

The Dynamic Stability Index (DSI) [7] is derived from the free-body diagram shown in Figure 2.18. In the figure, the vehicle is assumed to be a rigid body and symmetrical in all directions, and the vehicle is moving on a flat surface. From the moment equation about the center of the right tire/road contact patch (point P in

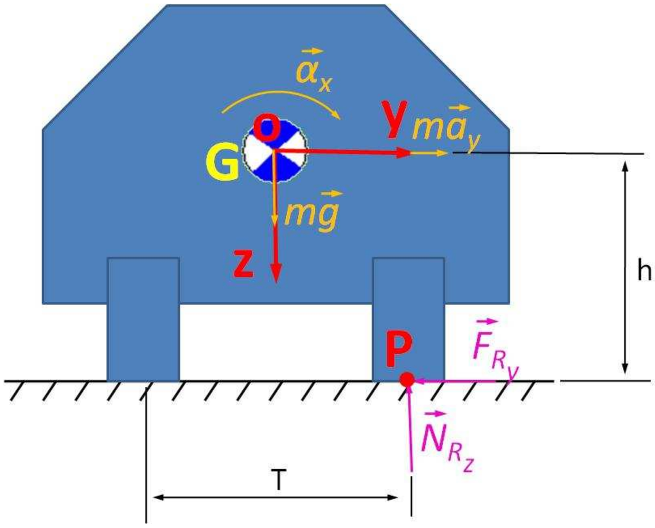

Figure 2.18: Free-body diagram of rigid vehicle model near rollover.

Figure 2.18), the DSI is presented as:

$$DSI = \frac{T}{2h} = \frac{a_y}{g} - \frac{I_{xx}\alpha_x}{mgh} \tag{2.47}$$

In the above equation, the vehicle has the mass m, the x-axis mass moment of inertia I_{xx}, the track width T, and the height of the center of gravity h. The lateral, gravitational, and roll accelerations are denoted by a_y, g, and α_x, respectively.

In order to obtain the DSI from the ZMP-based rollover index, Eq. 2.18 will be used, since the vehicle is assumed as a single rigid body. From the derivation of the DSI, the same following conditions are applied to the ZMP-based rollover index: the vehicle is symmetric in two directions of the vehicle ($I_{xz} = I_{yz} = 0$), the vehicle is running on the flat road ($\phi_r = \phi_t = \theta = a_{Gz} = q = \alpha_y = 0$), and the vehicle is turning left close to rollover ($y_{zmp} = \frac{T}{2}$, $\alpha_x > 0$, and $a_{Gy} < 0$). Substitution of the conditions into Eq. 2.18 leads to:

$$\frac{T}{2} = \frac{ma_{Gy}h - I_{xx}\alpha_x}{mg} \tag{2.48}$$

By rearranging the above equation, the DSI can be achieved from the ZMP relationship:

$$DSI = \frac{T}{2h} = \frac{a_y}{g} - \frac{I_{xx}\alpha_x}{mgh} \tag{2.49}$$

Chapter 3

Low-Order Vehicle Dynamic Models

In this chapter, two types of low-order linear vehicle dynamic models are developed by means of Newtonian-Eulerian mechanics: an in-plane vehicle dynamic model and an out-of-plane vehicle dynamic model. The in-plane vehicle dynamic model, also known as the two-degree-of-freedom model or the bicycle model, is a relatively simple model that describes vehicle planar dynamic characteristics by considering only lateral and yaw dynamics. This model is a well-known standard for studies of vehicle dynamics; however, it does not provide an understanding of vehicle's roll characteristics. To describe the vehicle's roll characteristics, the out-of-plane vehicle dynamic model is developed by modification of the in-plane dynamic model.

Table 3.1: Nomenclature used in derivation of bicycle model.

Symbol	**Definition**
m	vehicle mass
I_{zz}	z-axis mass moment of inertia about CG
a	distance from CG to front axle along the x-axis
b	distance from CG to rear axle along the x-axis
U	longitudinal velocity at CG
V	lateral velocity at CG
r	yaw rate
$\vec{F}_f$	front tire force
$\vec{F}_r$	rear tire force
$C_{\alpha f}$	front cornering stiffness
$C_{\alpha r}$	rear cornering stiffness
α_f	front slip angle
α_r	rear slip angle
δ_f	front steering angle

3.1 In-Plane Vehicle Dynamic Model: the Bicycle Model

The derivation of the in-plane vehicle dynamic model is elaborated in this section. The nomenclature used in the formulation process is indicated in Figure 3.1 and Table 3.1. Some of assumptions made to mathematically aid the derivation process for obtaining the model are listed below:

- All parts including wheels are rigid bodies.
- A left-right symmetry of forces is assumed, allowing a four-wheeled vehicle to be a bicycle-like vehicle.

- The vehicle is a front-wheel steering vehicle.
- There is no motion in the roll and pitch directions.
- The linear tire model is applied: $F = C_\alpha \alpha$. F is a lateral tire force, C_α is a cornering stiffness, and α is a slip angle. The slip angle is the angle between the center line of a tire and the direction that the tire is moving.
- The front slip angle α_f, rear slip angle α_r, yaw angle ψ, and front wheel steering angle δ_f are small so that the cosine of the angle is approximately one, and the sine of the angle is approximately the angle itself.
- The vehicle moves with constant longitudinal velocity.

As a consequence, a four-wheeled vehicle can be assumed to be well-represented by a bicycle-like vehicle (Figure 3.1), from which it derives its name, the bicycle model. In the free-body diagram, point O is the center of gravity of the vehicle to which the coordinates xyz are attached.

Since there is no motion in the roll and pitch directions, the angular velocity and angular acceleration may be expressed as:

$$\vec{\omega} = r\vec{k} \tag{3.1}$$

$$\dot{\vec{\omega}} = \dot{r}\vec{k} \tag{3.2}$$

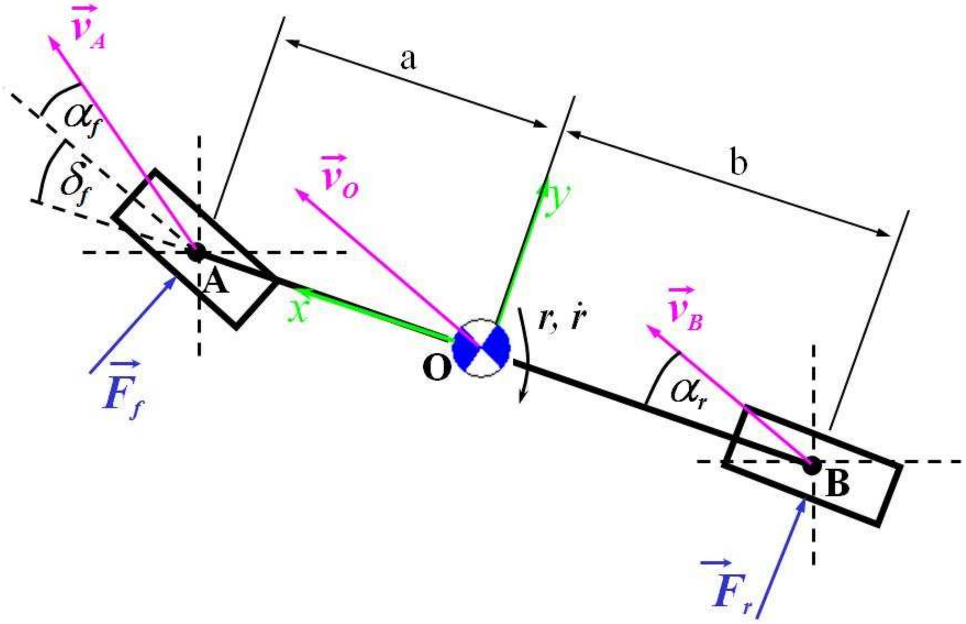

Figure 3.1: Free-body diagram of bicycle model derived in body-fixed coordinates.

The linear velocity of the vehicle measured at the center of gravity is:

$$\vec{v}_O = U\vec{i} + V\vec{j} \tag{3.3}$$

The linear acceleration, which is the derivative of the above equation, is derived by:

$$\vec{a}_O = \dot{U}\vec{i} + U\dot{\vec{i}} + \dot{V}\vec{j} + V\dot{\vec{j}} = -Vr\vec{i} + (\dot{V} + Ur)\vec{j} \tag{3.4}$$

where $\dot{U} = 0$, $\dot{\vec{i}} = \vec{\omega} \times \vec{i} = r\vec{j}$, and $\dot{\vec{j}} = \vec{\omega} \times \vec{j} = -r\vec{i}$. From basic kinematic relations, the velocities at the centers of the front and rear wheels (point A and point B in Figure 3.1) are:

$$\vec{v}_A = \vec{v}_O + \vec{\omega} \times \vec{r}_{OA} = U\vec{i} + (V + ar)\vec{j} \tag{3.5}$$

$$\vec{v}_B = \vec{v}_O + \vec{\omega} \times \vec{r}_{OB} = U\vec{i} + (V - br)\vec{j} \tag{3.6}$$

The geometry in Figure 3.1 allows the front and rear slip angles to be described in terms of the front steering angle δ_f and velocities at points A and B.

$$\alpha_f = \tan^{-1}\left(\frac{v_{A_y}}{v_{A_x}}\right) - \delta_f \approx \left(\frac{v_{A_y}}{v_{A_x}}\right) - \delta_f = \frac{V + ar}{U} - \delta_f \tag{3.7}$$

$$\alpha_r = \tan^{-1}\left(\frac{v_{B_y}}{v_{B_x}}\right) \approx \left(\frac{v_{B_y}}{v_{B_x}}\right) = \frac{V - br}{U} \tag{3.8}$$

After all necessary kinematic relations are considered, the equations of motion can now be derived by using Newtonian-Eulerian mechanics. The summation of forces in the y-direction gives:

$$\sum F_y = F_f + F_r = ma_y \tag{3.9}$$

where $F_f = C_{\alpha f}\alpha_f$, $F_r = C_{\alpha r}\alpha_r$, and $a_y = \dot{V} + Ur$. After substituting the tire forces, lateral acceleration, and slip angles into Eq. 3.9 and rearranging the equation, the equation of motion is found to be:

$$\dot{V} = \left(\frac{C_{\alpha f} + C_{\alpha r}}{mU}\right)V + \left(\frac{aC_{\alpha f} - bC_{\alpha r}}{mU} - U\right)r - \frac{C_{\alpha f}}{m}\delta_f \tag{3.10}$$

Next, considering the yaw dynamics by taking moments about the z-axis, we obtain:

$$\sum M_z = aF_f - bF_r = aC_{\alpha f}\alpha_f - bC_{\alpha r}\alpha_r = I_{zz}\dot{\omega}_z = I_{zz}\dot{r} \tag{3.11}$$

Substitution of the slip angles (Eqs. 4.4 and 4.5) into the above equation and rearrangement of the equation leads to:

$$\dot{r} = \left(\frac{aC_{\alpha f} - bC_{\alpha r}}{I_{zz}U}\right)V + \left(\frac{a^2C_{\alpha f} + b^2C_{\alpha r}}{I_{zz}U}\right)r - \frac{aC_{\alpha f}}{I_{zz}}\delta_f \tag{3.12}$$

To write the equations of motion, Eq. 3.10 and Eq. 3.12, in a state-space representation, the states are defined as follows:

$$\mathbf{x} = \begin{bmatrix} V & r \end{bmatrix}^T \tag{3.13}$$

The state-space vehicle dynamic model is:

$$\begin{bmatrix} \dot{V} \\ \dot{r} \end{bmatrix} = \begin{bmatrix} \dfrac{C_{\alpha f} + C_{\alpha r}}{mU} & \dfrac{aC_{\alpha f} - bC_{\alpha r}}{mU} - U \\ \dfrac{aC_{\alpha f} - bC_{\alpha r}}{I_{zz}U} & \dfrac{a^2C_{\alpha f} + b^2C_{\alpha r}}{I_{zz}U} \end{bmatrix} \begin{bmatrix} V \\ r \end{bmatrix} + \begin{bmatrix} \dfrac{-C_{\alpha f}}{m} \\ \dfrac{-aC_{\alpha f}}{I_{zz}} \end{bmatrix} \delta_f$$

$$\mathbf{y} = \begin{bmatrix} 1 & 0 \\ 0 & 1 \end{bmatrix} \begin{bmatrix} V \\ r \end{bmatrix} + \begin{bmatrix} 0 \\ 0 \end{bmatrix} \delta_f \tag{3.14}$$

3.2 Out-Of-Plane Vehicle Dynamic Model: the Roll Dynamic Model

An out-of-plane vehicle dynamic model is derived in this section. The vehicle model discussed here is expanded from the previous section by including roll dynamics. This addition will enhance the accuracy of the vehicle dynamic model in predicting roll characteristics of the vehicle and in understanding the effects of the vehicle's suspension. The nomenclature used in the development process is listed in Figures 3.2, 3.3, and Table 3.2. Further, the following assumptions are made to simplify the complexity of a vehicle system and the associated mathematics in the derivation process.

- All parts including wheels are rigid bodies.
- A left-right or xz-plane symmetry is assumed so that a four-wheeled vehicle can be approximated as a bicycle-like vehicle (eg $I_{xy} = 0$).
- The vehicle is a front-wheel steering vehicle.
- The vehicle's body has no motion in pitch direction.
- The linear tire model is applied.
- The torsional spring and torsional damper behave linearly.
- The front slip angle α_f, rear slip angle α_r, yaw angle ψ, roll angle ϕ, and

Table 3.2: Nomenclature used in derivation of roll dynamic model.

Symbol	**Definition**
m	total vehicle mass
m_s	sprung mass
m_u	unsprung mass
I_{xx_s}	x-axis mass moment of inertia about CG of sprung mass
I_{zz}	z-axis mass moment of inertia about CG of total vehicle
I_{xz_s}	mass product of inertia about CG of sprung mass
a_s	distance from CG of sprung mass to front axle along the x-axis
b_s	distance from CG of sprung mass to rear axle along the x-axis
a_u	distance from CG of unsprung mass to front axle along the x-axis
b_u	distance from CG of unsprung mass to rear axle along the x-axis
l_{su}	distance from CG of sprung mass to CG of unsprung mass
h_s	height from CG of sprung mass from ground
h_r	height from roll center from ground
U	longitudinal velocity at CG of sprung mass in sprung mass's coordinates
V	lateral velocity at CG of sprung mass in sprung mass's coordinates
ϕ	roll angle of sprung mass
p_s	roll rate of sprung mass
r	yaw rate
$\vec{F}_f$	front tire force
$\vec{F}_r$	rear tire force
$C_{\alpha f}$	front cornering stiffness
$C_{\alpha r}$	rear cornering stiffness
α_f	front slip angle
α_r	rear slip angle
δ_f	front steering angle
K_ϕ	roll stiffness
D_ϕ	roll damping coefficient
g	gravitational acceleration

front wheel steering angle δ_f are small so that the cosines and sines of those angles are approximately one and angles themselves, respectively.

- The vehicle moves with constant velocity along the x-axis.

- The roll center is fixed with respect to the vehicle's body.
- The unsprung mass rotates only in yaw direction.

Based in the above assumptions, the out-of-plane vehicle dynamic model, hereafter called the roll dynamic model, is considered as an inverted pendulum connected to a moving cart consistent with the work of others [59, 11, 60, 61]. Illustrated in Figure 3.2, the model consists of two parts: a sprung mass G_s and an unsprung mass G_u. The sprung mass is a mass that sits on a vehicle's suspension, and the remainder of the vehicle mass is the unsprung mass. Both the sprung and unsprung masses are linked together at a point called the roll center (point R). The roll center is a revolute joint that allows rotation only in the roll direction. The roll center is a virtual point whose location depends upon the type and configuration of the suspension. The masses are supported by a torsional spring K_ϕ and a torsional damper D_ϕ. The torsional spring and torsional damper are assumed to simulate the vehicle's suspensions; additionally, this simplifies difficulties pertaining to the suspensions' kinematics and dynamics. The coordinates xyz are fixed to the center of gravity of the sprung mass (point $\mathrm{G_S}$).

In order to write the equations of motion of the vehicle, the linear accelerations of the sprung and unsprung masses must be determined first. Because it is assumed that there is no motion occurring in the pitch direction, the angular velocity and angular acceleration of the sprung mass may be expressed in vector form by the

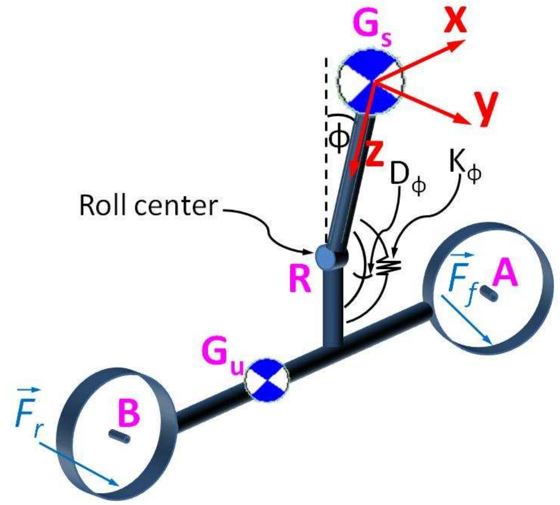

Figure 3.2: Free-body diagram of roll dynamic model derived in body-fixed coordinates.

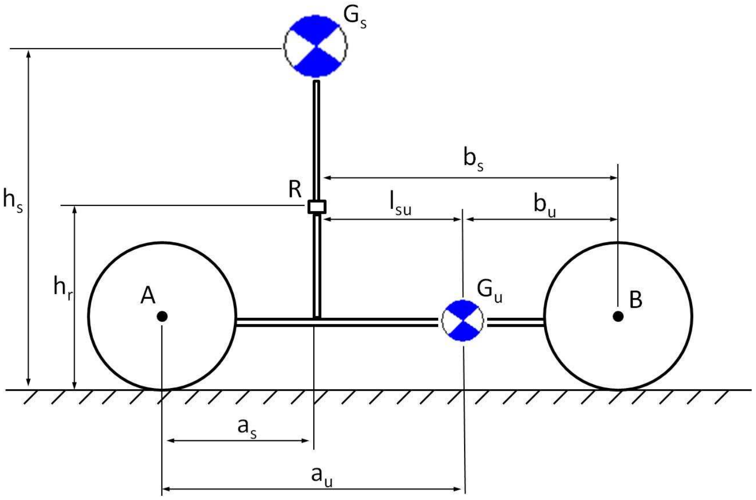

Figure 3.3: Parameters associated with roll dynamic model.

following equations:

$$\vec{\omega}_s = p_s\vec{i} + r\vec{k} \tag{3.15}$$

$$\dot{\vec{\omega}}_s = \dot{p}_s\vec{i} + \dot{r}\vec{k} \tag{3.16}$$

Since planar motion is assumed for the unsprung mass, and the roll center only allows both masses to rotate in the pitch direction, the angular velocity and angular acceleration of the unsprung mass can be written as follows:

$$\vec{\omega}_u = r\vec{k} \tag{3.17}$$

$$\dot{\vec{\omega}}_u = \dot{r}\vec{k} \tag{3.18}$$

The linear velocity at the center of gravity of the sprung mass is:

$$\vec{v}_s = U\vec{i} + V\vec{j} \tag{3.19}$$

where the velocity component in the x-direction, U, is constant. Differentiation of Eq. 3.19 yields the linear acceleration of the sprung mass as:

$$\vec{a}_s = \dot{U}\vec{i} + U\dot{\vec{i}} + \dot{V}\vec{j} + V\dot{\vec{j}} = -Vr\vec{i} + (\dot{V} + Ur)\vec{j} + Vp_s\vec{k} \tag{3.20}$$

where $\dot{U} = 0$, $\dot{\vec{i}} = \vec{\omega}_s \times \vec{i} = r\vec{j}$, and $\dot{\vec{j}} = \vec{\omega}_s \times \vec{j} = -r\vec{i} + p_s\vec{k}$. Using the relative-velocity equation of a rigid body, the linear velocity of the unsprung mass can be written in terms of the linear velocity of the sprung mass, the angular velocities of the sprung and unsprung masses, and the physical dimensions of the vehicle as follows:

$$\vec{v}_u = U\vec{i} + (V - h_{sr}p_s - l_{su}r)\vec{j} \tag{3.21}$$

where $h_{sr} = h_s - h_r$. By differentiating the above equation, the linear acceleration of the unsprung mass may be expressed as:

$$\begin{aligned} \vec{a}_u &= (-Vr + h_{sr}p_s r + l_{su}r^2)\vec{i} + (\dot{V} - h_{sr}\dot{p}_s - l_{su}\dot{r} + Ur)\vec{j} \\ &\quad +(Vp_s - h_{sr}p_s^2 - l_{su}p_s r)\vec{k} \end{aligned} \tag{3.22}$$

With the help of kinematic relations, the velocities at the centers of the front and rear wheels (point A and point B) respectively are:

$$\vec{v}_A = U\vec{i} + (V - h_{sr}p_s + a_s r)\vec{j} \tag{3.23}$$

$$\vec{v}_B = U\vec{i} + (V - h_{sr}p_s - b_s r)\vec{j} \tag{3.24}$$

Thus, the front and rear slip angles can be written as:

$$\alpha_f = \frac{V - h_{sr}p_s + a_s r}{U} - \delta_f \tag{3.25}$$

$$\alpha_r = \frac{V - h_{sr}p_s - b_s r}{U} \tag{3.26}$$

Examining the free-body diagrams of both the unsprung and sprung masses in Figure 3.2 and summing the forces in the y-directions yields:

$$\sum F_y = F_f + F_r = m_s a_{s_y} + m_u a_{u_y} \tag{3.27}$$

where $F_f = C_{\alpha f}\alpha_f$, $F_r = C_{\alpha r}\alpha_r$, $a_{s_y} = \dot{V} + Ur$, and $a_{u_y} = \dot{V} - h_{sr}\dot{p}_s - l_{su}\dot{r} + Ur$. By substituting the front and rear tire forces, lateral accelerations of sprung and unsprung masses, and front and rear slip angles (Eqs. 3.25 and 3.26) into the above equation and rearranging, Eq. 3.27 becomes:

$$\begin{aligned} m\dot{V} - m_u h_{sr}\dot{p}_s - m_u l_{su}\dot{r} &= \left(\frac{C_{\alpha f} + C_{\alpha r}}{U}\right) V - h_{sr}\left(\frac{C_{\alpha f} + C_{\alpha r}}{U}\right) p_s \\ &\quad + \left(\frac{a_s C_{\alpha f} - b_s C_{\alpha r}}{U} - mU\right) r - C_{\alpha f}\delta_f \end{aligned} \tag{3.28}$$

After the force equation is determined, the next step is to consider the moment equations about the x- and z-axes. By analyzing the free-body diagram in Figure 3.2 and applying the Newton-Euler dynamics as well as the assumptions made previously, the moment equation about the x-axis of the sprung mass is:

$$\sum M_x = m_s g h_{sr}\phi - M_K - M_D = m_s h_{sr} a_{s_y} + I_{xx_s}\dot{p}_s - I_{xz_s}\dot{r} \tag{3.29}$$

where $M_K = K_\phi \phi$, $D_K = D_\phi p_s$, and $a_{s_y} = \dot{V} + Ur$. Substitution of the torsional moments induced by the torsional spring and torsional damper and rearrangement of the parameters results in the formulation of Eq. 3.29 as the equation of motion in the roll direction:

$$m_s h_{sr}\dot{V} + I_{xx_s}\dot{p}_s - I_{xz_s}\dot{r} = (m_s g h_{sr} - K_\phi)\phi - D_\phi p_s - m_s h_{sr} U r \tag{3.30}$$

The final equation of motion is obtained from the moment equation about the z-axis. Summation of the yaw moments leads to:

$$\sum M_z = a_s F_f - b_s F_r = I_{zz}\dot{r} - I_{xz_s}\dot{p}_s + m_s a_{s_y} h_{sr} + m_u a_{u_y} l_{su} \tag{3.31}$$

Substituting the tire forces gives:

$$\begin{aligned}(m_u l_{su} + m_s h_{sr})\dot{V} - (I_{xz_s} + m_u l_{su} h_{sr})\dot{p}_s + (I_{zz} - m_u l_{su}^2)\dot{r} = \\ \left(\frac{a_s C_{\alpha f} - b_s C_{\alpha r}}{U}\right) V - h_{sr}\left(\frac{a_s C_{\alpha f} - b_s C_{\alpha r}}{U}\right) p_s \\ + \left[\frac{a_s^2 C_{\alpha f} + b_s^2 C_{\alpha r}}{U} - (m_u l_{su} + m_s h_{sr})U\right] r - a_s C_{\alpha f}\delta_f\end{aligned} \tag{3.32}$$

Thus, all necessary equations of motion (Eqs 3.28, 3.30, and 3.32) have been derived. The equations may be rewritten in a mass-damper-spring form as:

$$\mathbf{M}\dot{\mathbf{x}} + \mathbf{N}\mathbf{x} = \mathbf{F}\delta_f \tag{3.33}$$

where

$$\mathbf{x} = \begin{bmatrix} V & \phi & p_s & r \end{bmatrix}^T \tag{3.34}$$

$$\mathbf{M} = \begin{bmatrix} m & 0 & -m_u h_{sr} & -m_u l_{su} \\ 0 & 1 & 0 & 0 \\ m_s h_{sr} & 0 & I_{xx_s} & -I_{xz_s} \\ (m_u l_{su} + m_s h_{sr}) & 0 & -(I_{xz_s} + m_u l_{su} h_{sr}) & (I_{zz} - m_u l_{su}^2) \end{bmatrix} \tag{3.35}$$

$$\mathbf{N} = -\begin{bmatrix} \left(\frac{C_{\alpha f} + C_{\alpha r}}{U}\right) & 0 & -h_{sr}\left(\frac{C_{\alpha f} + C_{\alpha r}}{U}\right) & \left(\frac{a_s C_{\alpha f} - b_s C_{\alpha r}}{U} - mU\right) \\ 0 & 0 & 1 & 0 \\ 0 & (m_s g h_{sr} - K_\phi) & -D_\phi & -m_s h_{sr} U \\ \left(\frac{a_s C_{\alpha f} - b_s C_{\alpha r}}{U}\right) & 0 & -h_{sr}\left(\frac{a_s C_{\alpha f} - b_s C_{\alpha r}}{U}\right) & N_{44} \end{bmatrix} \tag{3.36}$$

$$N_{44} = \left[\frac{a_s^2 C_{\alpha f} + b_s^2 C_{\alpha r}}{U} - (m_u l_{su} + m_s h_{sr})U\right] \tag{3.37}$$

and

$$\mathbf{F} = \begin{bmatrix} -C_{\alpha f} & 0 & 0 & -a_s C_{\alpha f} \end{bmatrix}^T \tag{3.38}$$

Further, from the mass-damper-spring form, the equations of motion can be represented in a state-space form. The states are previously defined as in Eq. 3.34. Then, the state-pace roll dynamic model is

$$\begin{aligned} \dot{\mathbf{x}} &= \mathbf{A}\mathbf{x} + \mathbf{B}\mathbf{u} \\ \mathbf{y} &= \mathbf{C}\mathbf{x} + \mathbf{D}\mathbf{u} \end{aligned} \tag{3.39}$$

where $\mathbf{A} = -\mathbf{M}^{-1}\mathbf{N}$, $\mathbf{B} = \mathbf{M}^{-1}\mathbf{F}$, $\mathbf{C} = \mathbf{I}_{4\times4}$, $\mathbf{D} = 0$, $\mathbf{u} = \delta_f$, and $\mathbf{I}_{4\times4}$ is a four-by-four identity matrix.

Chapter 4

Measurement, Estimation, and Validation of Vehicle Parameters

This chapter gives an overview of the test vehicle and discusses the procedures used to estimate its physical parameters. This vehicle was used to perform all the tests reported in this work for validating the idea of using the zero-moment-point method to predict vehicle rollover. Hence, it was essential to estimate the numerical values of the vehicle's parameters. The parameters obtained in this chapter are mostly relevant to the rigid vehicle model and the vehicle roll model that were introduced in Chapter 2. Once all the necessary parameters were obtained, the integrity of their values was validated by experimental methods.

4.1 Overview of Test Vehicle

This section provides a detailed description of the data acquisition and control systems that are instrumented on the test truck. This truck is the primary vehicle used to perform all experiments throughout this work. The test vehicle is a robotically-driven 1989 GMC 2500 pick-up truck shown in Fig. 4.1. In addition to an autonomous driving mode, the truck is capable of remote driving via a radio controller. The truck is instrumented with a Global Positioning System (GPS) and an Inertial Measurement Unit (IMU) to collect vehicle states that are later used to calculate the location of ZMP. Moreover, another IMU shown in Figure 4.2 is attached to the rear axle of the truck to acquire states of the unsprung mass.

Figure 4.1: Test truck: 1989 GMC 2500

To detect wheel liftoff, string potentiometers are installed on the vehicle's suspension to measure wheel travel. Moreover, suspension travel is used to calculate

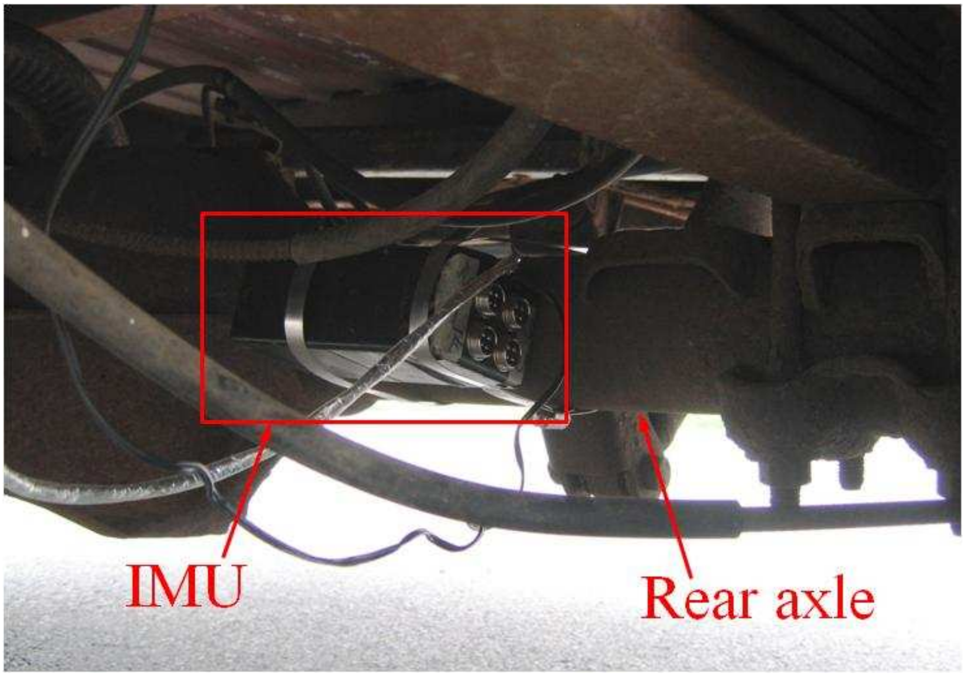

Figure 4.2: IMU on truck's rear axle

the roll angle of the unsprung mass. Figure 4.3 shows the installation of the string potentiometers on the vehicle's suspensions. Another string potentiometer is also

(a) Front suspension.

(b) Rear suspension.

Figure 4.3: Installation of string potentiometers on suspensions.

attached to the steering rack to obtain a front wheel steering angle. The string potentiometers are paired with microcontrollers (Arduino) to convert output signals from analog to digital. All sensors on the truck communicate with a host computer through a TCP/IP network. The computer runs QuaRC, which is a real-time data-acquisition/control software that seamlessly integrates with MATLAB/Simulink, to collect data streaming from the sensors. To make the truck more rollover-prone, approximately 850 kilograms of extra weight is added to the truck's bed. The extra weight is an array of water containers completely filled with water to avoid slosh dynamics. Outriggers are bolted to the front and rear bumpers to prevent catastrophic rollover of the truck.

4.2 Measurement and Estimation of Vehicle Parameters

This section describes the procedures and experimental techniques used to estimate the numerical values of parameters of the test vehicle. The test vehicle, which is a 1989 GMC 2500 pick-up truck, is illustrated in Figure 4.1. The majority of the vehicle parameters, which are described in this section, are relevant to the rigid vehicle model or the vehicle roll model which were discussed in Section 2.2. A few extra parameters that will be used in future sections are also discussed here. It is also important to note that the vehicle parameters that are presented are for the case of an unladen truck.

4.2.1 Vehicle Mass, Location of Center of Gravity , and Physical Dimensions

The procedures to acquire the vehicle mass, location of center of gravity, and physical dimensions are simple and straightforward. To measure the vehicle's weight, it was weighed on a set of corner weight scales as shown in Figure 4.4. The load on each tire is tabulated in Table 4.1. The location of the center of gravity in the horizontal plane was determined from the weight distribution indicated in the table [62]. The unsprung mass of the test truck is taken from that of a 1987 Ford E150 van [63]. The reason behind choosing this van is that it has mass properties which are close to that of a truck, and it also has a type of suspension that is common to most trucks.

Figure 4.4: Test truck on corner weight scales.

To estimate the height of the center of gravity, the procedure indicated in ISO

Table 4.1: Vehicle weight distribution.

	Front left	**Front right**	**Rear right**	**Rear right**
Weight (N)	6636	6458	4587	4676

10392 [62] was followed. The truck's axle was lifted in steps and then the axle load on the other axle and the lifting angle corresponding to each position were recorded. Figure 4.5 shows the position of the truck on a lift as this procedure was conducted.

The height of the center of gravity of the unsprung mass is estimated to be the same as that of the differential's center of gravity, since the mass of the differential dominates most of the unsprung mass. Hence, the height of the center of gravity of the unsprung mass is approximately equal to the radius of the tire. After obtaining the height of the centers of gravity corresponding to the whole truck and the unsprung mass, the height of the center of gravity of the sprung mass is back calculated from the definition of the center of gravity [64]. Lastly, the physical dimensions of the truck such as the wheel base, the track width, etc. were simply measured by a tape measure.

4.2.2 Mass Moment of Inertia

Mass moment of inertia is a property of the body that accounts for the radial distribution of mass with respect to a particular axis of rotation which is normal to the plane of motion [30]. In this work, the mass moments of inertia of the sprung


(a) Front axle on lift. (b) Rear axle on lift.

Figure 4.5: Test truck positioned on lift.

mass of the truck are estimated by the empirical formulae provided in [65] and [66]. The formulae are based on a vehicle's total mass. The formulae to estimate the roll, pitch, and yaw mass moments of inertia of the truck's sprung mass are given by Eqs. 4.1, 4.2, and 4.3, respectively.

$$I_{xx_s} = 0.558 m_{slug}^{4/3} \tag{4.1}$$

$$I_{yy_s} = 0.733 m_{slug}^{5/3} \tag{4.2}$$

$$I_{zz_s} = 2.4154 m_{kg} + 1197.8 \tag{4.3}$$

In the above equations, m_{slug} is the total mass of the vehicle in the units of slug or lbf s^2/ft, and m_{kg} is the total mass of the vehicle in the units of kilogram. Fidelity of these formulae is confirmed in the work of Allen *et al.* [66]. For the unsprung mass's mass moments of inertia, the numerical values of a 1987 Ford E150 van [63] were used. The mass moments of inertia of the whole truck are the summations of those of sprung mass and unsprung mass by using the parallel-axis theorem [30]. All other mass products of inertia are assumed to be zero.

4.2.3 Cornering Stiffness

Cornering stiffness is a constant and is defined as the ratio between the lateral tire force and slip angle, once the tire force model is assumed to be linear. From the definition, the cornering stiffness of a tire can be determined from the slope of a tire force curve, which is a plot between the slip angle of a wheel and the corresponding tire force generated from that wheel.

The test procedure began with the truck driven in a donut pattern in both clockwise and counterclockwise directions on the skid pad area at the Thomas D. Larson Pennsylvania Transportation Institute's test track. A picture of this area is shown in Figure 4.6. The speed of the truck was increased in a slow and continuous manner until 15.6 m/s (35 mph) was reached and then the slowdown was performed in the same fashion. To estimate the cornering stiffnesses of the truck's front and rear wheels, a Global Positioning System (GPS) and an Inertia Measure Unit (IMU) were installed on the truck to obtain velocities and lateral acceleration of the truck during cornering. In addition, a string potentiometer was attached to the steering rack to measure the steering angle of the front wheel of the truck. Based on these velocities and the steering angle, the front and rear slip

Figure 4.6: Skid pad area at the Thomas D. Larson Pennsylvania Transportation Institute's test track.

angles can be obtained through the following equations.

$$\alpha_f = \frac{V + ar}{U} - \delta_f \tag{4.4}$$

$$\alpha_r = \frac{V - br}{U} \tag{4.5}$$

where α_f is the front slip angle, α_r is the rear slip angle, U is the longitudinal velocity, V is the lateral velocity, r is the yaw rate, a is the distance from the vehicle's center of gravity to the front axle, b is the distance from the vehicle's center of gravity to the rear axle, and δ_f is the front steering angle. The longitudinal and lateral velocities are measured at the vehicle's center of gravity. The front and rear tire forces are determined from the lateral acceleration by using the following formulae.

$$F_f = \frac{m a_{G_y} b}{L} \tag{4.6}$$

$$F_r = \frac{m a_{G_y} a}{L} \tag{4.7}$$

where F_f and F_r are the front and rear tire forces, respectively. m is the vehicle mass, a_{G_y} is the lateral acceleration at the center of gravity, and L is the wheel base.

The results from the experiments are illustrated in Figures 4.7 and 4.8, which present the tire force curves of the front and rear wheels, respectively. The lines in these figures are the linear fits determined within the linear portions of the data. The slopes of these lines denote the cornering stiffnesses of the tires, which are -75709 N/rad for the front cornering stiffness and -83686 N/rad for the rear

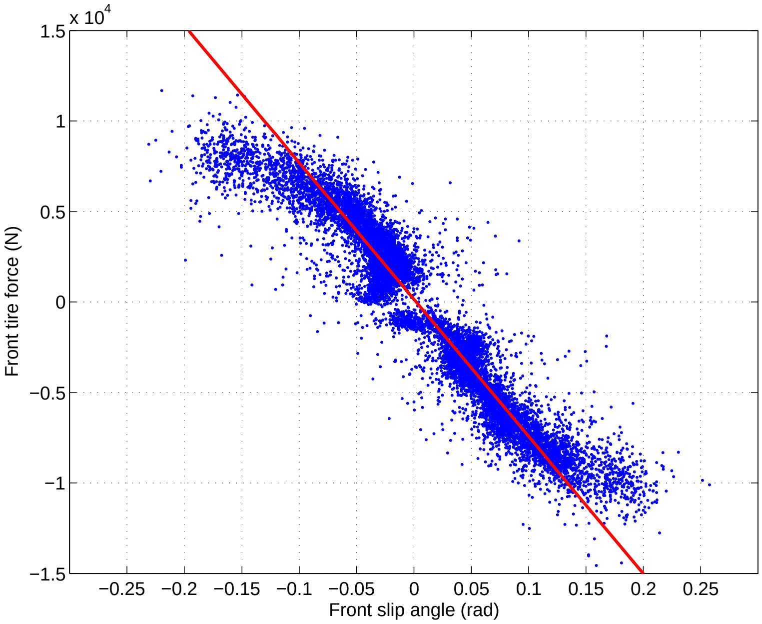

Figure 4.7: Front tire force curve.

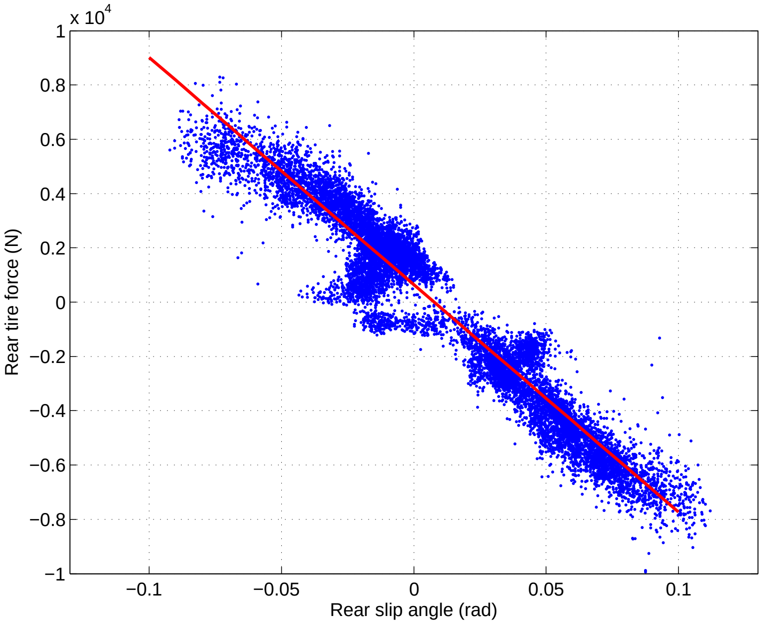

Figure 4.8: Rear tire force curve.

cornering stiffness. Furthermore, the nonlinear characteristics of the tire forces are noticeable in these plots. Also, during the tests at the relatively high speed, the skidding sound of the tires was audible, which is another indication of the nonlinear behaviors of the tires at the high slip angles.

4.2.4 Effective Roll Stiffness

In the roll dynamic model, a vehicle is modeled as an inverted pendulum on a moving cart. The pendulum is supported by a torsional spring and a torsional damper. The spring and damper are assumed to represent the vehicle's suspension system. Thus, it is essential to obtain the effective roll stiffness and effective roll damping coefficient in order to describe the roll characteristics of the vehicle.

The procedure to estimate the roll stiffness is similar to the one used to obtain the values of the cornering stiffnesses in Section 4.2.3. The truck was circled on the skid pad area in both clockwise and counterclockwise directions. In each direction, the speed of the truck was slowly and continuously ramped up until 15.6 m/s (35 mph) and then gradually decreased. The IMU on the truck measured the roll angle and the lateral acceleration of the truck. Given the lateral acceleration, the roll moment may be expressed as:

$$M_\phi = m_s a_{G_y}(h_s - h_r) \tag{4.8}$$

where M_ϕ is the roll moment induced by the lateral acceleration, m_s is the mass of sprung mass, a_{G_y} is the lateral acceleration at the center of gravity, h_s is the height of the center of gravity of sprung mass from ground, and h_r is the height of the roll center from ground.

Figure 4.9 presents the plot between the roll angle and roll moment induced lateral acceleration. The dots in the figure represent the experimental data points, and the line is obtained by performing linear regression over them. The effective roll stiffness is the slope of the linear fit and is computed to be 71177 N-m/rad. Moreover, it is evident from the experimental results that the suspension behavior is relatively linear.

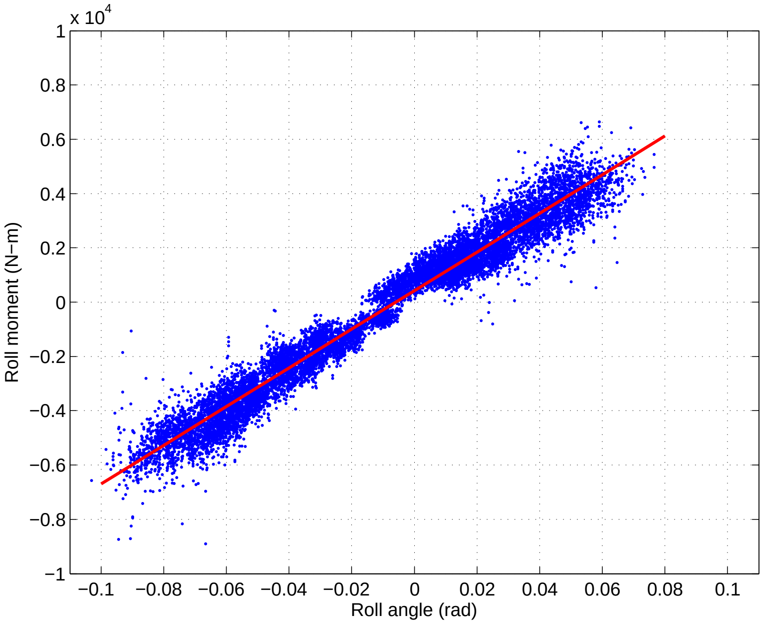

Figure 4.9: Roll stiffness determined from the slope of the plot between roll angle and roll moment.

4.2.5 Calibration of Steering Mechanism

To measure the steering angle of the front wheels of the test truck, a string potentiometer was attached to the steering rack of the truck's steering mechanism. The output signal of the potentiometer was connected to an analog input of a microcontroller (Arduino) that acts as a data-acquisition unit and sends the data to a host computer over a network. The microcontroller also provides a five-volt power source to the potentiometer.

Slip plates were used to create a calibration curve for the steering sensor. The plates were put under the front wheels of the truck to measure the steering angles. The calibration process was simultaneously performed on both the front wheels. The output readings of the controller were recorded at three-degree intervals of the front left wheel and plotted as shown in Figures 4.10 and 4.11. In the figures, the dots represent the experimental data points. Furthermore, it is visually clear from the results that the steering sensor does indeed follow a linear trend. The trend lines corresponding to each wheel are given by the following equations and are represented by solid red lines in both the figures

$$\delta_{fl} = -0.0337R + 83.782 \tag{4.9}$$

$$\delta_{fr} = -0.0334R + 83.925 \tag{4.10}$$

where δ_{fl} and δ_{fr} denote the steering angles of the front left and right wheels, respectively. R is the digital reading of the microcontroller.

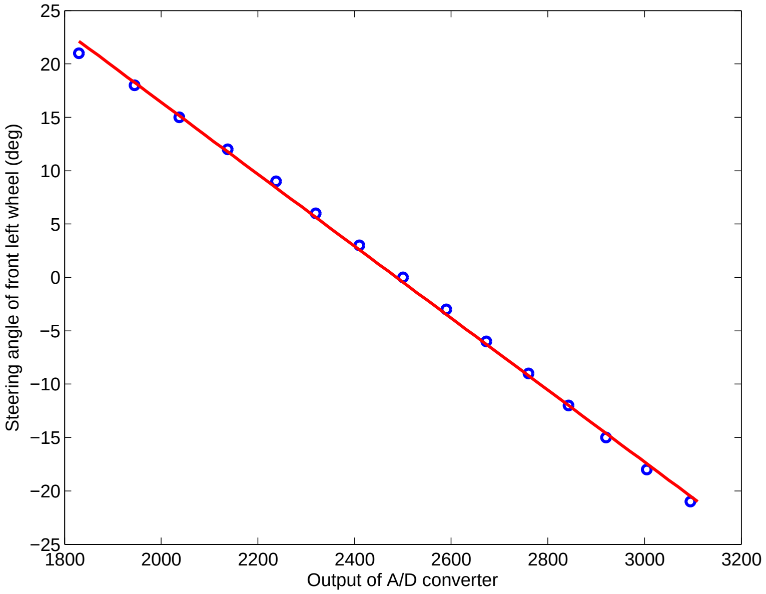

Figure 4.10: Calibration curve of front left wheel

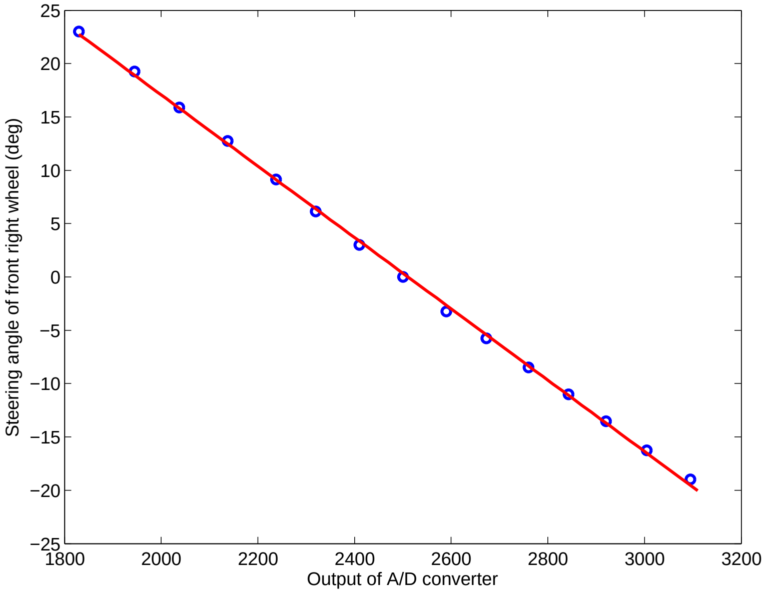

Figure 4.11: Calibration curve of front right wheel

4.2.6 Calibration of String Potentiometers on Suspensions

String potentiometers are installed on the truck's suspensions to measure suspension travel, the information that is later used to detect wheel lift. Furthermore, the suspension travel is used to calculate roll angle of the unsprung mass of the truck. To serve this purpose, these potentiometers need to be calibrated; thus, the relationships between the outputs of analog-to-digital converters and the suspension travel are determined. The truck was lifted up by a hydraulic floor jack. The suspension travel of each wheel was measured by a tape measure. The calibrations were done one axle at a time.

The calibration curves of the front left, front right, rear left, and rear right suspensions respectively are illustrated in Figures 4.12, 4.13, 4.14, and 4.15. In the figures, the dots represent the experimental results, and the lines show the

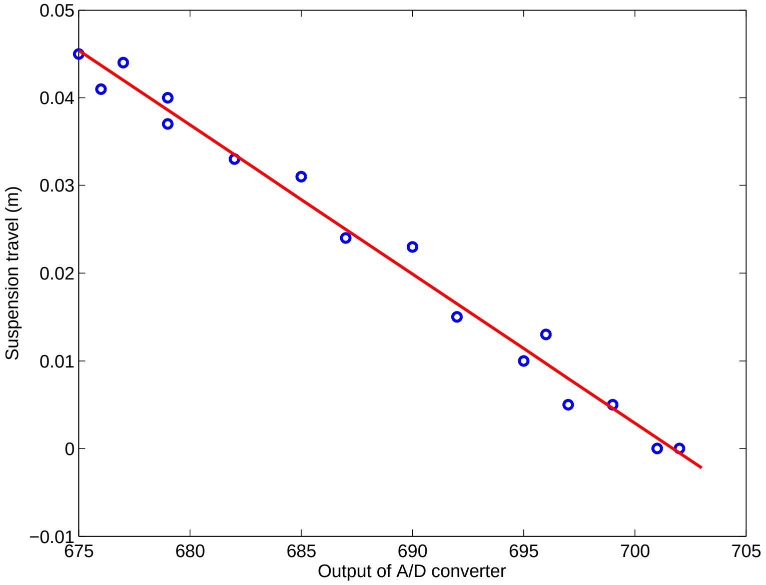

Figure 4.12: Calibration curve of string potentiometer mounted on front left suspension

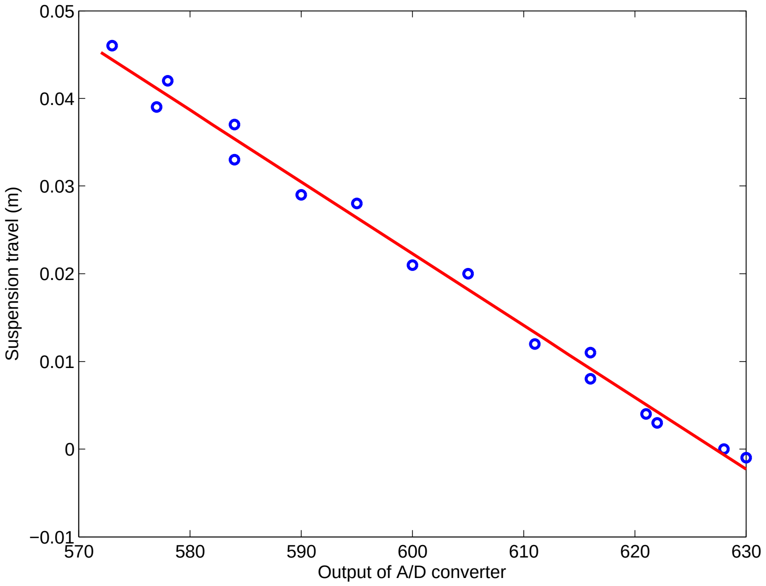

Figure 4.13: Calibration curve of string potentiometer mounted on front right suspension

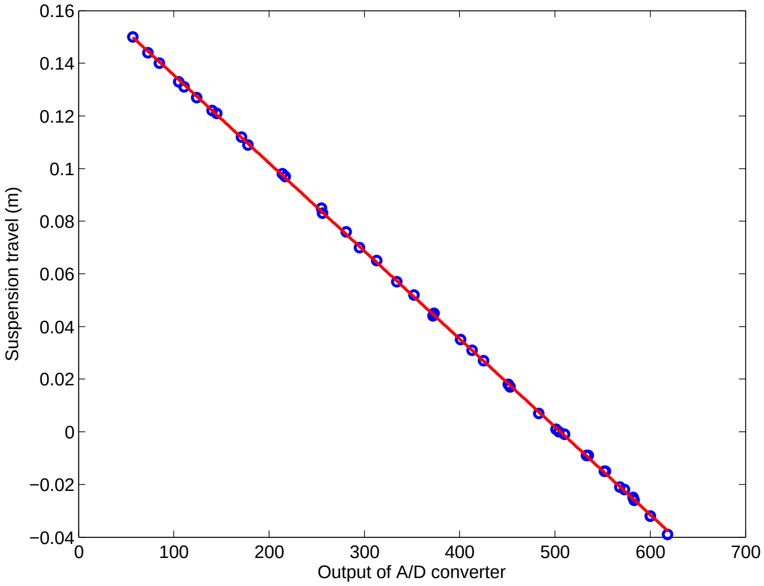

Figure 4.14: Calibration curve of string potentiometer mounted on rear left suspension

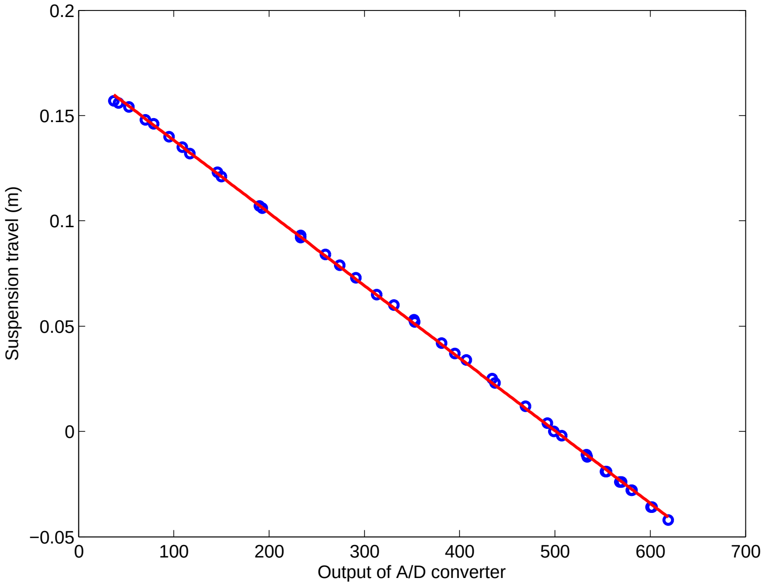

Figure 4.15: Calibration curve of string potentiometer mounted on rear right suspension

linear model fit. The equations to convert from the the analog-to-digital readings to the suspension travel are as follows:

$$ST_{fl} = -0.0017R_{fl} + 1.1933 \tag{4.11}$$

$$ST_{fr} = -0.0008R_{fr} + 0.5138 \tag{4.12}$$

$$ST_{rl} = -0.0003R_{rl} + 0.1689 \tag{4.13}$$

$$ST_{rr} = -0.0003R_{rr} + 0.1726 \tag{4.14}$$

where R is the output reading of the analog-to-digital converter, and ST is the suspension travel. Subscripts fl, fr, rl, and rr denote the locations of the suspensions, standing for front left, front right, rear left, and rear right, respectively.

4.2.7 Summary of Unladen Truck's Parameters

The physical properties of the unladen truck shown in Figure 4.1 are summarized in Table 4.2.

Table 4.2: Vehicle parameters of unladen truck.

Symbol	Value	Unit	Symbol	Value	Unit
m	2279	kg	m_u	299	kg
m_s	1980	kg	a	1.390	m
b	1.964	m	a_u	2.042	m
b_u	1.312	m	a_s	1.358	m
b_s	1.996	m	T	1.615	m
h	0.812	m	h_u	0.352	m
h_s	0.882	m	h_r	0.50	m
I_{xx}	854	kg·m^2	I_{yy}	5450	kg·m^2
I_{zz}	5411	kg·m^2	I_{xz}	0	kg·m^2
I_{yz}	0	kg·m^2	I_{xx_u}	145	kg·m^2
I_{yy_u}	802	kg·m^2	I_{zz_u}	947	kg·m^2
I_{xz_u}	0	kg·m^2	I_{yz_u}	0	kg·m^2
I_{xx_s}	636	kg·m^2	I_{yy_s}	4501	kg·m^2
I_{zz_s}	4317	kg·m^2	I_{xz_s}	0	kg·m^2
I_{yz_s}	0	kg·m^2	$C_{\alpha f}$	-75709	N/rad
$C_{\alpha r}$	-83686	N/rad	K_ϕ	71177	N-m/rad
D_ϕ	2000	N-m-s/rad	-	-	-

4.3 Experimental Validation of Vehicle Parameters

With the help of the vehicle dynamic models derived in the previous chapter, the fidelity of the parameters of the unladen truck estimated in Section 4.2 is checked by using experimental methods in this section. The tests were performed at the Thomas D. Larson Pennsylvania Transportation Institute's test track as before. The truck was equipped with a GPS/IMU system to collect vehicle states during the tests. The main variables of interest during these tests are lateral velocity, yaw rate, roll rate, and front steering angle. More details about the instrumentation on the test truck can be found in Section 4.1.

The truck was driven at the relatively constant longitudinal speed of 11.18 m/s (25 mph) on the straight portion of the test track. The fidelity of the vehicle parameters was evaluated by measuring the frequency response of the vehicle. To obtain the frequency response, the truck was excited by a series of sinusoidal steering inputs. The frequency of the sine-wave inputs ranged from 0.15 Hz to 3.47 Hz, and the response for each individual frequency was recorded. The frequency responses of the experimental data were created by using a technique called correlation frequency response analysis. [67, 68]. Figure 4.16 illustrates the frequency response of the lateral velocity of the truck for different frequencies of the front steering input. Similarly, the frequency responses corresponding to the yaw rate and the roll rate are shown in Figures 4.17 and 4.18, respectively.

In all of these figures, the experimental frequency responses are compared to those determined from the bicycle model and the roll dynamic model, which are respectively denoted by a solid blue line and a dash-dot red line. The top section of the plots is the magnitude plot, and the lower section is the phase plot. One can see that the frequency responses of the vehicle models match with the experimental results really well. From the above results, it can be deduced that the vehicle parameters in Table 4.2 are able to represent the physical properties of the truck.

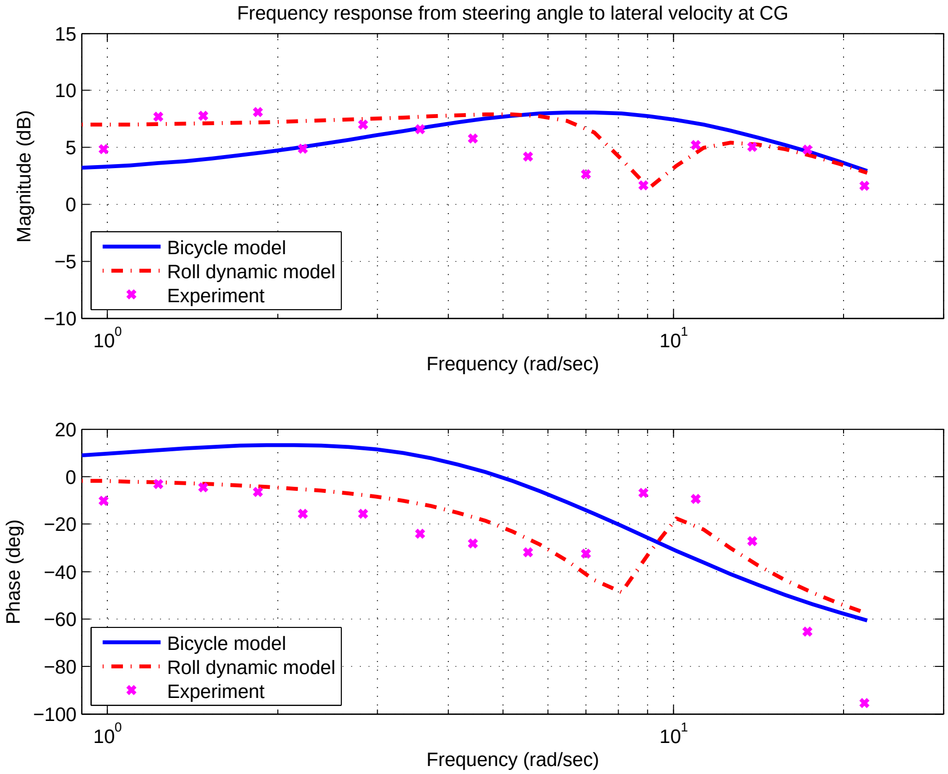

Figure 4.16: Frequency response of the truck compared to the bicycle model and the roll dynamic model from front steering angle to lateral velocity.

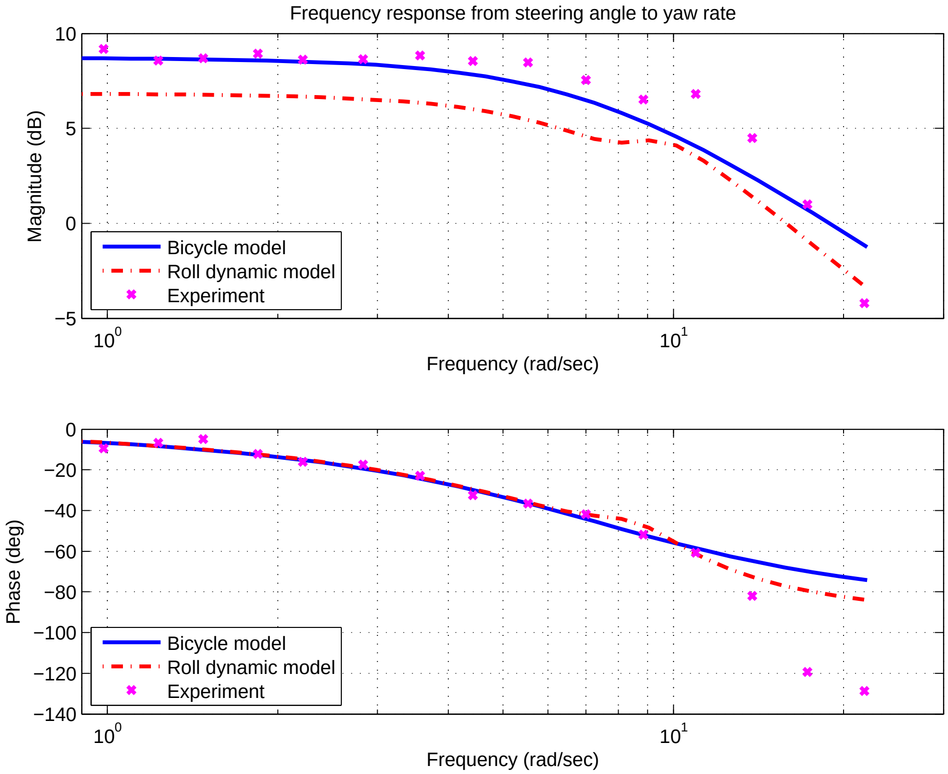

Figure 4.17: Frequency response of the truck compared to the bicycle model and the roll dynamic model from front steering angle to yaw rate.

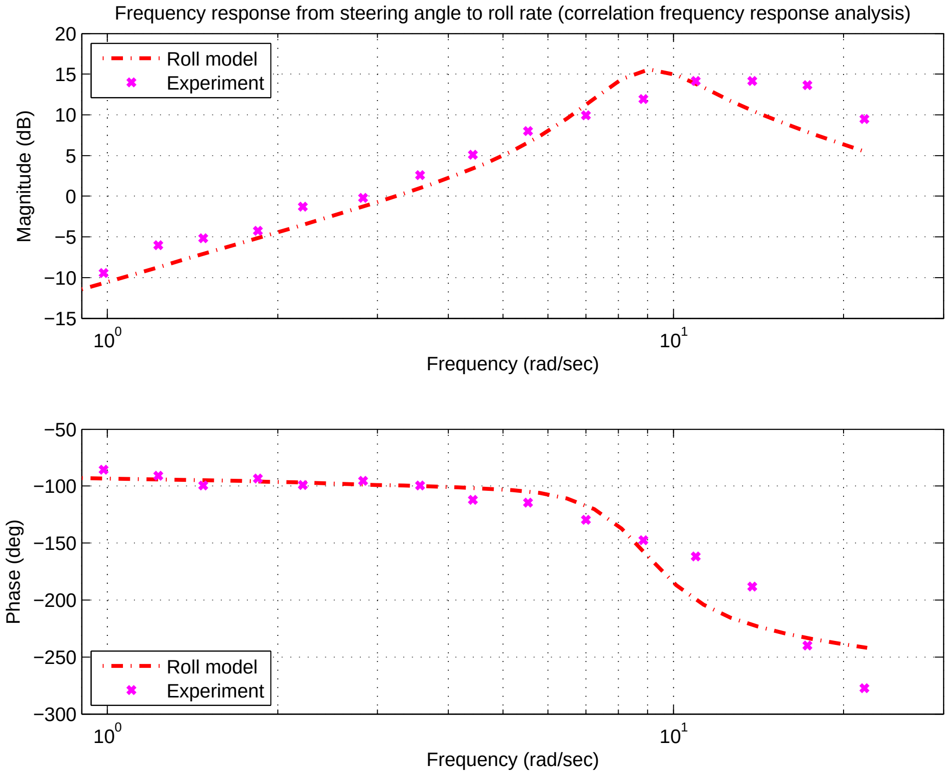

Figure 4.18: Frequency response of the truck compared to the roll dynamic model from front steering angle to roll rate.

Chapter 5

Results

The effectiveness of the zero-moment-point-based rollover threat indices derived in Chapter 2 is analyzed and validated in this chapter, first with simulations and later through field experiments. A vehicle-dynamic software package called CarSim was utilized to simulate vehicle rollover in various circumstances. Once the simulation results confirmed the feasibility of the proposed rollover algorithm, the field experiments were conducted. The experimental results revealed the dynamic behaviors of the ZMP-based rollover metrics in real-life scenarios. Later, extensive analyses of the experimental results were performed to better understand the mechanisms behind vehicle rollover.

Table 5.1: Vehicle parameters used in simulations.

Symbol	**Value**	**Unit**	**Symbol**	**Value**	**Unit**
m	1843	kg	m_u	180	kg
m_s	1663	kg	a	1.175	m
b	1.403	m	c	0.028	m
d	0.257	m	T	1.565	m
h	0.847	m	h_u	0.36	m
h_s	0.9	m	h_r	0.494	m
I_{xx}	762.09	kg·m^2	I_{yy}	2857.56	kg·m^2
I_{zz}	3074.32	kg·m^2	I_{xz}	59.98	kg·m^2
I_{yz}	0	kg·m^2	I_{xx_u}	61.73	kg·m^2
I_{yy_u}	346.37	kg·m^2	I_{zz_u}	357.13	kg·m^2
I_{xz_u}	0	kg·m^2	I_{yz_u}	0	kg·m^2
I_{xx_s}	653	kg·m^2	I_{yy_s}	2498	kg·m^2
I_{zz_s}	2704	kg·m^2	I_{xz_s}	85	kg·m^2
I_{yz_s}	0	kg·m^2	g	9.81	m/s^2

5.1 Simulation Results

In this section, the proposed rollover prediction algorithms for both the rigid vehicle model (Eqs. 2.17 and 2.18) and vehicle roll model (Eqs. 2.31 and 2.32) are implemented. CarSim, which is a multi-body vehicle simulation software, was used to simulate a Sport Utility Vehicle (SUV). Vehicle parameters used in simulations were primarily taken from [69, 21]. The parameters are summarized in Table 5.1. The definitions of the nomenclature in Table 5.1 are defined in Tables 2.1 and 2.2.

The algorithms were tested in two different scenarios: on a flat road and on a banked road. In each scenario, the vehicle was excited in a way such that wheel liftoff and rollover was induced. The Toyota J-turn and double lane change are two primary maneuvers used throughout the simulations. When simulating the Toyota J-turn maneuver, the vehicle was first steered as quickly as possible 294 degrees of steering wheel angle, and then 588 degrees in the opposite direction as quickly as possible. During this maneuver, the vehicle's path resembles a fishhook shape [70]. To determine when wheel liftoff had occurred, the Load Transfer Ratio (LTR) [23] was used as an indicator. The LTR is defined as:

$$LTR = \frac{F_{z_R} - F_{z_L}}{F_{z_R} + F_{z_L}} \tag{5.1}$$

where F_{z_L} and F_{z_R} are normal forces acting on tires on left and right sides of the vehicle, respectively. The LTR ranges from -1 to 1, and once wheel liftoff occurs, the absolute value of the LTR is equal to one.

5.1.1 Simulation Results on Flat Road

The LTRs and displacements of y_{zmp} calculated from Eqs. 2.18 and 2.32 of the vehicle that was excited by the Toyota J-turn on a flat road, leading to wheel liftoff and rollover, are respectively plotted in Figures 5.1 and 5.2. Figure 5.3 shows the results during the double-lane-change maneuver on the flat road that induced wheel liftoff, and the results of the rollover case are included in Figure 5.4. In the figures, the top part of the plot depicts the load transfer ratio, and the bottom part illustrates the displacement of y_{zmp}. The dash-dotted magenta line is the displacement of y_{zmp} determined from the rigid vehicle model. The displacement of y_{zmp}

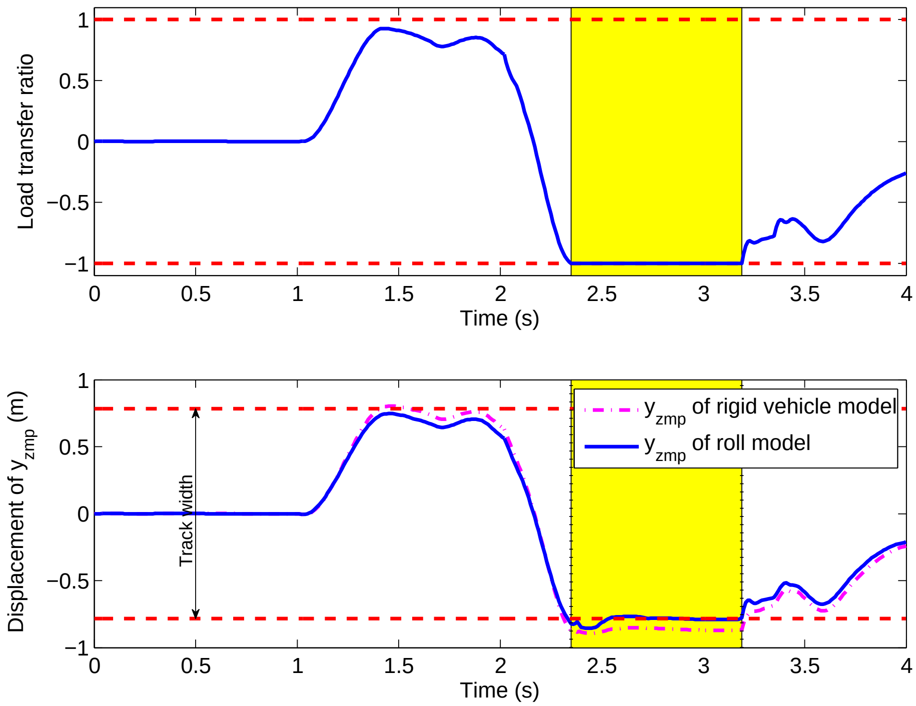

Figure 5.1: LTRs and displacements of y_{zmp} of vehicle during Toyota J-turn on flat road, causing wheel liftoff.

calculated from the vehicle roll model is the solid blue line. The distance between the red dash lines is the track width. The yellow shaded regions in the figures indicate the regions that wheel liftoff has occurred in CarSim. More discussions of the results will be given in Section 5.2.

5.1.2 Simulation Results on Banked Road

For the banked-road simulations, a severely banked road was constructed with a 30%-grade i.e. an inclination angle of 16.70 degrees. Figures 5.5 and 5.6 respectively illustrate the LTRs and displacements of y_{zmp} of the vehicle undergoing

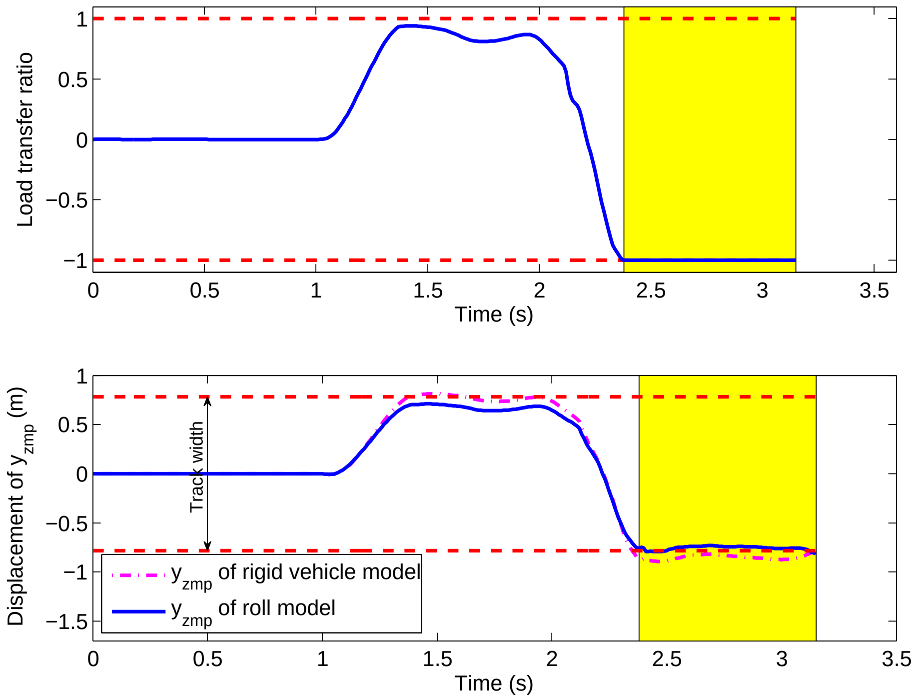

Figure 5.2: LTR and displacements of y_{zmp} of vehicle during Toyota J-turn on flat road, causing rollover.

wheel liftoff and rollover during the Toyota J-turn on the banked road. The results of the vehicle from the double-lane-change maneuver that caused wheel liftoff are shown in Figure 5.7. Figure 5.8 plots the LTR and displacement of y_{zmp} of the vehicle that rolled over during the double-lane-change excitation. The wheel liftoff regions in the figures are shaded.

5.2 Discussion of Simulation Results

A few observations can be made from the simulation results. First, the displacements of y_{zmp} for both the rigid vehicle model and vehicle roll model predict vehicle

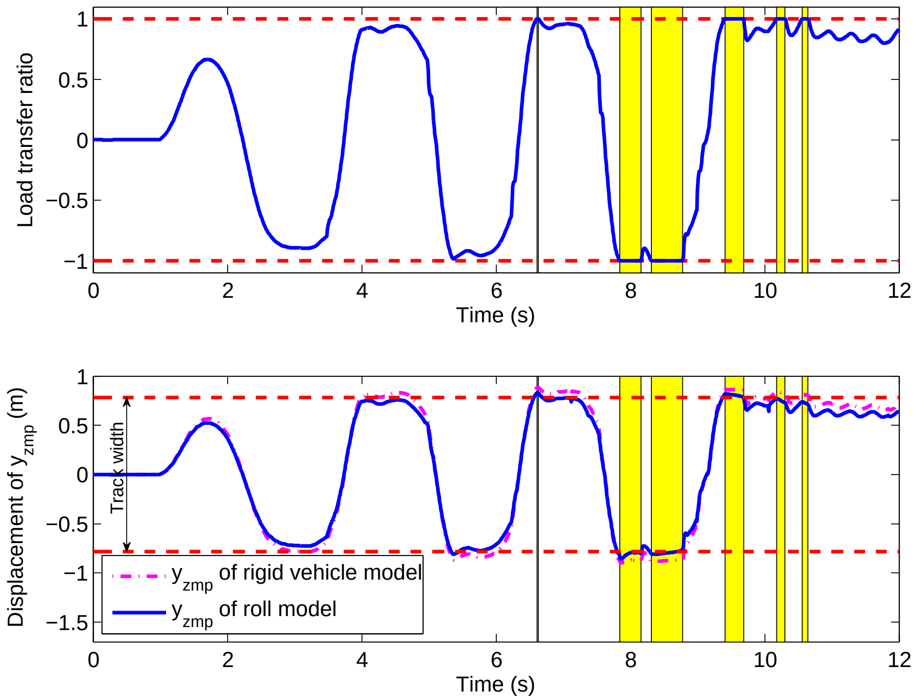

Figure 5.3: LTR and displacements of y_{zmp} of vehicle during double lane change on flat road, causing wheel liftoff.

rollover quite well; however, the displacement of y_{zmp} estimated from the rigid vehicle model (from Eq. 2.18) is more conservative than the one obtained from the roll model (from Eq. 2.32). This may happen since the roll model is more realistic than the rigid vehicle model, causing the behavior of the vehicle roll model to more closely mimic to a real vehicle.

The second observation is that the displacement of y_{zmp} during wheel liftoff is a relatively flat straight line. Since there is no external force applied to the vehicle, the only place that reaction forces can physically act during wheel liftoff is on the edge of the vehicle, allowing the vehicle to rock itself on its wheels due to the

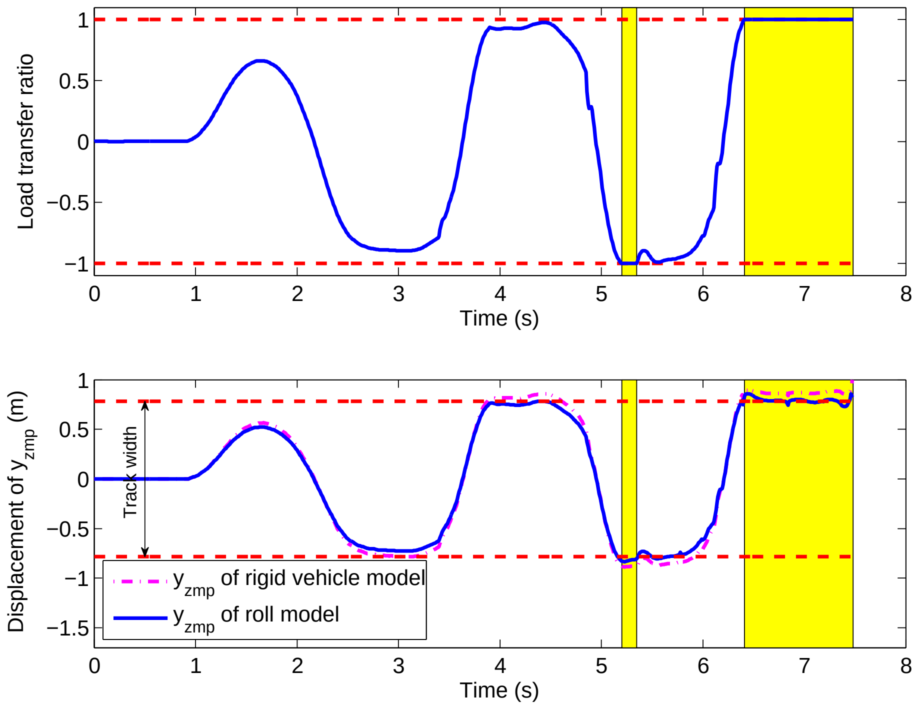

Figure 5.4: LTR and displacements of y_{zmp} of vehicle during double lane change on flat road, causing rollover.

effects of its own momentum. Thus, we see that the ZMP method also saturates as do other metrics, but this saturation is due to physics of the system and not the way that the metric is defined.

The last observation that one can notice is that the shapes of the LTRs and displacements of y_{zmp} are remarkably similar. The shape similarity comes from the fact that the zero-moment-point technique is an alternative way to represent load transfer, yet one that avoids any calculation of wheel normal forces.

Furthermore, Table 5.2 shows the averages of the absolute values of the displacements of y_{zmp} at wheel liftoff and average percent errors of y_{zmp}. The averages

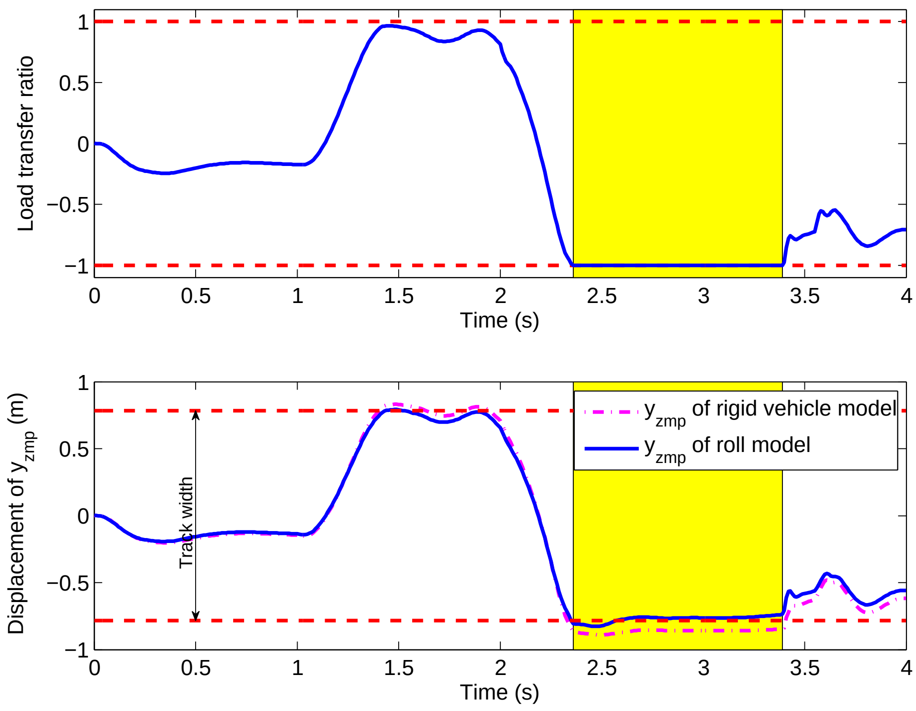

Figure 5.5: LTR and displacements of y_{zmp} of vehicle during Toyota J-turn on banked road, causing wheel liftoff.

and errors were computed from the rigid vehicle model and vehicle roll model. These are compared against the Static Stability Factor (SSF) [4, 5] and Dynamic Stability Index (DSI) [7]. The mathematical representations of the SSF and DSI are respectively in Eqs. 1.2 and 1.10. Furthermore, the average percent errors in Table 5.2 are pictorially presented in Figure 5.9. The reason behind using the average values is that, in certain scenarios, wheel liftoff happens more than once. From Table 5.2 and Figure 5.9, one can see that both SSF and DSI cannot predict wheel liftoff as precisely as the ZMP-based rollover indices proposed in this work, especially when the influence of terrain is present.

Table 5.2: Wheel-lift predictions and percent errors from y_{zmp} derived from rigid vehicle model and vehicle roll model, Static Stability Factor (SSF) and Dynamic Stability Index (DSI).

Condition and Maneuver	Static Stability Factor (SSF) Threshold = 0.924		Dynamic Stability Index (DSI) Threshold = 0.924		y_{zmp} (rigid vehicle model) Threshold = 0.7825		y_{zmp} (vehicle roll model) Threshold = 0.7825	
	Average of absolute value at wheel lift	Average percent error	Average of absolute value at wheel lift	Average percent error	Average of absolute value at wheel lift	Average percent error	Average of absolute value at wheel lift	Average percent error
FR[a], TJ[b], WL[c]	0.757	18.1	0.770	16.7	0.8775	12.1	0.8232	5.2
FR, TJ, RO[d]	0.806	12.8	0.843	8.8	0.8682	11.0	0.7560	3.4
FR, DLC[e], WL	0.759	17.9	0.752	18.6	0.8607	10.0	0.8006	4.6
FR, DLC, RO	0.808	12.6	0.795	14.0	0.8778	12.2	0.8293	6.0
BR[f], TJ, WL	0.473	48.8	0.473	48.8	0.8618	10.1	0.8049	2.9
BR, TJ, RO	0.473	48.8	0.473	48.8	0.8599	9.9	0.8034	2.7
BR, DLC, WL	0.967	9.6	0.967	9.6	0.8777	12.2	0.8350	6.7
BR, DLC, RO	0.784	27.6	0.785	27.5	0.8518	8.9	0.8120	3.8

[a] FR = flat road, [b] TJ = Toyota J-turn, [c] WL = wheel liftoff, [d] RO = rollover, [e] DLC = double lane change, [f] BR = banked road

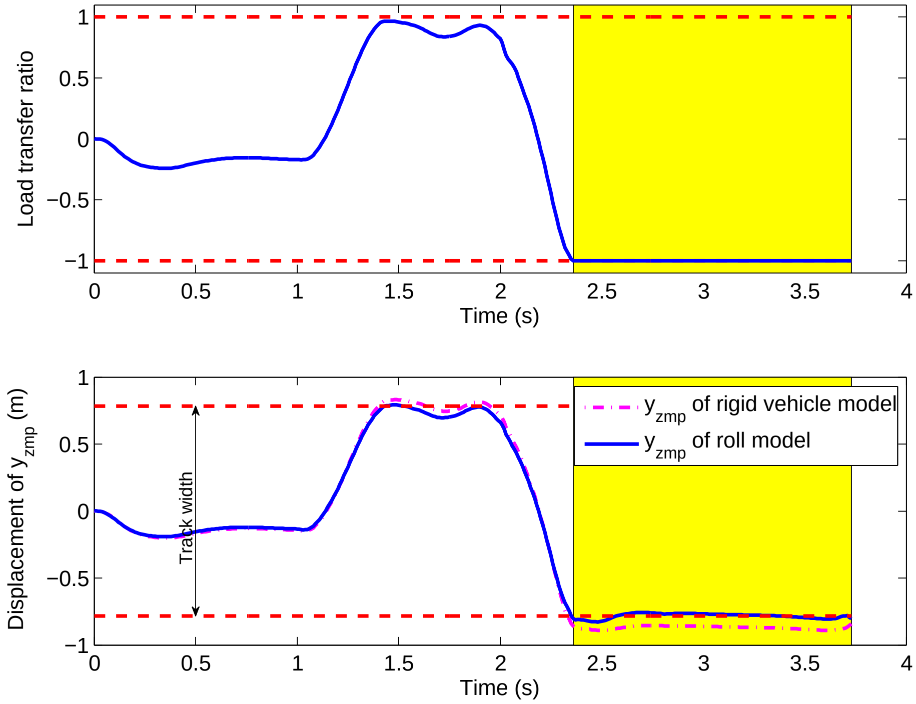

Figure 5.6: LTR and displacements of y_{zmp} of vehicle during Toyota J-turn on banked road, causing rollover.

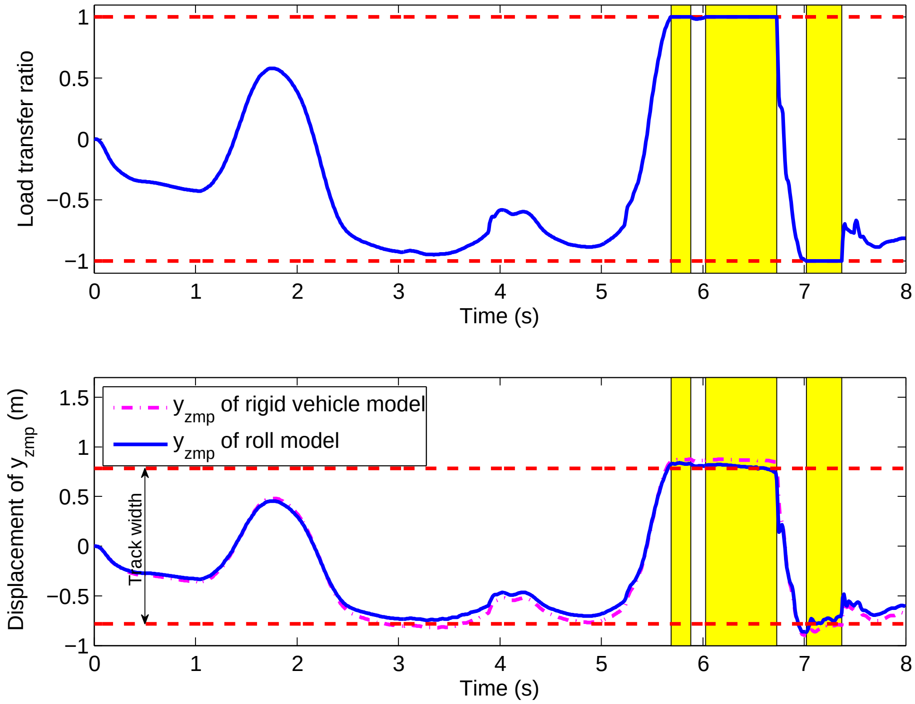

Figure 5.7: LTR and displacements of y_{zmp} of vehicle during double lane change on banked road, causing wheel liftoff.

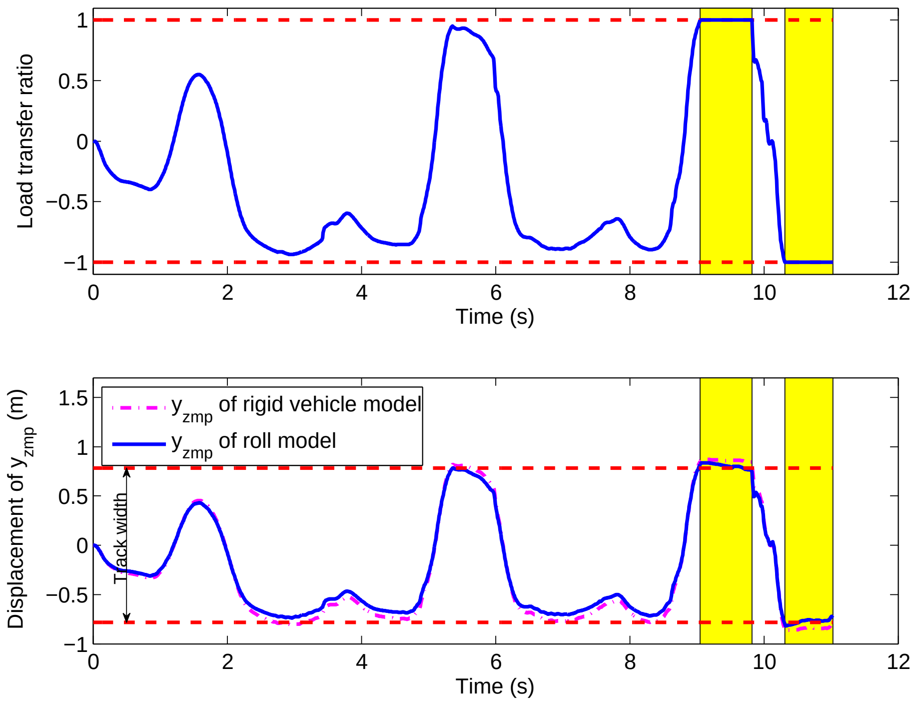

Figure 5.8: LTR and displacements of y_{zmp} of vehicle during double lane change on banked road, causing rollover.

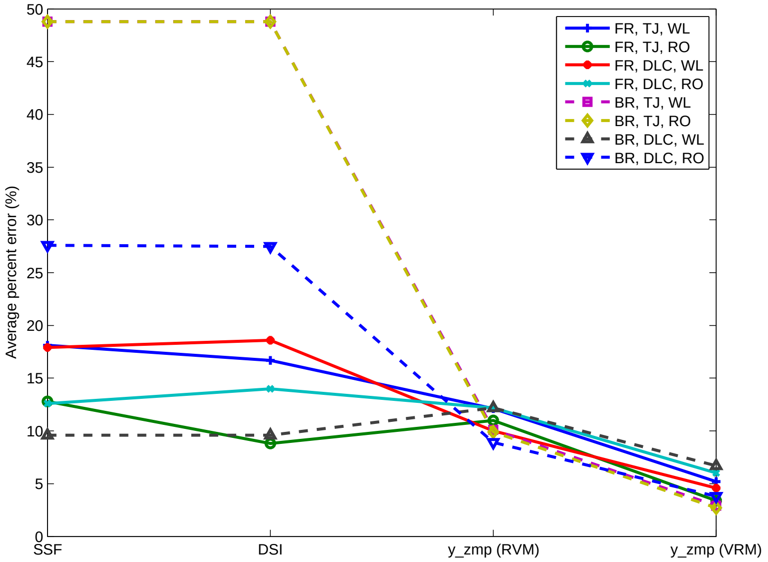

Figure 5.9: Average percent errors of Static Stability Factor (SSF), Dynamic Stability Index (DSI), y_{zmp} (rigid vehicle model), and y_{zmp} (vehicle roll model).

5.3 Experimental Results

This section shows the effectiveness of the proposed rollover prediction algorithms from both the rigid vehicle model (Eq. 2.18) and the vehicle roll model (Eq. 2.32). The algorithms were implemented with the test truck described in Section 4.1. All tests were conducted at the Thomas D. Larson Pennsylvania Transportation Institute's test track. In the experiments, the height of the truck's center of gravity was varied by different loading conditions, so that wheel liftoff could happen at various speeds. The truck was excited under two maneuvers, the Toyota J-turn and a double-lane change, on two road profiles. Pictures of the road sections on which the experiments were performed are shown in Figures 5.10 and 5.11. Figure 5.10 illustrates the flat-road section, and Figure 5.11 presents the banked-road section. The banked-road section has an inclination of seven degrees.

To determine when wheel liftoff had occurred, string potentiometers were mounted on the truck's suspensions. More details about the truck are given in Section 4.1. The truck's properties (e.g. mass, mass moments of inertia, etc.) used to calculate the locations of y_{zmp} of the rigid vehicle model and the vehicle roll model are listed in Appendix A. The procedures and techniques used to obtain the truck's parameters are described in Section 4.2.

Figure 5.10: Flat-road section at the Thomas D. Larson Pennsylvania Transportation Institute's test track.

5.3.1 Experimental Results on Flat Road

This section presents the experimental validation results obtained from the tests in which the truck was driven on the flat road. The flat-road section used in the tests is illustrated in Figure 5.10. The truck underwent various testing conditions to confirm the fidelity of the ZMP-based rollover threat indices. However, all of the results are not given in this section. Additional experimental results can be found in Appendix B.

The results shown in this section were taken from the following scenarios: (1) the test in which no wheel liftoff occurred, (2) the test in which wheel liftoff occurred, and (3) the test in which no wheel liftoff occurred, but the truck skidded.

Figure 5.11: Banked-road section at the Thomas D. Larson Pennsylvania Transportation Institute's test track.

Under these scenarios, one can see how effectively the ZMP-based rollover metric behaves and predicts wheel lift. The testing conditions, the brief descriptions, and the results of the select experiments are summarized in Table 5.3. The testing conditions include: (1) the maneuver used to excite the truck, (2) the speed of the truck in that particular test, and (3) the loading condition on the truck. The vehicle parameters used to calculate the displacement of y_{zmp} in the corresponding tests are also given in Table 5.3. It is also important to note that, in the case of Figure 5.14, the wheel liftoff induced a very large roll angle, which caused the outriggers to touch the ground. However, as described previously, the fact that the outriggers hit the ground does not have any dynamic effects in calculating the y_{zmp}, since the moments generated by the forces that are tangential to the supporting surface are not components of the tipping moments. At this point, it may be noted that adding more contact points changes the shape of the support polygon but not the position of the ZMP. Additionally, a series of snapshots captured from one of the tests in which wheel lift happened is shown in Figure 5.12.

Figure 5.12: Snapshots of the truck during wheel liftoff.

In the plots of the results (Figures 5.13, 5.14, 5.15, 5.16, and 5.17), the top section of the plots shows the percentage of suspension travel. 100 percent of suspension travel means that the truck's suspension is fully extended, or, in other words, that wheel liftoff is happening. Each line in the plots represents suspension travel on each side of the truck. The displacements of y_{zmp} are illustrated in the bottom section of the plots. In the plots of the displacements of y_{zmp}, the solid magenta line represents the displacement of y_{zmp} estimated from the rigid vehicle model. The dash blue line denotes the displacement of y_{zmp} of the vehicle roll model. The distance between the dotted red lines signifies the track width of the test truck. The shaded regions in the figures indicate the regions where wheel liftoff has occurred. The cyan areas mark the regions in which only one wheel is

Table 5.3: Testing conditions, brief descriptions, and results of wheel-lift experiments on flat road.

Maneuver	**Speed** (m/s)	**Loading condition** (kg)	**Parameter**	**Description**	**Results**
Toyota J	10	448	Table A.2	No wheel lift.	Figure 5.13
Toyota J	17	448	Table A.2	Both of the right wheels lifted off.	Figure 5.14
Toyota J	20	0	Table A.1	No wheel lift, but the truck skidded.	Figure 5.15
Double-lane change	15.5	448	Table A.2	Both of the right wheels lifted off on the first turn, and only the rear left wheel lifted on the second turn.	Figure 5.16
Double-lane change	20	0	Table A.1	No wheel lift, but the truck skidded.	Figure 5.17

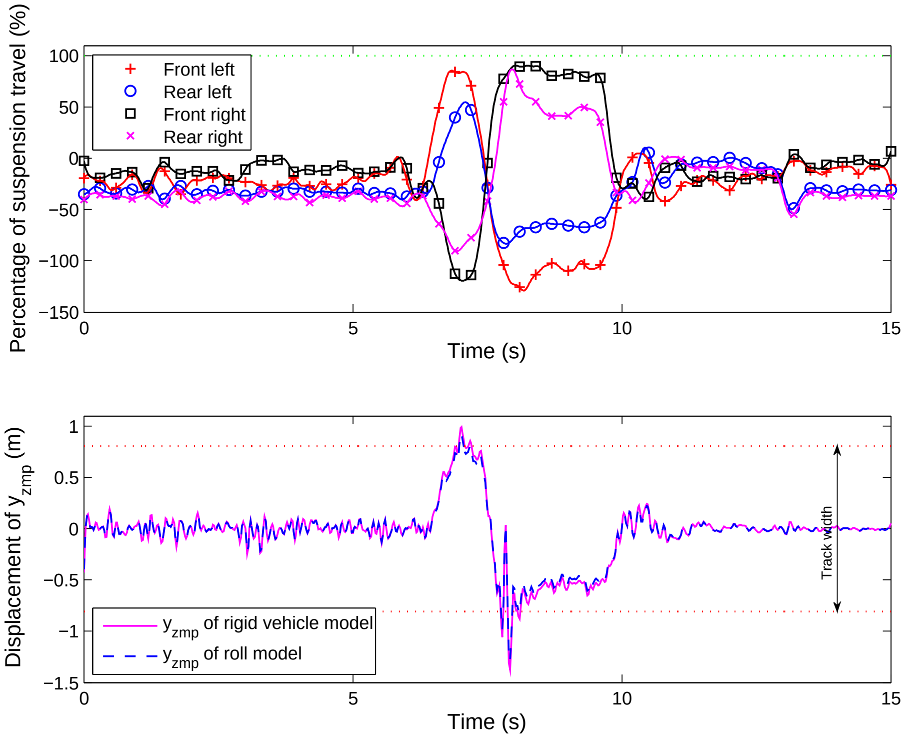

Figure 5.13: Percentage of suspension travel and displacements of y_{zmp} obtained from the test whose testing conditions are given in the first row of Table 5.3. The truck was driven on the flat road and excited by the Toyota J-turn at speed of 10 m/s, causing no wheel lift.

lifted, usually either one of the front wheels. The yellow areas indicate the two-wheel-lift regions. In the cases of the sliding truck, the sideslip is also illustrated as an indication of skidding.

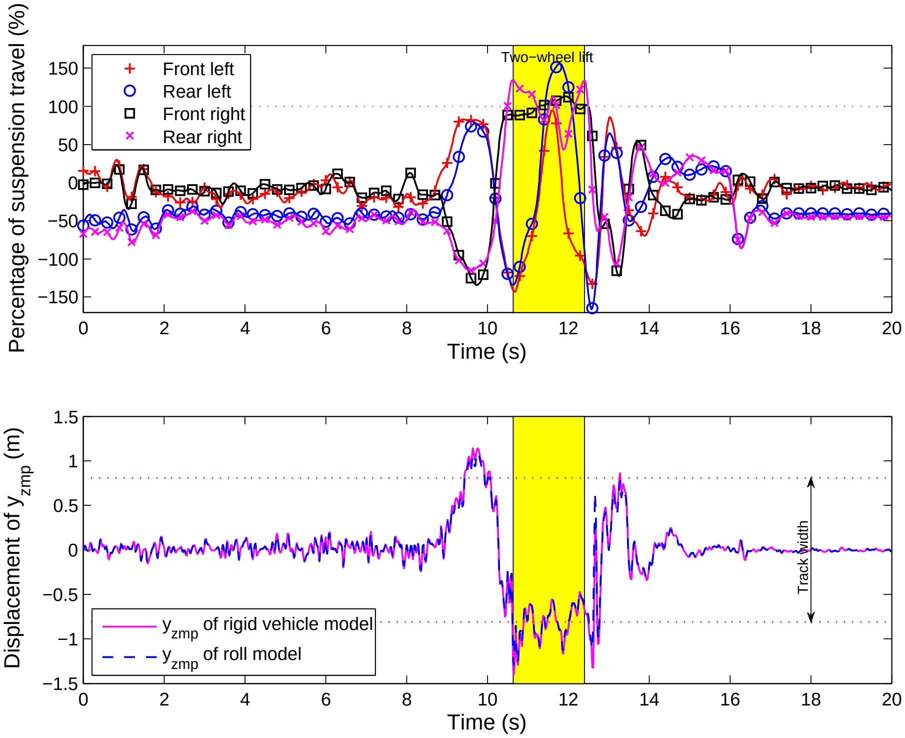

Figure 5.14: Percentage of suspension travel and displacements of y_{zmp} obtained from the test whose testing conditions are given in the second row of Table 5.3. The truck was driven on the flat road and excited by the Toyota J-turn at speed of 17 m/s, causing both of the right wheels of the truck to lift.

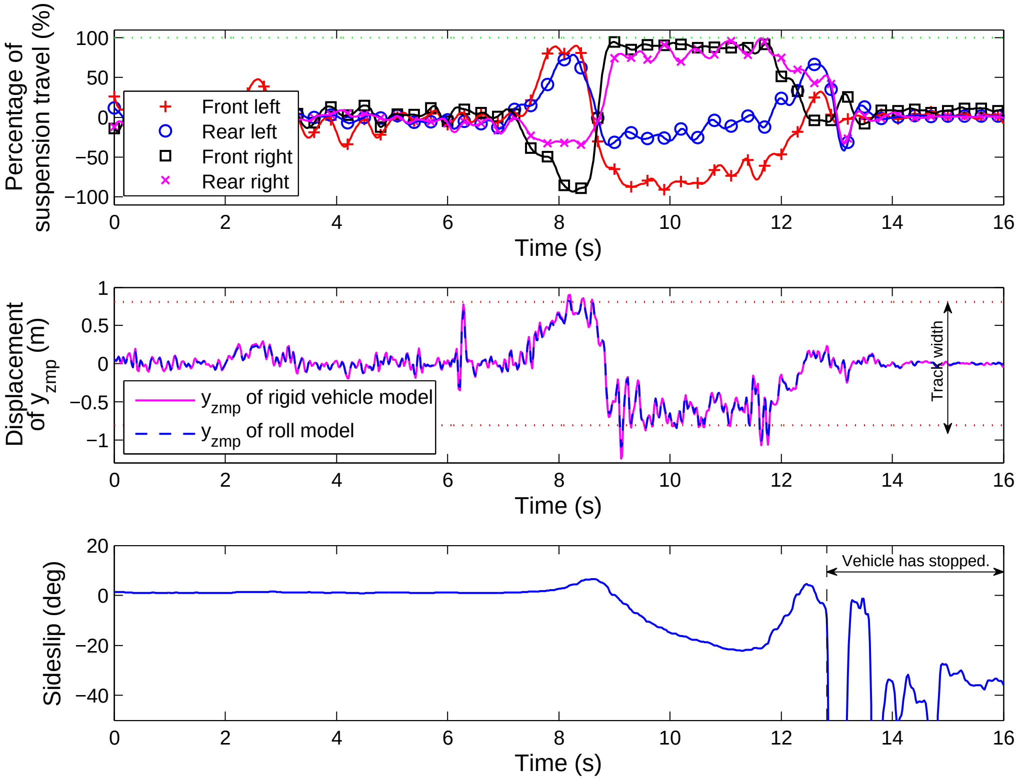

Figure 5.15: Percentage of suspension travel, displacements of y_{zmp}, and sideslip obtained from the test whose testing conditions are given in the third row of Table 5.3. The truck was driven on the flat road and excited by the Toyota J-turn at speed of 20 m/s, causing the truck to skid with no wheel lift.

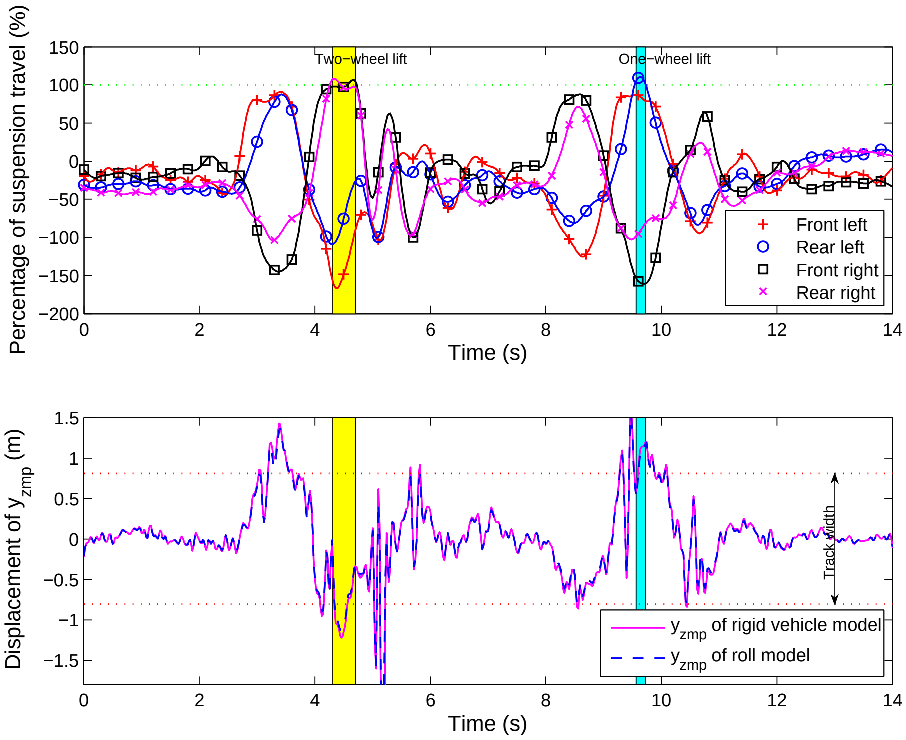

Figure 5.16: Percentage of suspension travel and displacements of y_{zmp} obtained from the test whose testing conditions are given in the fourth row of Table 5.3. The truck was driven on the flat road and excited by the double-lane-change maneuver at speed of 15.5 m/s, causing both of the right wheels of the truck to lift on the first turn, and only the rear left wheel to lift on the second turn.

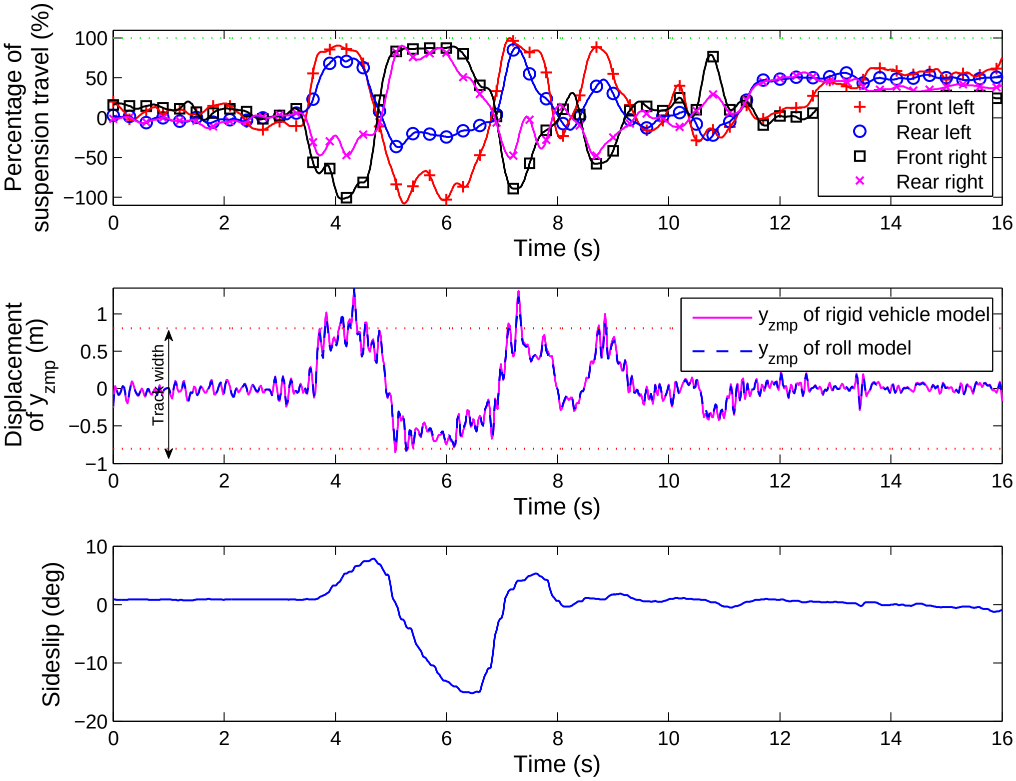

Figure 5.17: Percentage of suspension travel, displacements of y_{zmp}, and sideslip obtained from the test whose testing conditions are given in the fifth row of Table 5.3. The truck was driven on the flat road and excited by the double-lane-change maneuver at speed of 20 m/s, causing the truck to skid with no wheel lift.

5.3.2 Experimental Results on Banked Road

In this section, the experimental results performed on the banked road are provided. Figure 5.11 is a picture of the banked-road section used in all the banked-road tests. The banked road has an inclination of seven degrees. In the banked-road tests, the test truck was excited by only the Toyota-J turn due to limited space.

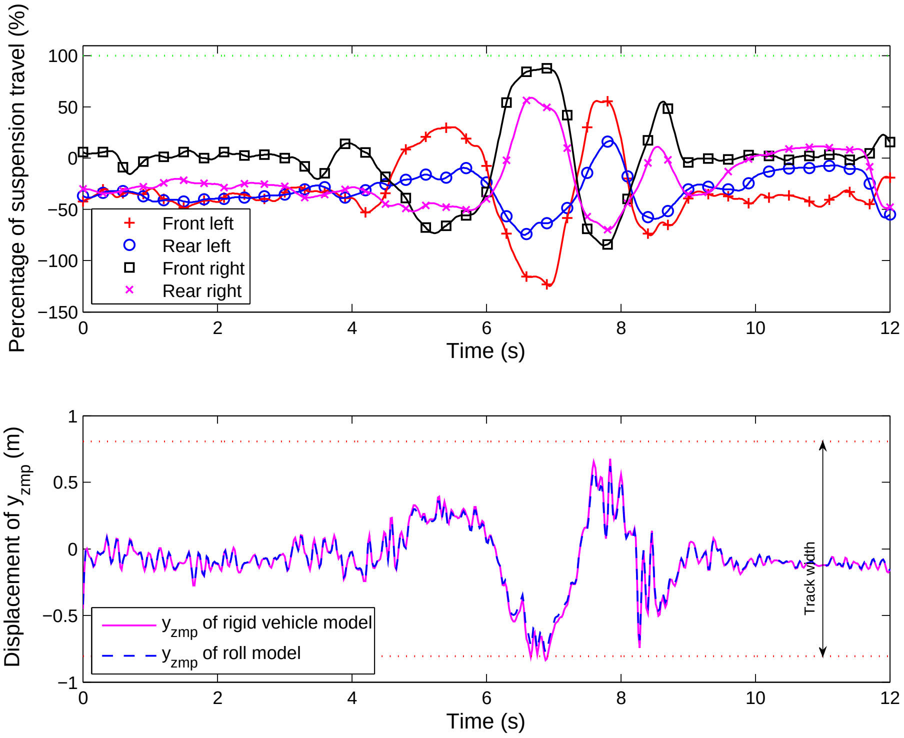

Figure 5.18: Percentage of suspension travel and displacements of y_{zmp} obtained from the test in which the truck was driven on the banked road and excited by the Toyota J-turn at speed of 7 m/s, causing no wheel lift.

Figure 5.18 shows the percentage of suspension travel and the displacements of y_{zmp} calculated from the rigid vehicle model (Eq. 2.18) and the vehicle roll model (Eq. 2.32). The results are taken from the test in which the truck performed the

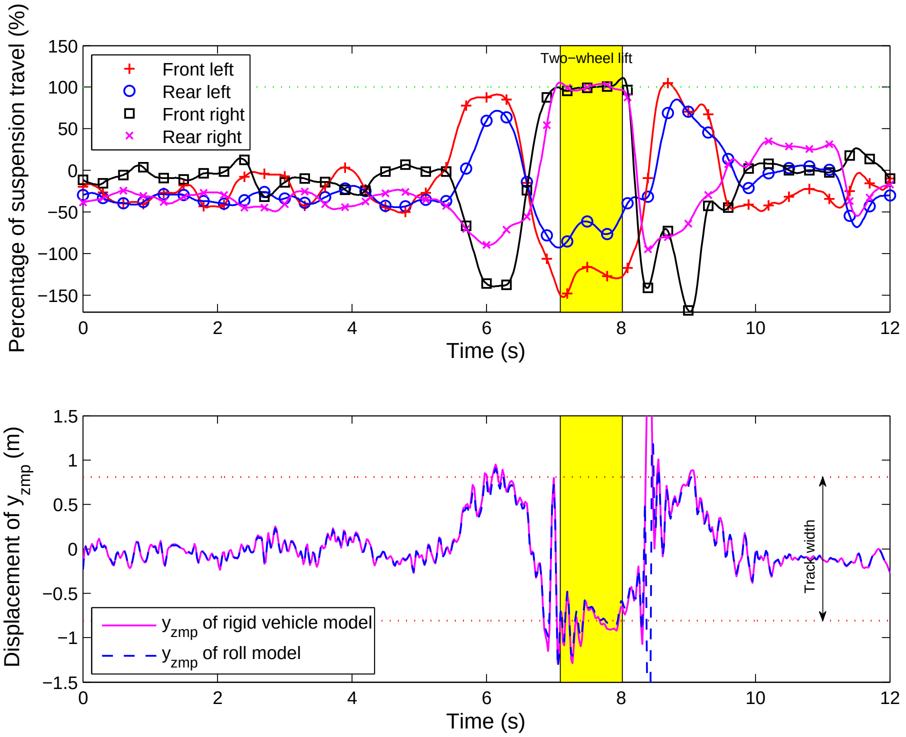

Figure 5.19: Percentage of suspension travel and displacements of y_{zmp} obtained from the test in which the truck was driven on the banked road and excited by the Toyota J-turn at speed of 12 m/s, causing both of the right wheels of the truck to lift.

Toyota J-turn on the banked road at the speed of 7 m/s, leading to no wheel lift. Figure 5.19 presents the results gathered from the test at the speed of 12 m/s. In this test, both of the right wheels of the truck were airborne during the Toyota J-turn. For the results shown in this section, an additional load of 448 kg was put on the truck's rack. The corresponding vehicle parameters used to compute the displacements of y_{zmp} are indicated in Table A.2.

In Figures 5.18 and 5.19, the percentage of suspension travel is represented in the top section of the plots. The lower section in the figures indicates the displacements of y_{zmp} of the rigid vehicle model and the vehicle roll model. The width between the dotted red lines is the track width of the truck. The yellow area in Figure 5.19 shows the wheel-liftoff region.

5.4 Discussion of Experimental Results

The experimental results are indeed consistent with the simulation results. There are a couple of observations that can be drawn from the experimental results. First, the displacements of y_{zmp} from both the rigid vehicle model and the vehicle roll model predict wheel liftoff quite well. The displacements of y_{zmp} estimated from both models are almost on top of each other and are very hard to distinguish. However, when one zooms in on the wheel-lift regions, one can see that the displacement of y_{zmp} estimated from the rigid vehicle model (Eq. 2.18) is slightly more conservative than the one obtained from the roll model (Eq. 2.32). This may happen since the roll model is more realistic than the rigid vehicle model, causing the behavior of the roll model to be closer to a real vehicle than that of the rigid vehicle model.

Additionally, Table 5.4 shows the effectiveness of the ZMP-based rollover indices obtained from both the rigid vehicle model and the vehicle roll model. The results in the table also support the above paragraph. Furthermore, from the results previously shown and the table, a number of false positives (the off-diagonal members in the table) can be noticed. These false positives may be caused by

Table 5.4: Truth table showing the effectiveness of the ZMP-based rollover indices.

Results	**Predicted**	**Rigid vehicle model**		**Vehicle roll model**	
		Actual		**Actual**	
		Yes	No	Yes	No
Figure 5.13	Yes	0	18	0	11
	No	0	210	0	217
Figure 5.14	Yes	45	40	40	36
	No	43	173	48	177
Figure 5.15	Yes	0	32	0	18
	No	0	269	0	283
Figure 5.16	Yes	12	67	10	55
	No	9	388	11	400
Figure 5.17	Yes	0	31	0	22
	No	0	370	0	379
Figure 5.18	Yes	0	3	0	0
	No	0	148	0	151
Figure 5.19	Yes	26	28	18	19
	No	20	167	28	176

the uncertainties in the estimated vehicle parameters and the state measurements. The reason that this hypothesis is proposed is that, once considering the simulation results wherein almost every vehicle parameter is precisely known, the ZMP-based rollover metrics can accurately predict vehicle rollover. To show how the uncertainties effect the calculation of y_{zmp}, a sensitivity analysis [71] based on the lateral acceleration and the height of the center of gravity was performed to determine the standard deviation of y_{zmp}. Figure 5.20 illustrates the displacement of y_{zmp} computed from the rigid vehicle model along with the uncertainty of three standard deviations. From the figure, although it is not quite conclusive, one can see that the uncertainties in the parameters and measurements can be a possible cause of the false positives.

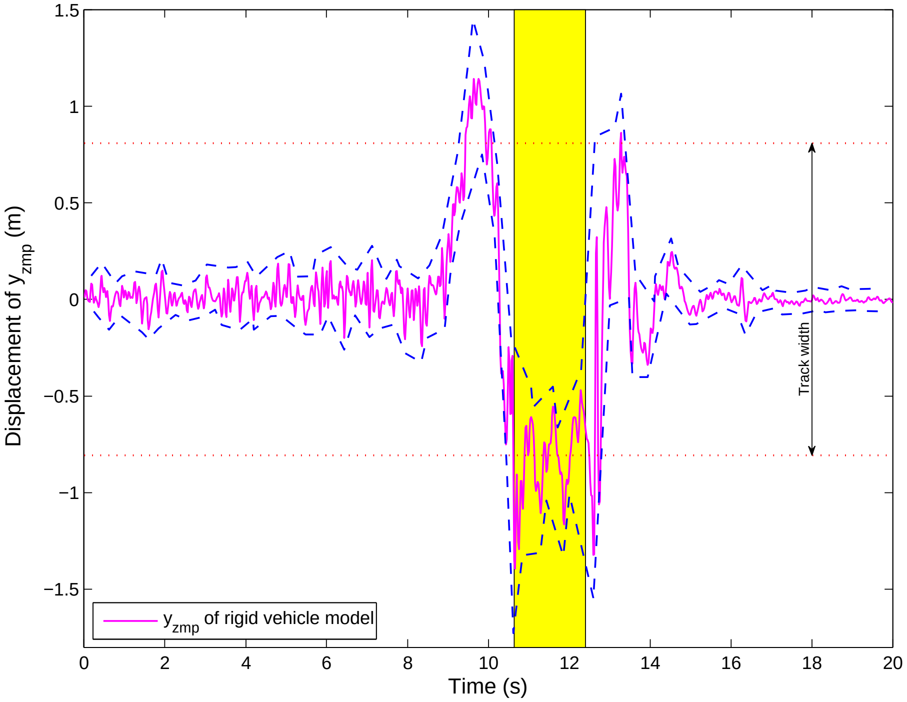

Figure 5.20: Displacement of y_{zmp} of the rigid vehicle model from Figure 5.14 with the uncertainty of three standard deviations.

The second observation is that the displacement of y_{zmp} during wheel liftoff is a relatively flat straight line. Since there is no external force applied to the vehicle, the only place that reaction forces can physically act after the wheel liftoff is on the edge of the vehicle, allowing the vehicle to rock itself on its wheels due to the effects of its own momentum. Thus, we see that the ZMP method also saturates as do other metrics (i.e. load transfer ratio and stability moment), but this saturation is due to physics and not due to the way that the metric is defined.

During the saturation, one can also see that there are oscillations in the displacement of y_{zmp}. These oscillations are evident particularly in Figures 5.14 and 5.15. To reduce this oscillation effect, a low-pass filter can be applied. The y_{zmp} of the rigid vehicle model from Figure 5.14 were processed by passing through a a set of low-pass filters, and the processed results are shown in Figure 5.21. Figure 5.22 clearly shows the effects of the low-pass filters that have different cutoff frequencies on the accuracy of rollover prediction by considering the percentage of the off-diagonal members in the truth table (Table 5.4). The filters certainly reduce the oscillation and improve the prediction accuracy. However, the cutoff frequency cannot be too low, since it will introduce an unacceptable time delay to the output and/or worsen the prediction accuracy.

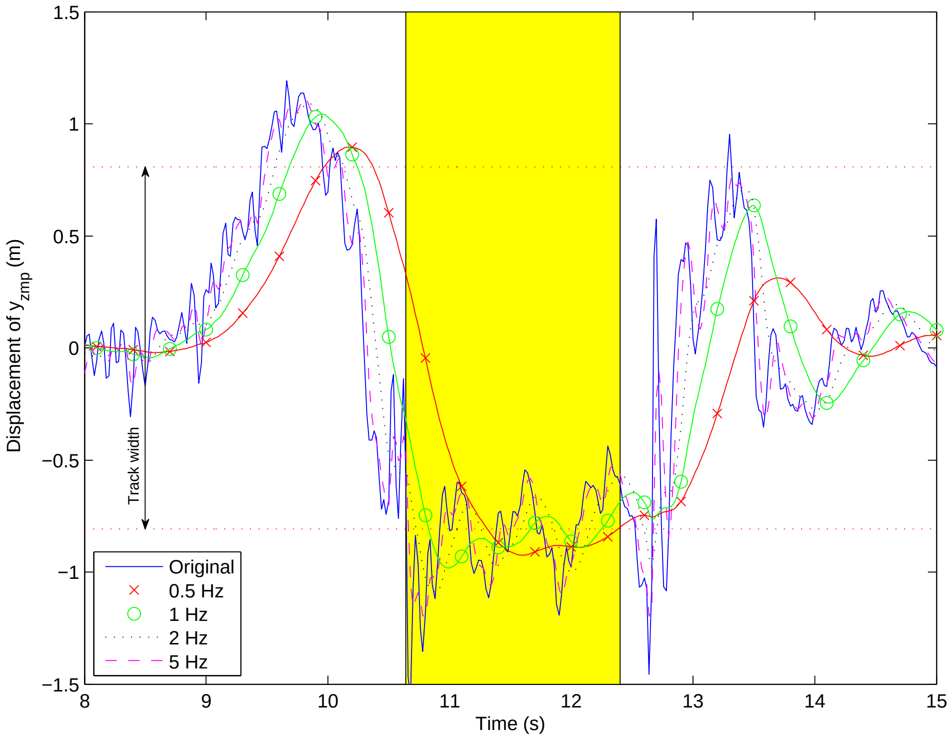

Figure 5.21: Effects of cutoff frequency on the time-domain data.

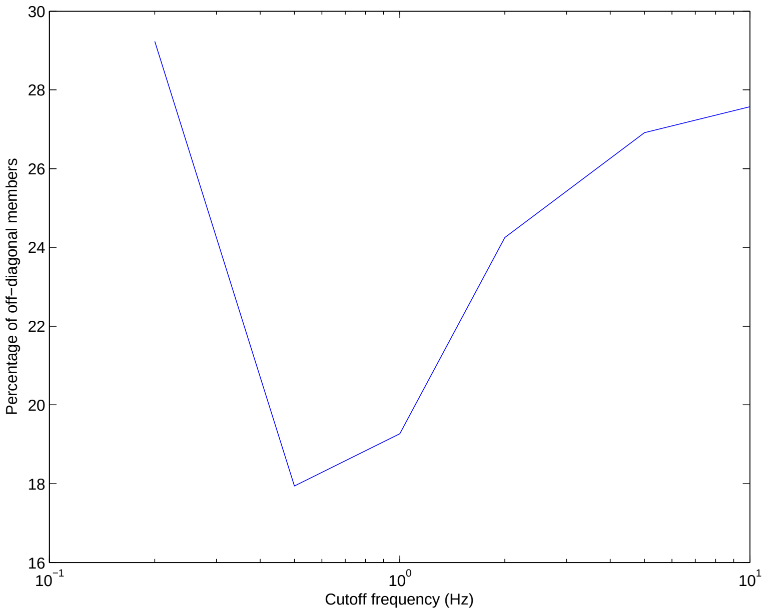

Figure 5.22: Effects of cutoff frequency on percentage of off-diagonal members.

5.5 Analyses of Experimental Results

This section considers a more detailed analysis of the experimental results. First, the influence of each term on the calculations of the displacements of y_{zmp} from the rigid vehicle model and the vehicle roll model are examined. This is followed by the investigation on how the unsprung mass and the sprung mass of the vehicle roll model contribute to the calculation of the displacement of y_{zmp}. The last analysis gives a guideline on how to simplify the y_{zmp} expressions. Since all of the test results are consistent throughout the experiments, the analyses are only conducted on a couple of scenarios in which the truck was excited by the Toyota J-turn on either the flat road or banked road. In these scenarios, both of the truck's right wheels lifted off the ground during the turn.

5.5.1 Contributions of Individual Term in y_{zmp} Expressions

The mechanisms behind vehicle rollover are described in this section. To proceed with the analysis, the equation of y_{zmp} of the rigid vehicle model is recalled.

$$\begin{aligned} y_{zmp} \;=\; & \{\, \overbrace{mg\cos(\theta)\sin(\phi_r)\,[T\,|\tan(\phi_r-\phi_t)|+2h]}^{\text{weight}} - \overbrace{ma_{Gy}\,[T\,|\tan(\phi_r-\phi_t)|+2h]}^{\text{lateral acceleration}} \\ & - \overbrace{2I_{xx}\alpha_x}^{\text{roll acceleration}} + 2I_{xz}\alpha_z + 2I_{yz}(q^2-r^2) + 2(I_{xz}+I_{yy}-I_{zz})qr \,\} \\ & /\, \{\, 2m\,[\, g\cos(\theta)\cos(\phi_t)\sec(\phi_r-\phi_t) - a_{Gy}\tan(\phi_r-\phi_t) - a_{Gz} \,]\,\} \end{aligned} \tag{5.2}$$

The first, second, and third terms in the numerator of the y_{zmp} expression are the contributions from the vehicle weight, the lateral acceleration, and the roll acceleration, respectively. The remaining terms of the numerator in the equation are due to the cross-product mass moments of inertia, which are typically ignored. The contributions of the vehicle weight, the lateral acceleration, and the roll acceleration during wheel liftoff are compared in Figures 5.23 and 5.24, which are the cases of the flat road and the banked road, respectively. Besides, it is interesting to investigate the results from the case of the skidding truck, which is presented in Figure 5.25.

In the similar fashion, the y_{zmp} expression of the vehicle roll model is recalled.

$$y_{zmp} \;=\; \{\, \overbrace{m_s g\,[\,T\sin(\phi_u)\cos(\theta)\,|\tan(\phi_t-\phi_u)| - 4h_r\sin\left(\frac{\phi}{2}\right)\cos\left(\frac{\phi}{2}+\phi_u\right)\cos(\theta)}^{\text{sprung mass's weight}}$$

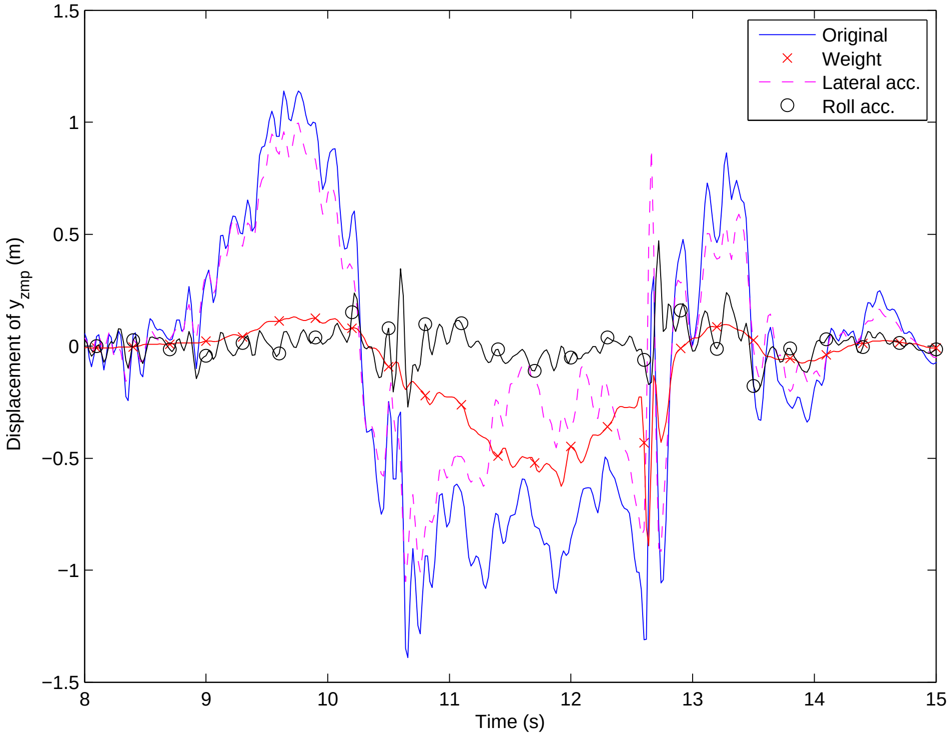

Figure 5.23: Contributions of individual term in the y_{zmp} expression of the rigid vehicle model obtained from the test whose testing conditions are given in the second row of Table 5.3. The truck was driven on the flat road and excited by the Toyota J-turn at speed of 17 m/s, causing both of the right wheels of the truck to lift.

$$
\begin{aligned}
&+\overbrace{2h_s\sin(\phi+\phi_u)\cos(\theta)\,]}^{\text{term in sprung mass's weight}}\\
&+\overbrace{m_u g\,[\,T\sin(\phi_u)\cos(\theta)\,|\tan(\phi_t-\phi_u)|+2h_u\sin(\phi_u)\cos(\theta)\,]}^{\text{unsprung mass's weight}}\\
&-\overbrace{m_s a_{sy}\,[\,T\,|\tan(\phi_t-\phi_u)|+4h_r\sin^2\left(\frac{\phi}{2}\right)+2h_s\cos(\phi)\,]}^{\text{sprung mass's lateral acceleration}}\\
&-\overbrace{m_u a_{uy}\,[\,T\,|\tan(\phi_t-\phi_u)|+2h_u\,]}^{\text{unsprung mass's lateral acceleration}}\\
&+\overbrace{2m_s a_{sz}(h_r-h_s)\sin(\phi)}^{\text{sprung mass's vertical acceleration}}-\overbrace{2I_{xx_s}\alpha_{sx}}^{\text{roll acc. of } m_s}-\overbrace{2I_{xx_u}\alpha_{ux}}^{\text{roll acc. of } m_u}+2(I_{xz_s}+I_{xz_u})\alpha_z\\
&+2(I_{yz_s}+I_{yz_u})q^2-2(I_{yz_s}+I_{yz_u})r^2+2I_{xz_s}p_s q+2I_{xz_u}p_u q
\end{aligned}
$$

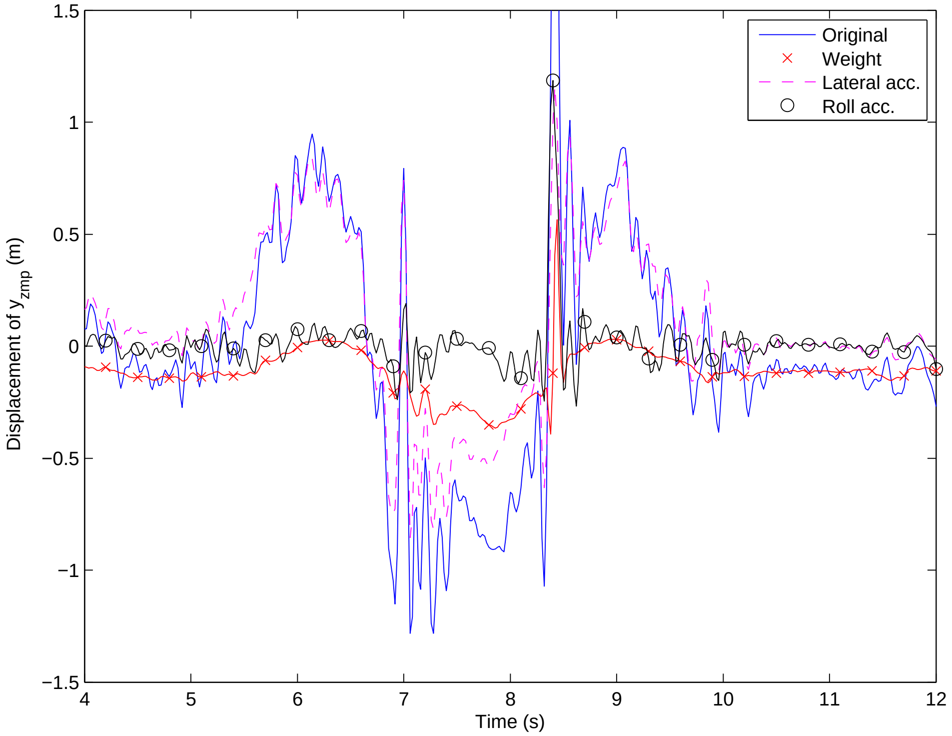

Figure 5.24: Contributions of individual term in the y_{zmp} expression of the rigid vehicle model obtained from the test in which the truck was driven on the banked road and excited by the Toyota J-turn at speed of 12 m/s, causing both of the right wheels of the truck to lift.

$$+2(I_{yy_s} + I_{yy_u} - I_{zz_s} - I_{zz_u})qr \ \}$$

$$/ \{ \ 2 \, [\ m_s(g\cos(\theta)\cos(\phi_t)\sec(\phi_t - \phi_u) - a_{sz} + a_{sy}\tan(\phi_t - \phi_u))$$

$$+m_u(g\cos(\theta)\cos(\phi_t)\sec(\phi_t - \phi_u) - a_{uz} + a_{uy}\tan(\phi_t - \phi_u)) \ ] \ \} \qquad (5.3)$$

From the above equation, the terms in the numerator are in the following sequence: sprung mass's weight, unsprung mass's weight, lateral acceleration of sprung mass, lateral acceleration of unsprung mass, vertical acceleration of sprung mass, roll acceleration of sprung mass, roll acceleration of unsprung mass, and the negligible

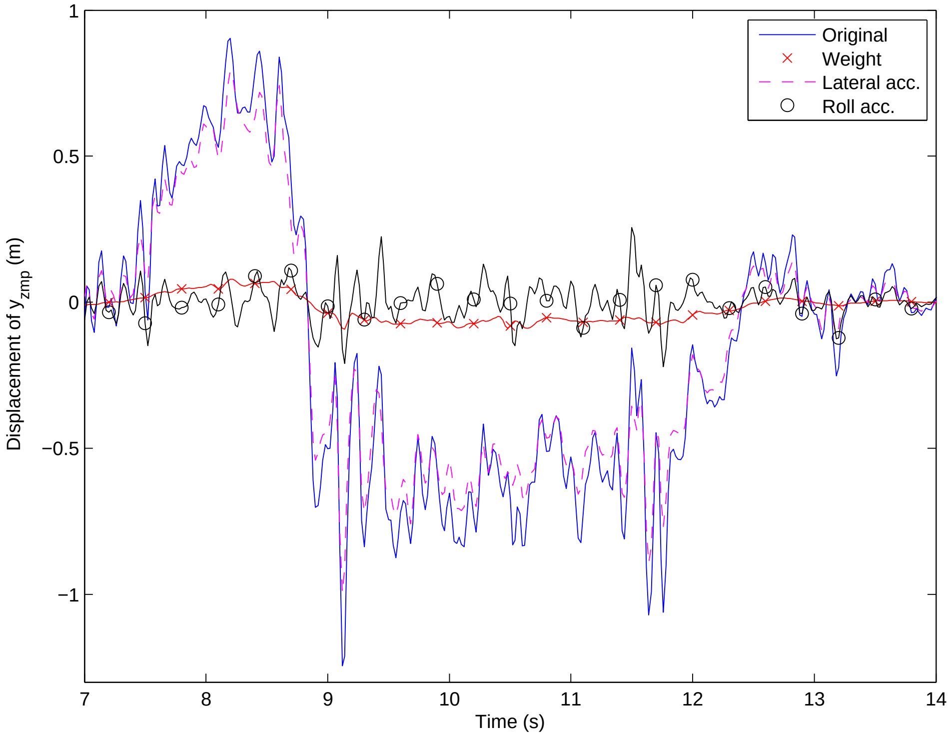

Figure 5.25: Contributions of individual term in the y_{zmp} expression of the rigid vehicle model obtained from the test in which the truck was driven on the flat road and excited by the Toyota J-turn at speed of 20 m/s, causing the truck to skid.

remainder that is related to the cross-product terms in Eq. 2.30. The terms related only to the sprung mass are considered, since the unsprung-mass terms may be ignored. An analysis on this issue will be given in the next section. The effects of the individual term corresponding to the sprung mass are plotted in Figures 5.26 and 5.27, which are obtained from the tests on the flat road and the banked road, respectively. Further, the results from the case of the skidding truck is presented in Figure 5.28.

For these plots (Figures 5.23, 5.24, 5.26, and 5.27), one can see that the most influential term during vehicle rollover is the lateral acceleration. The same obser-

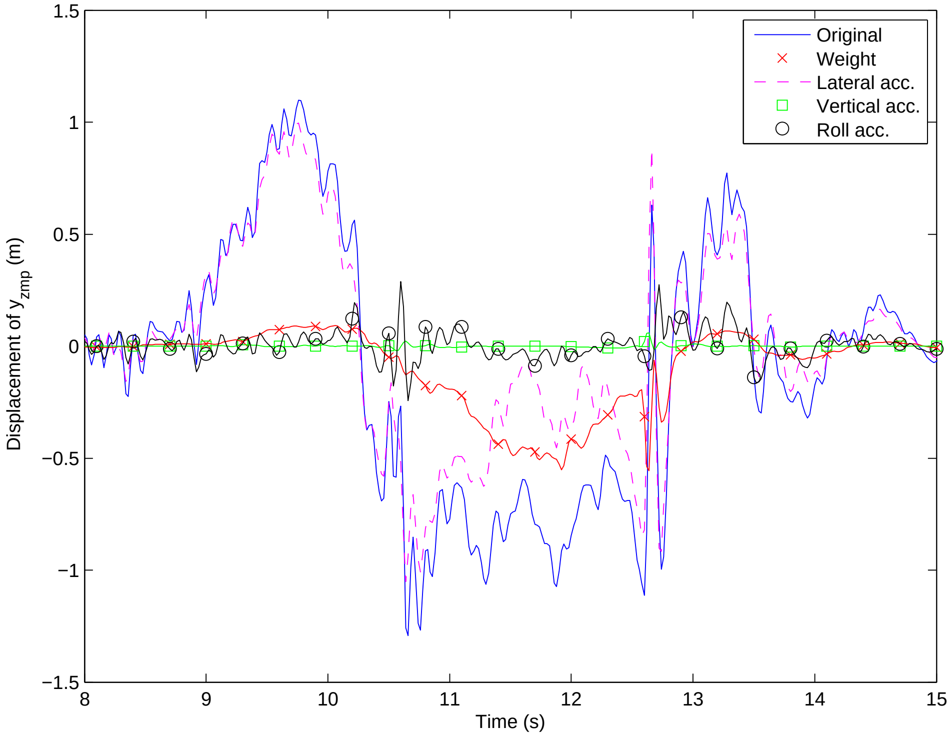

Figure 5.26: Contributions of individual term of the sprung mass in the y_{zmp} expression of the vehicle roll model obtained from the test whose testing conditions are given in the second row of Table 5.3. The truck was driven on the flat road and excited by the Toyota J-turn at speed of 17 m/s, causing both of the right wheels of the truck to lift.

vation can also be seen in the case of the skidding truck in Figures 5.25 and 5.28. This finding is particularly convenient, since the majority of the terms corresponding to the lateral acceleration in the y_{zmp} expressions are relatively straightforward to estimate. Further, it is evident that the contributions of the roll acceleration term is not that significant. This fact is also helpful, since the vehicle parameters relevant to the roll acceleration, particularly the mass moments of inertia, are not easy to measure. Moreover, if the mass moments of inertia is underestimated or overestimated by 20-30% of the true value, the displacements of y_{zmp} are still

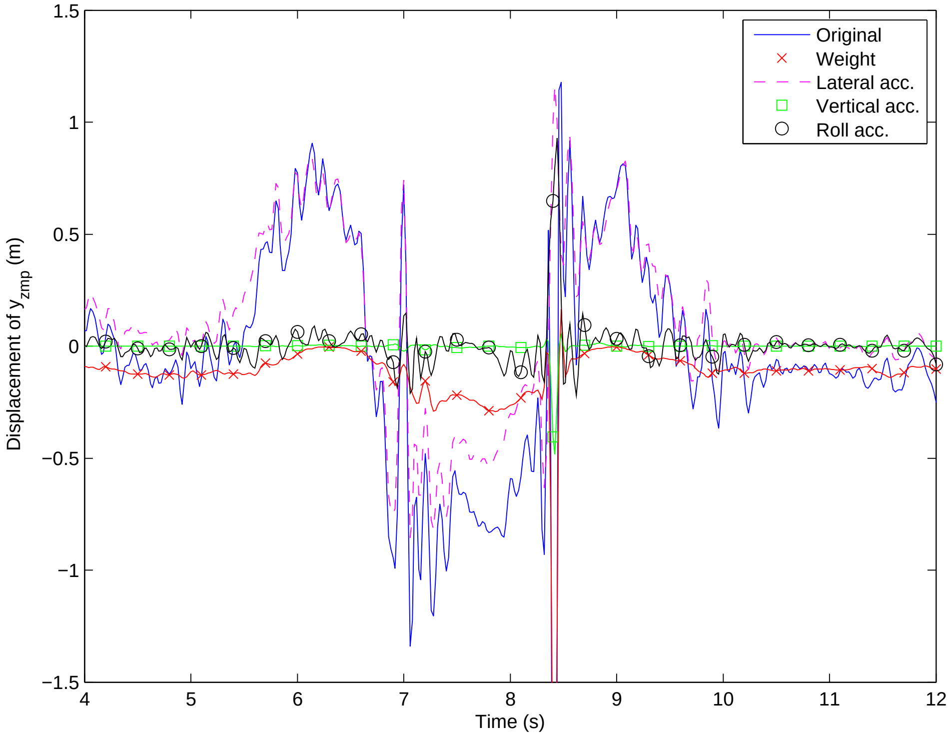

Figure 5.27: Contributions of individual term of the sprung mass in the y_{zmp} expression of the vehicle roll model obtained from the test in which the truck was driven on the banked road and excited by the Toyota J-turn at speed of 12 m/s, causing both of the right wheels of the truck to lift.

somewhat in an acceptable range. Next, considering the weight term, we observe that it contributes to the bias in the y_{zmp} calculation, especially with the presence of terrain. Although the inclination of the banked road in the experiments is not steep, it is quite clear to see how the terrain affects vehicle rollover prediction. The weight term becomes more dominant once the roll angle or the angle of terrain becomes larger, as one can see in the results.

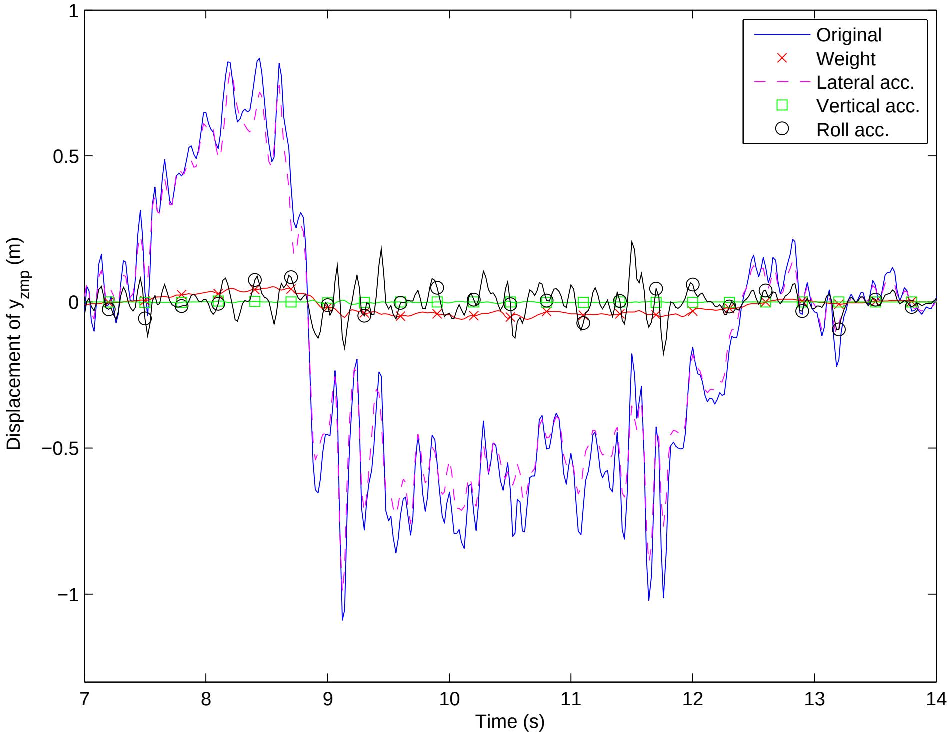

Figure 5.28: Contributions of individual term in the y_{zmp} expression of the vehicle roll model obtained from the test in which the truck was driven on the flat road and excited by the Toyota J-turn at speed of 20 m/s, causing the truck to skid.

5.5.2 Contributions of Unsprung Mass and Sprung Mass in y_{zmp} Expressions

In the vehicle roll model, a vehicle is assumed to consist of two bodies: the unsprung mass and sprung mass. In this section, the contributions of these two bodies are investigated. Figure 5.29 shows the influence of the unsprung mass and the sprung mass in the calculation of the displacement of y_{zmp}. The results in this figure were obtained from the test conducted on the flat road. The results of the banked-road test are illustrated in Figure 5.30.

From Figures 5.29 and 5.30, it is clear that the dynamics of the sprung mass

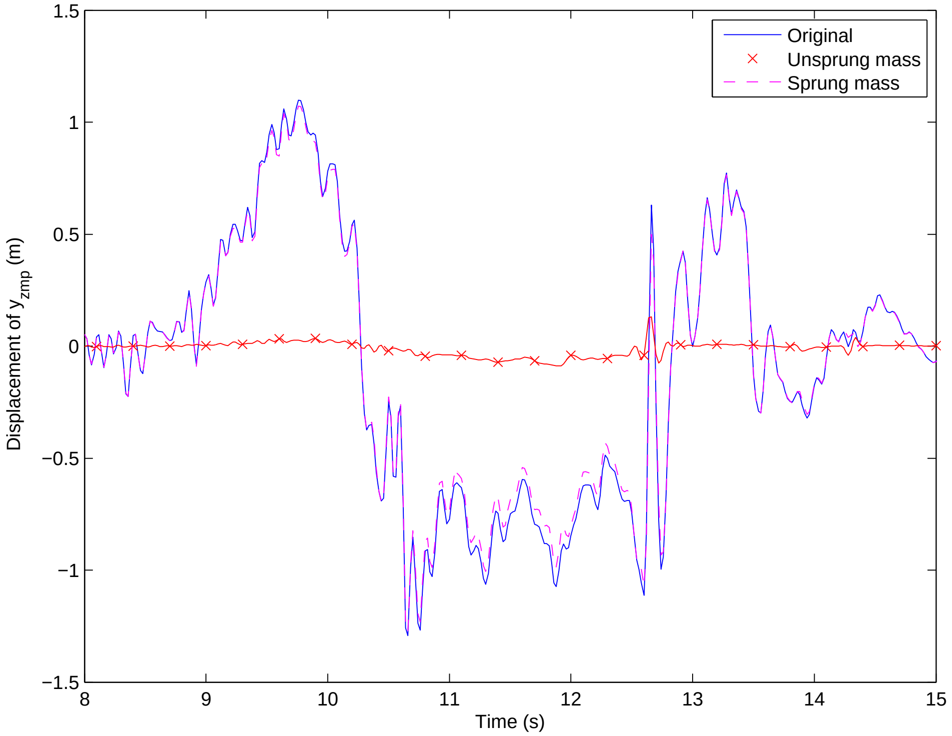

Figure 5.29: Contributions of the unsprung mass and the sprung mass in the y_{zmp} expression of the vehicle roll model obtained from the test whose testing conditions are given in the second row of Table 5.3. The truck was driven on the flat road and excited by the Toyota J-turn at speed of 17 m/s, causing both of the right wheels of the truck to lift.

considerably overshadow those of the unsprung mass. Even on the banked road, the effects of the unsprung-mass terms are negligible.

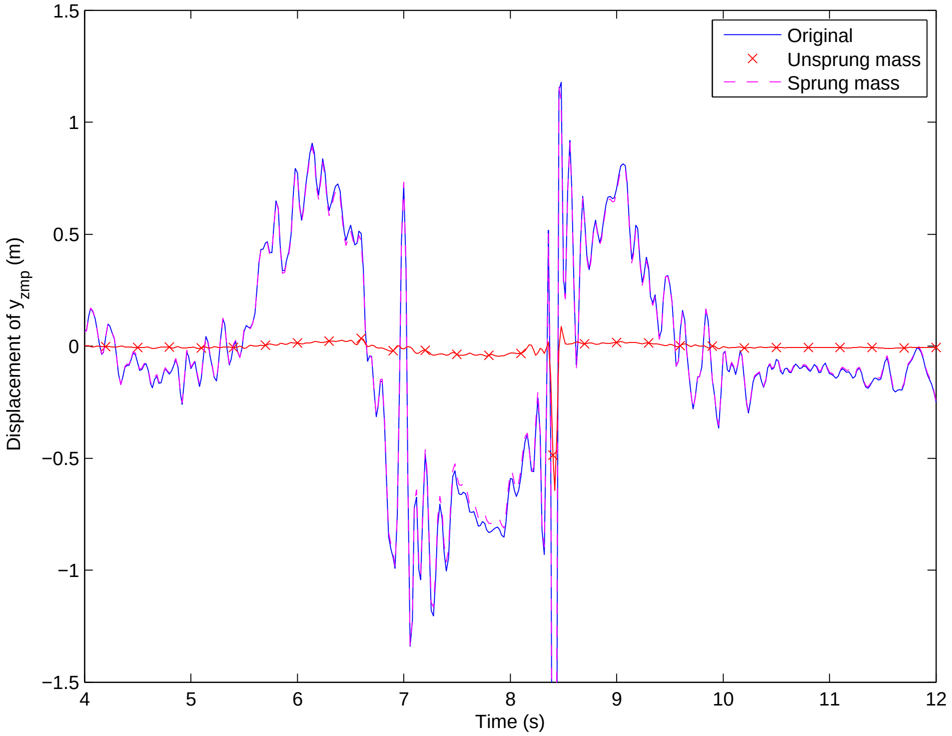

Figure 5.30: Contributions of the unsprung mass and the sprung mass in the y_{zmp} expression of the vehicle roll model obtained from the test in which the truck was driven on the banked road and excited by the Toyota J-turn at speed of 12 m/s, causing both of the right wheels of the truck to lift.

5.5.3 Contributions of Combined Terms in y_{zmp} Expressions

This section provides a set of simplified yet accurate ZMP-based rollover prediction indices obtained from the rigid vehicle model and the vehicle model. There are a couple of advantages gained from reducing the complexity of the mathematical representations of the location of the ZMP. Not only is the number of sensors installed on a vehicle to compute the displacement of y_{zmp} reduced, but it also saves time, since fewer procedures are required to measure vehicle parameters. To simplify the y_{zmp} expressions, the individual terms considered in Section 5.5.1 are paired with the other terms in the y_{zmp} expressions. Once the terms are combined, the displacement of y_{zmp} determined from the combined terms is plotted against that computed from the original expression. The comparison gives an idea of how accurately the simplified y_{zmp} expression predicts imminent vehicle rollover. It is known from Section 5.5.1 that the most, second most, and third most dominant terms behind vehicle rollover are the lateral acceleration, the vehicle's weight, and the roll acceleration, respectively; hence, the influence of the combination of these three states are investigated in this section. In the case of the simplified expression which combines the lateral acceleration and the weight, Eq. 5.2 can be reduced to:

$$\begin{aligned} y_{zmp} \;=\;& \{mg\cos(\theta)\sin(\phi_r)\,[T\,|\tan(\phi_r-\phi_t)|+2h] - ma_{Gy}\,[T\,|\tan(\phi_r-\phi_t)|+2h]\} \\ & /\,\{\,2m\,[\,g\cos(\theta)\cos(\phi_t)\sec(\phi_r-\phi_t) - a_{Gy}\tan(\phi_r-\phi_t) - a_{Gz}\,]\,\} \end{aligned} \tag{5.4}$$

If the roll acceleration is included in the above equation, the equation becomes:

$$\begin{aligned} y_{zmp} \;=\;& \{\,mg\cos(\theta)\sin(\phi_r)\,[T\,|\tan(\phi_r-\phi_t)|+2h] - ma_{Gy}\,[T\,|\tan(\phi_r-\phi_t)|+2h] \\ & -2I_{xx}\alpha_x\,\}\,/\,\{\,2m\,[\,g\cos(\theta)\cos(\phi_t)\sec(\phi_r-\phi_t) - a_{Gy}\tan(\phi_r-\phi_t) - a_{Gz}\,]\,\} \end{aligned} \tag{5.5}$$

Figure 5.31 shows the displacements of y_{zmp} during wheel lift on the flat road. The results from the banked-road test are illustrated in Figure 5.33. In the figures,

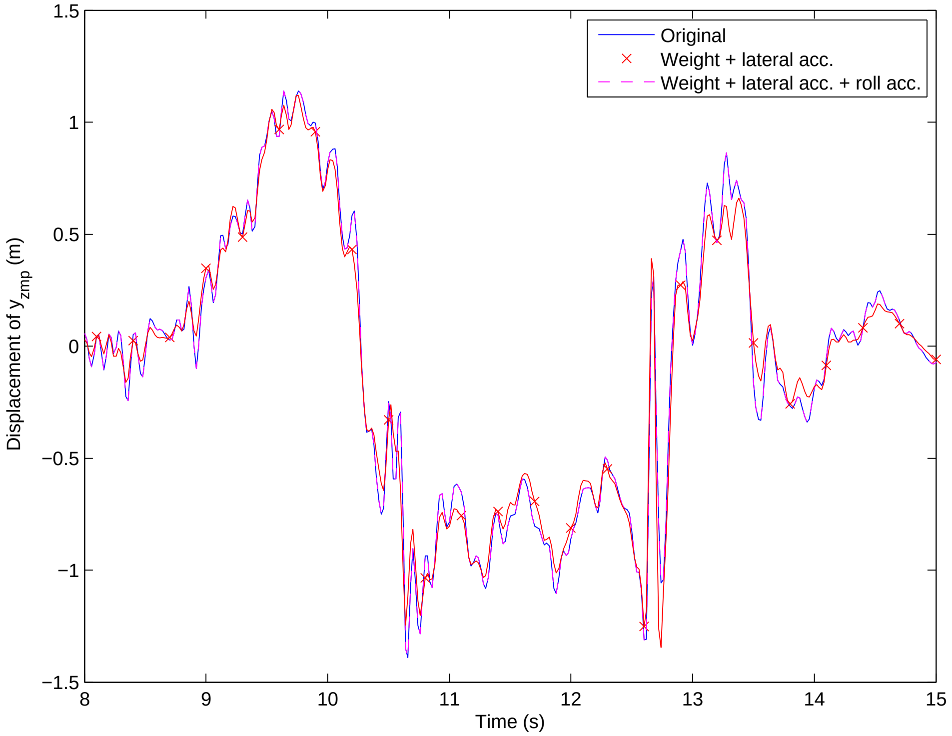

Figure 5.31: Contributions of combined terms in the y_{zmp} expression of the rigid vehicle model obtained from the test whose testing conditions are given in the second row of Table 5.3. The truck was driven on the flat road and excited by the Toyota J-turn at speed of 17 m/s, causing both of the right wheels of the truck to lift.

the displacements of y_{zmp} were computed from the rigid vehicle model (Eq. 5.2), the combination of the lateral acceleration and the weight (Eq. 5.4), and the combination of the lateral acceleration, the weight, and the roll acceleration (Eq. 5.5). Figures 5.33 and 5.34 show the errors between the original expression and the combined terms for the flat-road and banked-road cases, respectively. From the error plots, it is clear that the rollover index based on the combination of the lateral acceleration, the weight, and the roll acceleration is almost as good as the original one.

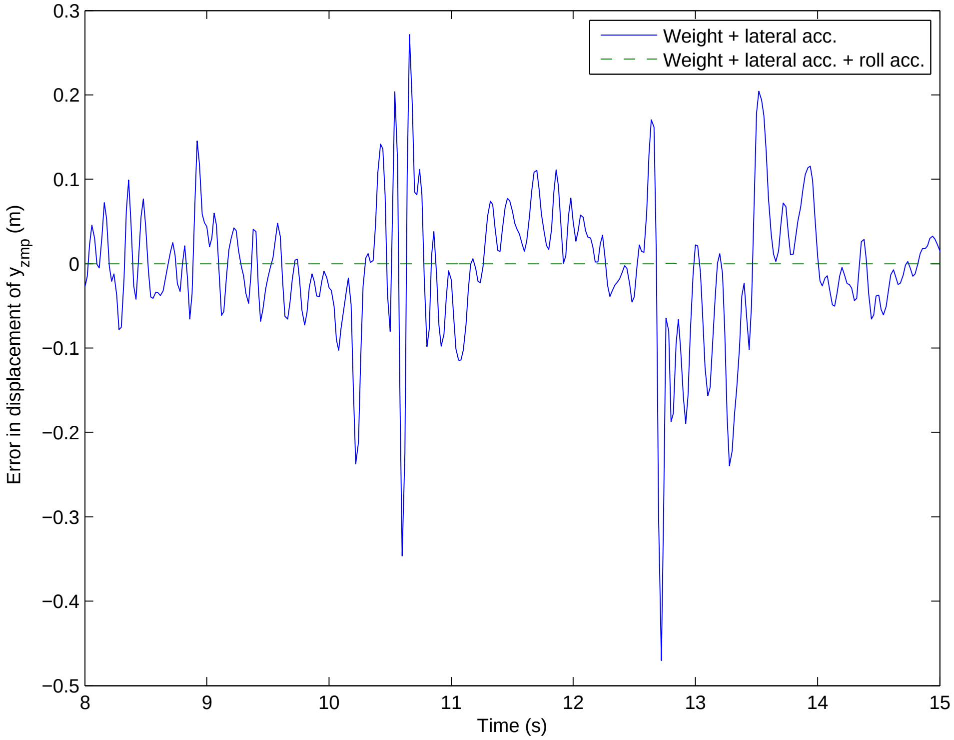

Figure 5.32: Errors between the full expression of y_{zmp} of the rigid vehicle model and the combined terms in Figure 5.31.

Next, the case of the vehicle roll model is considered. The analysis for this case is conducted in a similar fashion as in the case of the rigid vehicle model. Furthermore, the analysis performed in the previous section shows that the contribution of the unsprung mass is negligible; thus, only the influence of the sprung mass is considered. With these facts in mind, and considering only the sprung mass's lateral acceleration and weight, Eq. 5.3 may be rewritten as:

$$\begin{aligned} y_{zmp} &= \{\, m_s g \,[\, T \sin(\phi_u) \cos(\theta) \, |\tan(\phi_t - \phi_u)| - 4h_r \sin\left(\frac{\phi}{2}\right) \cos\left(\frac{\phi}{2} + \phi_u\right) \cos(\theta) \\ &\quad +2h_s \sin(\phi + \phi_u) \cos(\theta) \,] \end{aligned}$$

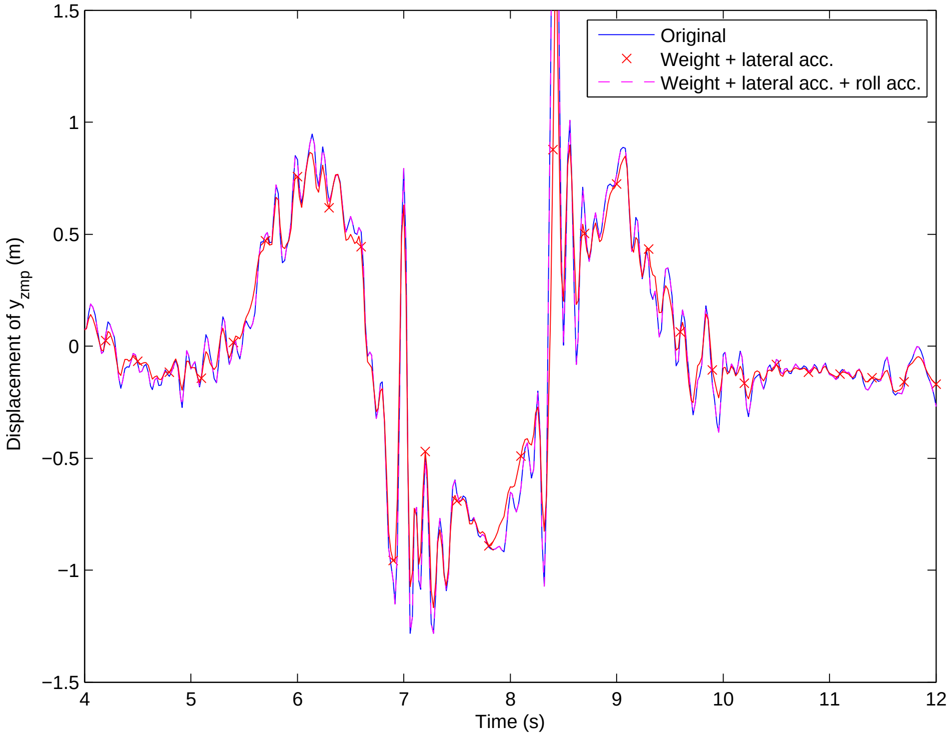

Figure 5.33: Contributions of combined terms in the y_{zmp} expression of the rigid vehicle model obtained from the test in which the truck was driven on the banked road and excited by the Toyota J-turn at speed of 12 m/s, causing both of the right wheels of the truck to lift.

$$-m_s a_{sy}\,[\,T\,|\tan(\phi_t-\phi_u)| + 4h_r\sin^2\left(\frac{\phi}{2}\right) + 2h_s\cos(\phi)\,]\,\}$$

$$/\,\{2\,[m_s(g\cos(\theta)\cos(\phi_t)\sec(\phi_t-\phi_u) - a_{sz} + a_{sy}\tan(\phi_t-\phi_u))]\} \qquad (5.6)$$

Further, if the roll acceleration of the sprung mass is added into consideration, the above equation becomes:

$$y_{zmp} \;=\; \{\,m_s g\,[\,T\sin(\phi_u)\cos(\theta)\,|\tan(\phi_t-\phi_u)| - 4h_r\sin\left(\frac{\phi}{2}\right)\cos\left(\frac{\phi}{2}+\phi_u\right)\cos(\theta)$$

$$+2h_s\sin(\phi+\phi_u)\cos(\theta)\,]$$

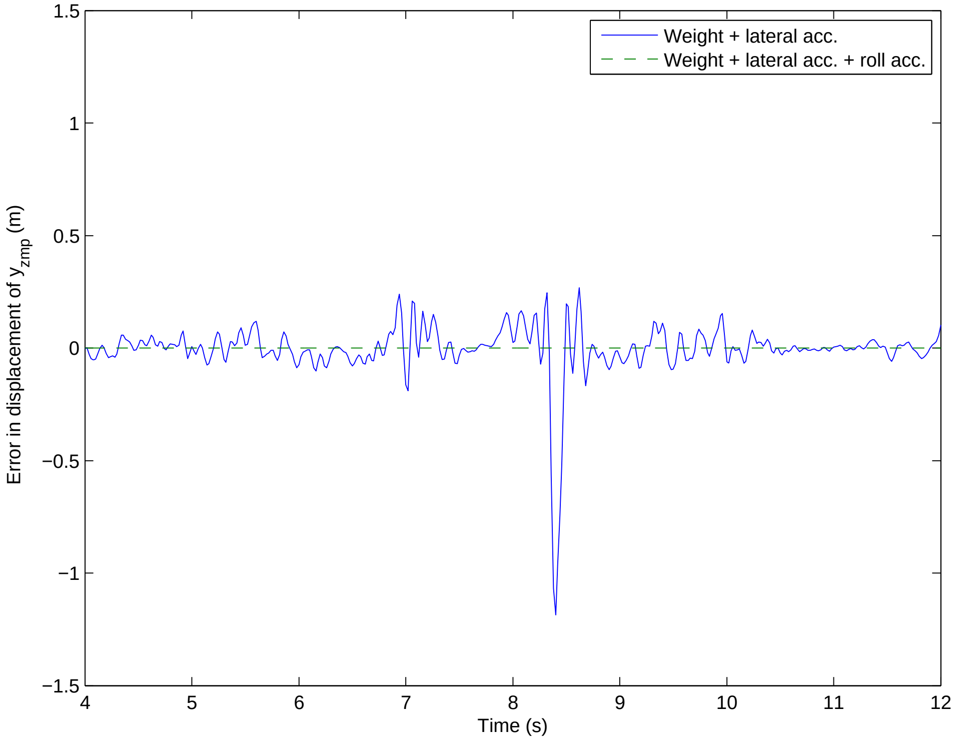

Figure 5.34: Errors between the full expression of y_{zmp} of the rigid vehicle model and the combined terms in Figure 5.33.

$$-m_s a_{sy}\left[\, T\left|\tan(\phi_t-\phi_u)\right| + 4h_r\sin^2\left(\frac{\phi}{2}\right) + 2h_s\cos(\phi) - 2I_{xx_s}\alpha_{sx}\,\right]\}$$

$$/\left\{2\left[m_s(g\cos(\theta)\cos(\phi_t)\sec(\phi_t-\phi_u) - a_{sz} + a_{sy}\tan(\phi_t-\phi_u))\right]\right\} \tag{5.7}$$

The displacements of y_{zmp} calculated from Eqs. 5.3, 5.6, and 5.7 are plotted for the flat road (Figure 5.35) and the banked road (Figure 5.37). The displacement differences from the full expression of y_{zmp} are shown in Figures 5.36 and 5.38. These results show a trend similar to the ones obtained from the rigid vehicle model. The roll index based on the combination of the lateral acceleration, the weight, and the roll acceleration provides adequate accuracy to predict vehicle

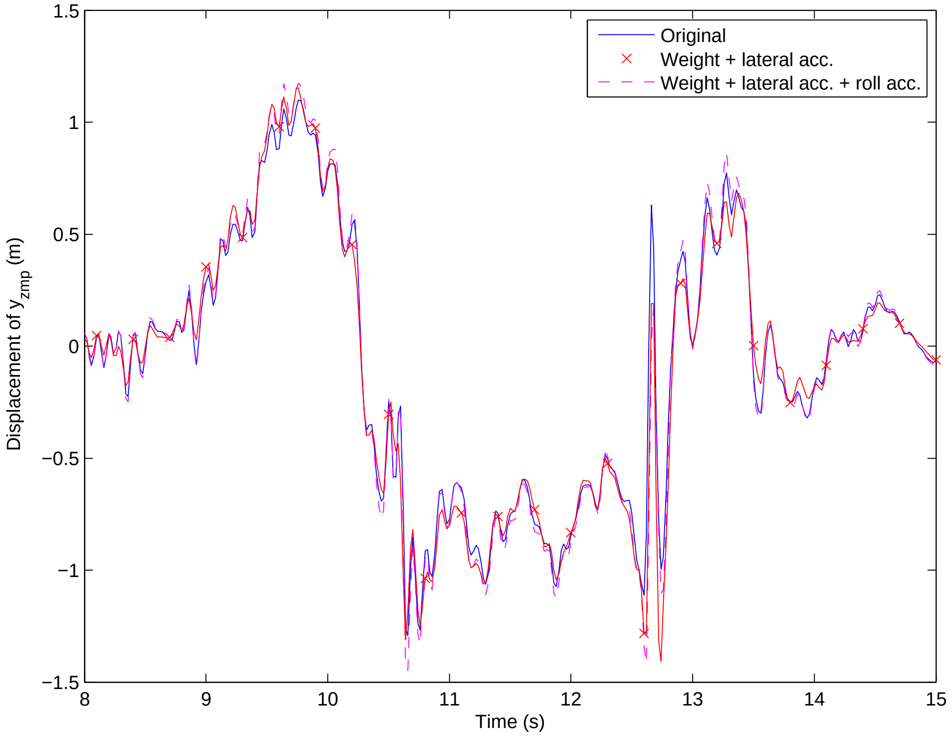

Figure 5.35: Contributions of combined terms in the y_{zmp} expression of the vehicle roll model obtained from the test whose testing conditions are given in the second row of Table 5.3. The truck was driven on the flat road and excited by the Toyota J-turn at speed of 17 m/s, causing both of the right wheels of the truck to lift.

rollover.

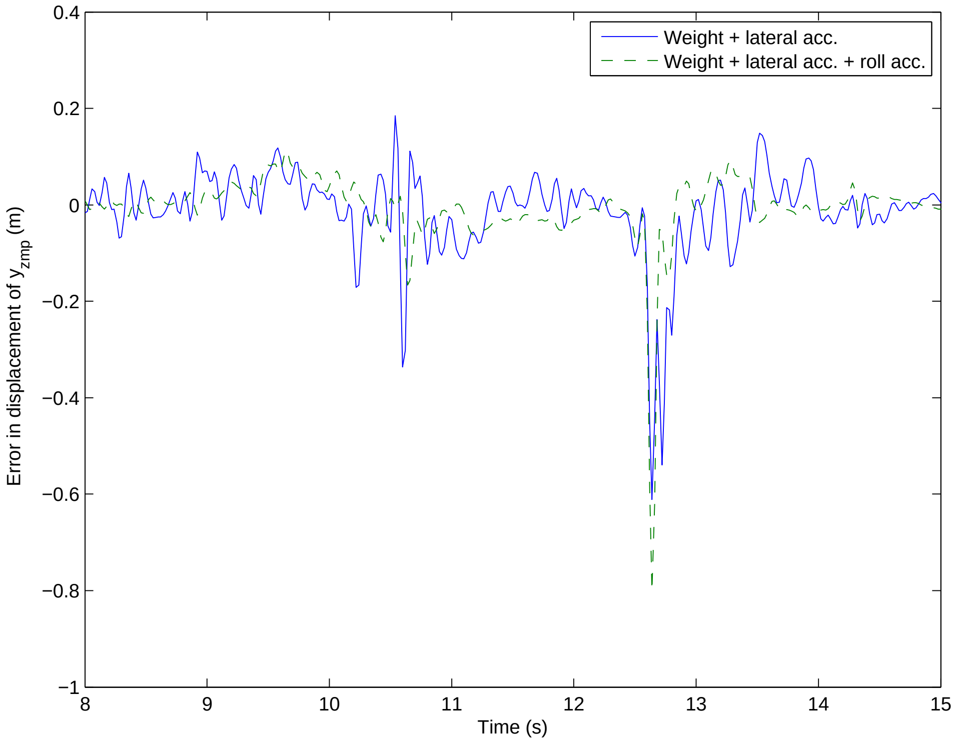

Figure 5.36: Errors between the full expression of y_{zmp} of the vehicle roll model and the combined terms in Figure 5.35.

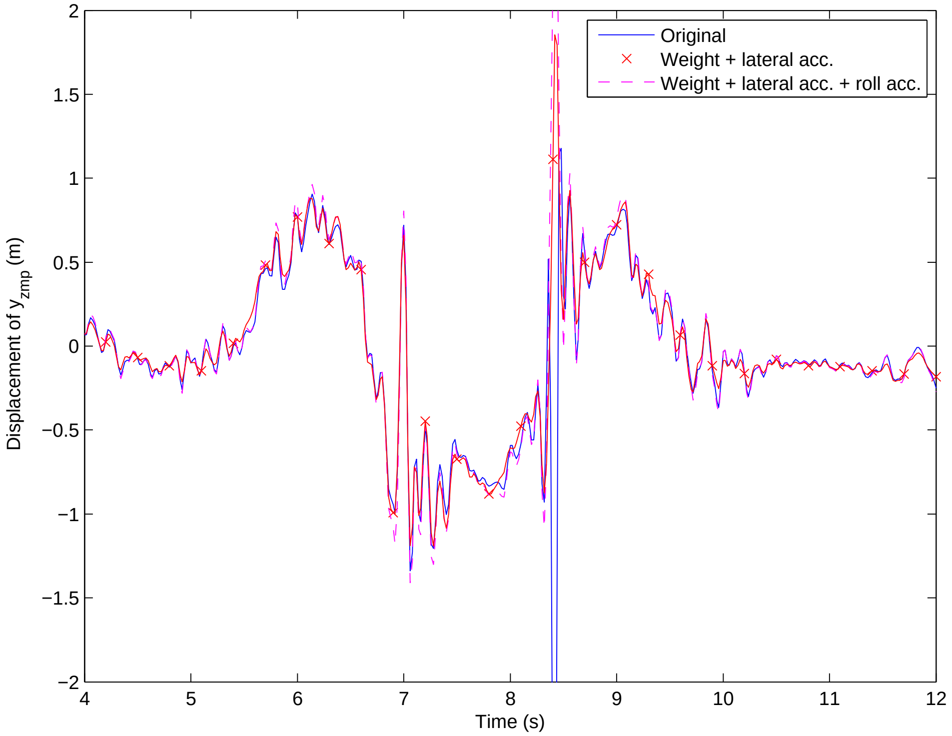

Figure 5.37: Contributions of combined terms in the y_{zmp} expression of the vehicle roll model obtained from the test in which the truck was driven on the banked road and excited by the Toyota J-turn at speed of 12 m/s, causing both of the right wheels of the truck to lift.

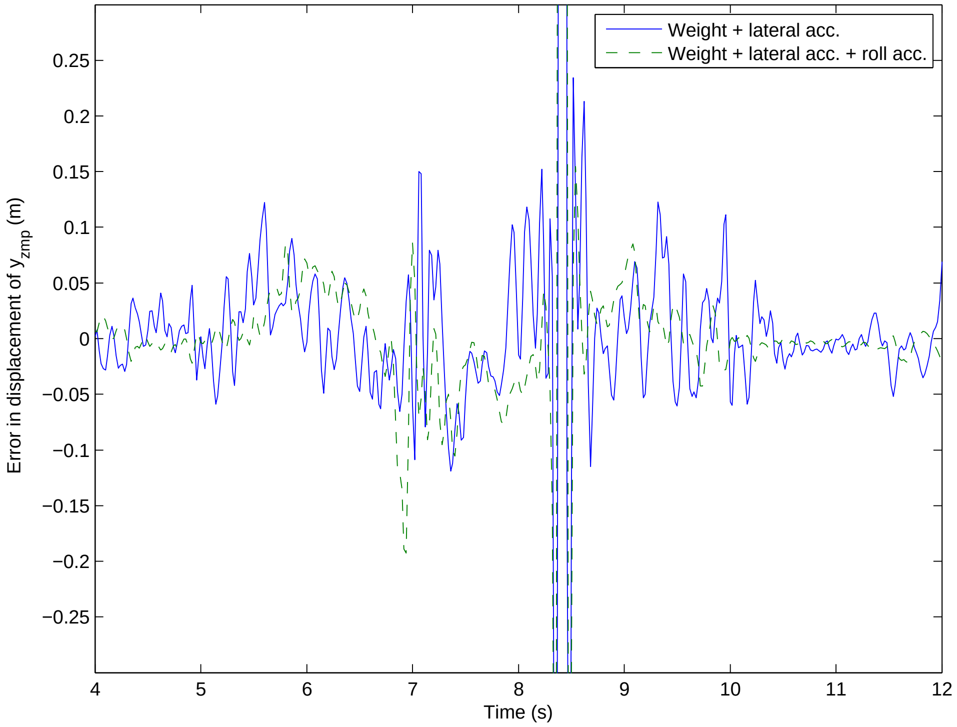

Figure 5.38: Errors between the full expression of y_{zmp} of the vehicle roll model and the combined terms in Figure 5.37.

Chapter 6

Conclusions and Future Work

This chapter summarizes the work in this thesis and suggests potential future work that may be pursued. The conclusions are discussed first and are followed by potential future work.

6.1 Conclusions

The concept of the Zero-Moment Point (ZMP) was introduced and applied to predict the onset of vehicle rollover for ground vehicles. The rigid vehicle model and the vehicle roll model were used to represent a vehicle in this work. The vehicle in the rigid vehicle model was assumed to behave as a rigid body, and the one in the vehicle roll model consists of two bodies, unsprung mass and sprung mass, moving relative to each other. Based on these models, the mathematical representations of the location the the ZMP were developed and used as vehicle rollover threat indices. Moreover, these rollover indices are one of the first algorithms that explicitly include the terrain features e.g. road bank, grade, etc. Additionally, it was shown that several of the existing rollover metrics are the special cases of the ZMP-based rollover indices, once appropriate assumptions are applied.

The effectiveness of the ZMP-based rollover indices was extensively validated, first with simulations and later through field experiments, under various scenarios and excitations. From both simulation and experimental results, it was observed that the ZMP is a valid indicator to measure the vehicle rollover propensity. The metrics derived from the rigid vehicle model and the vehicle roll model accurately predict imminent vehicle rollover. Further, the roll model, as expected, predicts the vehicle rollover more precisely than the rigid vehicle model, since the roll model incorporates more realistic assumptions. Additionally, the simulation results allow us to realize that the ZMP is an alternative way to represent load transfer.

Extensive analyses of the results were also performed. The analyses revealed many aspects of the rollover mechanisms. From the analysis, it is conclusive that the lateral acceleration plays the most influential role in predicting vehicle rollover. The vehicle's weight is the second most influential term. The weight becomes more dominant, once the roll angle of the vehicle or the inclination of the road becomes larger. From this, one can see that it is important to include the effect of terrain to predict wheel liftoff. With regard to the vehicle roll model, it is evident from the analysis that the dynamics of the sprung mass are far more significant than those of the unsprung mass. Hence, the influence of the unsprung mass is negligible. Further, it is shown that the expressions of y_{zmp} can be greatly simplified, especially for the vehicle roll model, with acceptable loss of accuracy.

6.2 Future Work

At the end of this thesis, we find many topics worth pursuing for the future research. These topics are listed in this section.

6.2.1 Causes of Oscillations in y_{zmp}

From the results in Figures 5.14 (large wheel lift) and 5.15 (sliding truck), one can notice the oscillations in the displacements of y_{zmp}. The frequency of oscillation in Figure 5.14 approximately is 1.8 Hz (period of 0.55 s); however, the oscillation in Figure 5.15 is not quite deterministic (varying from 1.8 Hz to 2.6 Hz). To determine a possible source of the oscillations, all the states associated with the y_{zmp} calculation from the results in Figure 5.14 are plotted in Figure 6.1. It is obvious from the plots of the vehicle states that none of the states have the distinct oscillations of this particular frequency.

To infer whether the equipment rack was causing the oscillation, an additional IMU was mounted to the rack on the truck to measure the lateral acceleration of the rack. Figures 6.2a and 6.2b respectively show the lateral accelerations of the unladen truck and the same truck with 448-kg extra weight while the truck

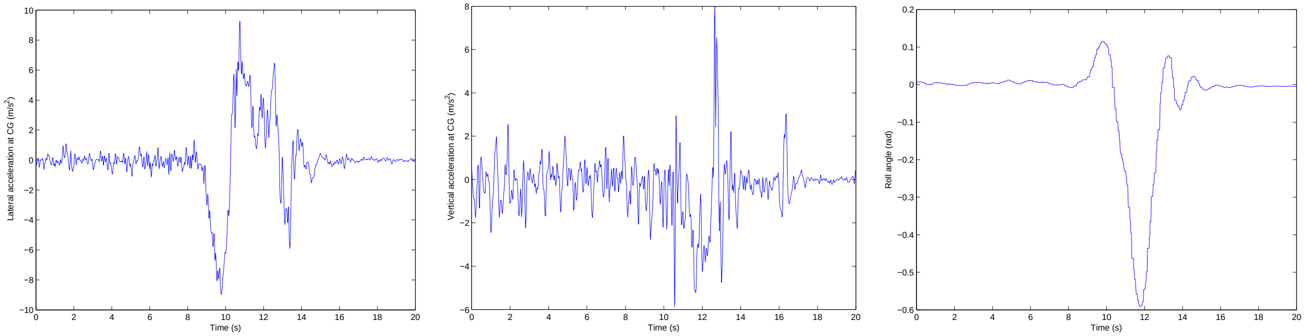

(a) Lateral acceleration at CG. (b) Vertical acceleration at CG. (c) Roll angle.

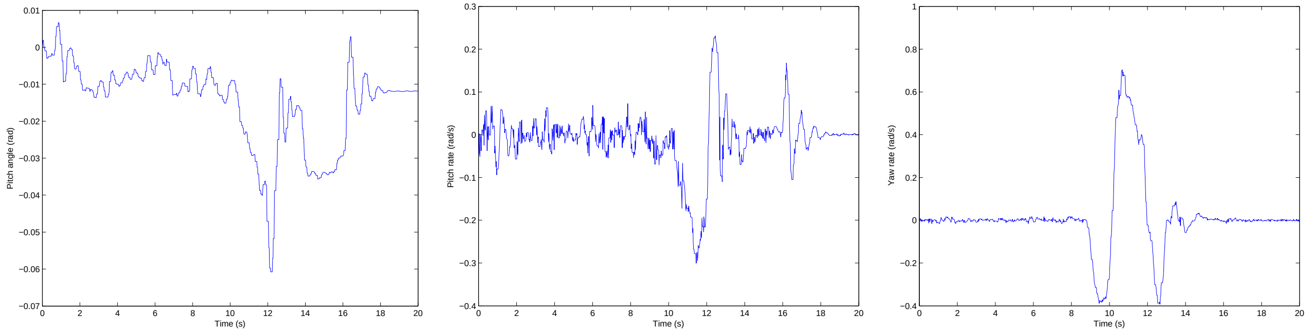

(d) Pitch angle. (e) Pitch rate. (f) Yaw rate.

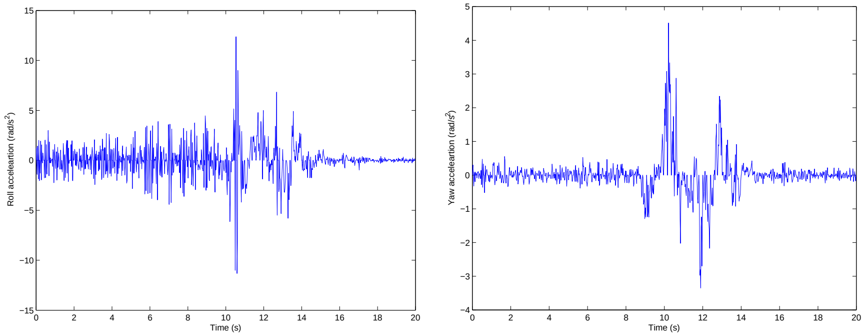

(g) Roll acceleration. (h) Yaw acceleration.

Figure 6.1: Vehicle states associated with the y_{zmp} calculation.

was being rocked laterally. From the figures, the roll natural frequencies were determined and are 1.3 Hz for the case of the unladen truck and 0.8 Hz for the case of the loaded truck. The natural frequencies of the roll mode are too low to be the cause of the oscillation of y_{zmp}. Further investigation may be required to identify the true causes of these oscillations.

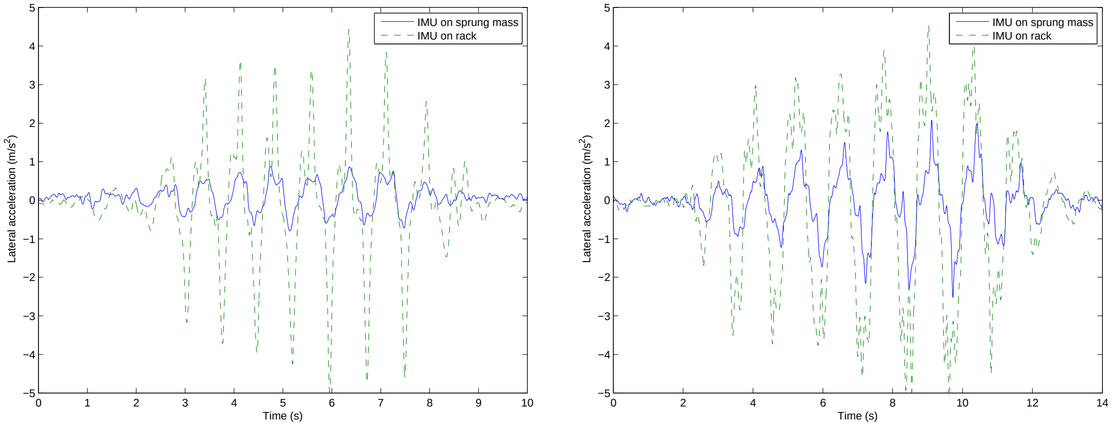

(a) Lateral accelerations from the oscillation test of the unladen truck.

(b) Lateral accelerations from the oscillation test of the truck with 448-kg extra weight.

Figure 6.2: Lateral accelerations from the oscillation tests.

6.2.2 Observer-Based Rollover Prediction Using the Zero-Moment Point Method

From the calculation of the location of the ZMP for the vehicle roll model, it is clear that there is a need to install an Inertia Measurement Unit (IMU) on the vehicle's unsprung mass to measure the states of the unsprung mass. This need may be eliminated by using an observer. The observer should be designed such that it can estimate the states of unsprung mass within an acceptable range of error. The estimated states will then be fed to the ZMP-based rollover algorithm to determine the location of the ZMP. Since most of the existing low-order vehicle models typically do not include the dynamics of unsprung mass and the influences of terrain, another challenge of this work will be to develop and verify a low-order linear vehicle dynamic model that considers these dynamics.

6.2.3 Model-Based Rollover Prediction Using the Zero-Moment Point Method

The idea of this section is to reduce the number of sensors required on a vehicle to estimate the location of the ZMP, particularly the displacement of y_{zmp}. Instead of relying on the inputs streaming in from the sensors, a low-order vehicle dynamic model will provide necessary vehicle states to the y_{zmp} calculation process. For this idea to work, a steering sensor is needed to measure the steering angle of the vehicle. The steering angle will be provided as an input to the vehicle dynamic model. The model will predict the vehicle states that will be used later to obtain the displacement of y_{zmp}. Similar challenges to the ones discussed in Section 6.2.2 are faced, such as coming up with a low-order linear vehicle dynamic model that describes the full dynamics of a vehicle.

6.2.4 Rollover Mitigation Using Model Predictive Control

This section proposes a method to implement Model-Predictive Control (MPC) [72, 73] to reduce the propensity of a vehicle to roll over. MPC, also known as Receding Horizon Control (RHC), is a control technique that explicitly uses a system model to obtain control signals by minimizing an objective function over a finite horizon. The objective function, which is usually a quadratic function, penalizes large inputs and large tracking errors. Moreover, MPC is a receding horizon strategy and thus provides an inherently iterative approach. At each time step, the first control signal of the sequence is implemented before the horizon is displaced towards the future [72]. The advantages of MPC over other techniques such as PID Control, State Feedback, etc. are that (1) this technique can easily deal with a Multiple-Input-Multiple-Output (MIMO) system, and (2) it can be extended to handle input and/or output constraints systematically during the controller design process [72].

The rollover-mitigation controller could be designed based on the MPC approach. Inputs to the vehicle will be calculated by minimizing an objective function. To calculate control signals for a vehicle that is on the threshold of rollover, the current steering input of the vehicle will be provided to the low-order vehicle dynamic model in order to generate a yaw-rate trajectory. The trajectory will be projected to a finite time period into the future, e.g. two seconds from the present. It is evident that the projected yaw-rate trajectory needs to account for the terrain encountered in the future. Consequently, it is necessary that (a) the terrain data be available, and (b) that the vehicle model employed utilizes the available terrain data. The projected yaw-rate trajectory will then be used as a reference signal for the controller. It is preferable to use the yaw rate as the reference, rather than the vehicle trajectory, since the the controller should not take away any authority to plan the future vehicle path from the driver.

Based on the analysis of experimental results discussed in Section 5.5, it is obvious that lateral acceleration plays a major role in rollover mechanisms. Thus, the best way to prevent the onset of rollover is to reduce the contribution from lateral acceleration. With this criteria in mind, the primary actuation mechanism that could be used to provide the necessary control input to prevent vehicle rollover is differential braking. Hence, the control input to the vehicle is the pressure applied to the brakes. In order to maintain roll stability of the vehicle during rollover recovery, a constraint that penalizes the displacement of y_{zmp} will also be included in the controller design. Once the constraint is added, the problem becomes a nonlinear-programming problem since the objective function is a quadratic function. To find a solution to this constrained optimization problem, a numerical technique such as Hidreth's Quadratic Programming Procedure [73] or Sequential Quadratic Programming (SQP) Procedure [74] may be used. The flow chart in Figure 6.3 summarizes the idea of rollover mitigation algorithm proposed in this section.

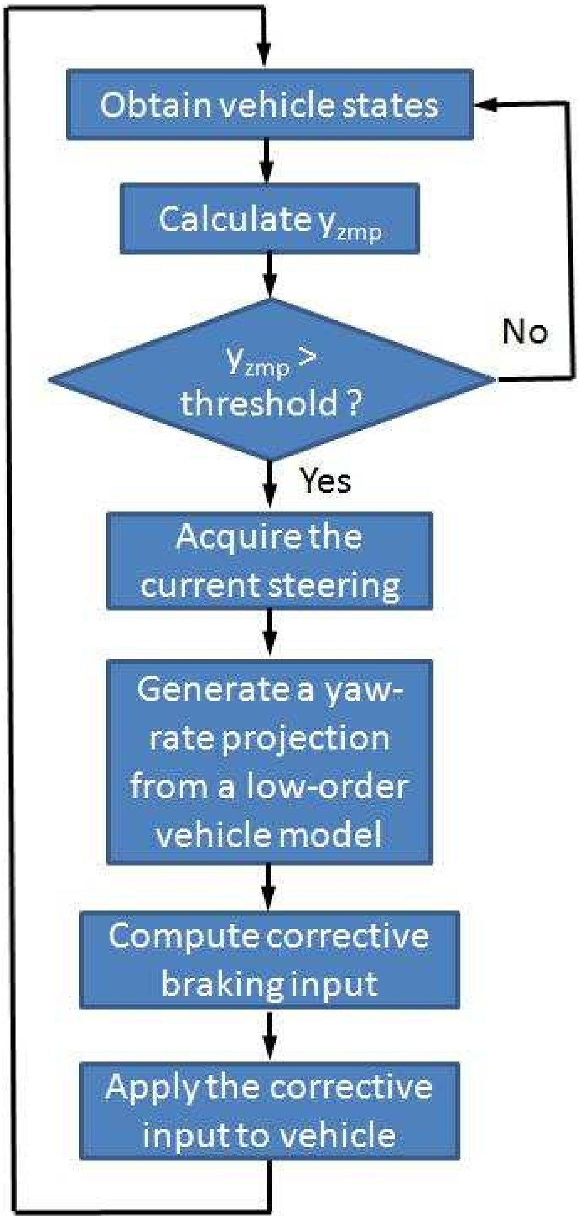

Figure 6.3: Flow chart summarizing rollover mitigation algorithm.

6.2.5 Terrain-Aware Rollover Prediction for Tractor-Trailer

According to a report from Center for National Truck and Bus Statistics at the University of Michigan Transportation Research Institute [75], there were 5,049 fatal commercial-truck incidents in 2007, claiming 5,248 lives. 3,399 of these incidents involves some type of tractor-trailer combination (e.g. a straight truck with a trailer, a tractor with a trailer, a tractor with two trailers, and other combinations). 12.6 percent of the tractor-trailer's accidents wers due to rollover. Although this percentage may seem low, the rollover incidents usually have a very high fatality rate [76]. Hence, it is crucial to enhance vehicle stability, especially roll stability of tractors-trailers.

The literature documents various rollover-prediction techniques applied to passenger cars that may equally well be applied to predict rollover of tractors-trailers. Thus, rollover metrics found in the literature can be classified similarly to the ones used in the passenger cars. The classification of the rollover threat indices is as follows: static or steady-state rollover metrics, rollover metrics based on thresholds of vehicle states or combinations of the vehicle states, rollover metrics based on forces acting on tires, and energy-based rollover metrics.

Examples of the static or steady-state rollover metrics are a metric proposed by Ervin [77] and Tilt-Table Ratio (TTR) [4]. Ervin [77] proposed that the static roll stability may be used for heavy vehicles. This roll stability is defined as a moment difference between a moment generated by lateral acceleration and a summation of moments generated by a vehicle suspension and vehicle weight.

States of a tractor-trailers, for instance, lateral acceleration, roll angle, roll rate, and a combination of these states, are widely implemented to detect wheel lift. Gillespie and Verma [8] proposed a dynamic rollover threshold based on the value of lateral acceleration that makes an outrigger to touch down. More examples of works that utilize lateral acceleration as a rollover metric are the works conducted by the research group led by Cebon at Cambridge University in England [13, 14, 15]. In addition to relying only on lateral acceleration as a rollover threat index, some combinations of vehicle states are often adopted. Polkovics *et al.* [16] used lateral acceleration threshold and difference in slip between two-sided wheels to detect rollover. Eisele and Peng [17] introduced a rollover index that is a combination of roll angle, roll rate, and lateral acceleration.

Extended from the use in passenger cars, Time-To-Rollover (TTR) [19, 22], which was proposed by Chen and Peng and is a model-based technique, has also been applied to tractors-trailers. In the work of Gaspar *et al.* [26], an observer was designed to monitor normal loads on wheels to predict wheel lift. The last type of the rollover metric is based on energy principle. Dahlberg [34] presented the idea of dynamic rollover energy margin in which the potential energy of suspensions is included. To define an unstable equilibrium point in a multi-body system, Dahlberg identified a saddle point that gave the lowest non-zero value of a potential-energy function.

As seen from the literature, all previous works ignore the effects of terrain while predicting vehicle rollover. Consequently, the concept of the Zero-Moment Point (ZMP) may be extended and used to predict wheel lift of a tractor-trailer, especially in the presence of terrain. Another advantage of the ZMP method is that, by its nature, the technique can easily deal with a multi-body system like the tractor-trailer.

Appendix A

Physical Parameters of Test Truck under Different Loading Conditions

This appendix contains the physical parameters of the test trucks under different loading conditions. The definitions of the nomenclature are indicated in Tables 2.1 and 2.2. It is also important to note that these parameters belong to the truck with the outriggers mounted on the front and rear bumpers.

Table A.1: Parameters of the test truck loaded with no extra weight.

Symbol	**Value**	**Unit**	**Symbol**	**Value**	**Unit**
m	2345	kg	m_u	299	kg
m_s	2045	kg	a	1.403	m
b	1.951	m	c	0.094	m
d	0.652	m	T	1.615	m
h	0.805	m	h_u	0.352	m
h_s	0.872	m	h_r	0.5	m
I_{xx}	932	kg·m^2	I_{yy}	6008	kg·m^2
I_{zz}	6042	kg·m^2	I_{xz}	0	kg·m^2
I_{yz}	0	kg·m^2	I_{xx_u}	145	kg·m^2
I_{yy_u}	802	kg·m^2	I_{zz_u}	947	kg·m^2
I_{xz_u}	0	kg·m^2	I_{yz_u}	0	kg·m^2
I_{xx_s}	716	kg·m^2	I_{yy_s}	5065	kg·m^2
I_{zz_s}	4955	kg·m^2	I_{xz_s}	0	kg·m^2
I_{yz_s}	0	kg·m^2	g	9.81	m/s^2

Table A.2: Parameters of the test truck loaded with 448-kg extra weight (16 water containers).

Symbol	**Value**	**Unit**	**Symbol**	**Value**	**Unit**
m	3021	kg	m_u	299	kg
m_s	2722	kg	a	1.724	m
b	1.630	m	c	0.111	m
d	0.321	m	T	1.615	m
h	1.123	m	h_u	0.352	m
h_s	1.174	m	h_r	0.5	m
I_{xx}	1648	kg·m^2	I_{yy}	6593	kg·m^2
I_{zz}	6671	kg·m^2	I_{xz}	0	kg·m^2
I_{yz}	0	kg·m^2	I_{xx_u}	145	kg·m^2
I_{yy_u}	802	kg·m^2	I_{zz_u}	947	kg·m^2
I_{xz_u}	0	kg·m^2	I_{yz_u}	0	kg·m^2
I_{xx_s}	1339	kg·m^2	I_{yy_s}	5683	kg·m^2
I_{zz_s}	5616	kg·m^2	I_{xz_s}	0	kg·m^2
I_{yz_s}	0	kg·m^2	g	9.81	m/s^2

Table A.3: Parameters of the test truck loaded with 560-kg extra weight (20 water containers).

Symbol	**Value**	**Unit**	**Symbol**	**Value**	**Unit**
m	3133	kg	m_u	299	kg
m_s	2834	kg	a	1.779	m
b	1.575	m	c	0.089	m
d	0.265	m	T	1.615	m
h	1.158	m	h_u	0.352	m
h_s	1.211	m	h_r	0.5	m
I_{xx}	1784	kg·m^2	I_{yy}	6892	kg·m^2
I_{zz}	6981	kg·m^2	I_{xz}	0	kg·m^2
I_{yz}	0	kg·m^2	I_{xx_u}	145	kg·m^2
I_{yy_u}	802	kg·m^2	I_{zz_u}	947	kg·m^2
I_{xz_u}	0	kg·m^2	I_{yz_u}	0	kg·m^2
I_{xx_s}	1457	kg·m^2	I_{yy_s}	6007	kg·m^2
I_{zz_s}	5951	kg·m^2	I_{xz_s}	0	kg·m^2
I_{yz_s}	0	kg·m^2	g	9.81	m/s^2

Table A.4: Parameters of the test truck loaded with 784-kg extra weight (28 water containers).

Symbol	**Value**	**Unit**	**Symbol**	**Value**	**Unit**
m	3321	kg	m_u	299	kg
m_s	3022	kg	a	1.894	m
b	1.460	m	c	0.050	m
d	0.147	m	T	1.615	m
h	1.220	m	h_u	0.352	m
h_s	1.265	m	h_r	0.5	m
I_{xx}	2030	kg·m^2	I_{yy}	7751	kg·m^2
I_{zz}	7862	kg·m^2	I_{xz}	0	kg·m^2
I_{yz}	0	kg·m^2	I_{xx_u}	145	kg·m^2
I_{yy_u}	802	kg·m^2	I_{zz_u}	947	kg·m^2
I_{xz_u}	0	kg·m^2	I_{yz_u}	0	kg·m^2
I_{xx_s}	1665	kg·m^2	I_{yy_s}	6913	kg·m^2
I_{zz_s}	6879	kg·m^2	I_{xz_s}	0	kg·m^2
I_{yz_s}	0	kg·m^2	g	9.81	m/s^2

Appendix B

Additional Experimental Results

This appendix presents additional experimental results. The results are from different testing conditions. Descriptions of the conditions are provided below the results. In the plots of the results, the percentage of suspension travel is in the upper sections of the plots, and the displacements of y_{zmp} estimated from both the rigid vehicle model and the vehicle roll model are in the lower sections. The displacement of y_{zmp} computed from the rigid vehicle model is denoted by a solid magenta line, and the one from the vehicle roll model is represented by the dash blue line. In the plots, it is very hard to distinguish theses two lines, since the displacement of y_{zmp} from the vehicle roll model is almost on the top of the one from the rigid vehicle model. The track width is the distance between the red dotted lines. Wheel-liftoff regions are highlighted with cyan if only one wheel had lifted and with yellow if two wheels had lifted. The results obtained from the tests conducted on the flat road are given first and then followed by those on the banked road.

B.1 Experimental Results on Flat Road

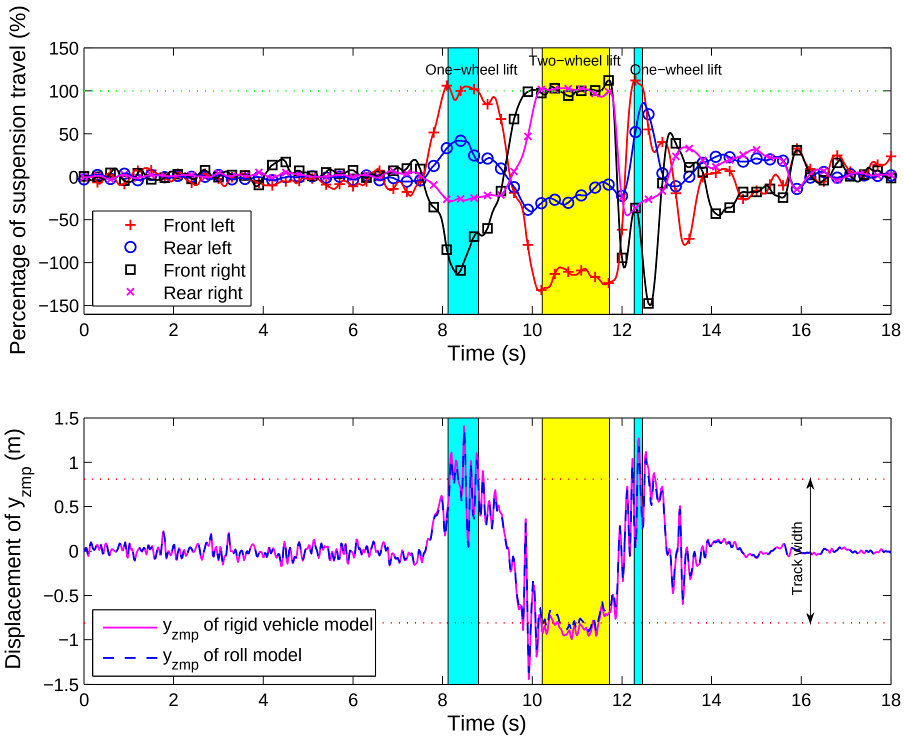

Figure B.1: Percentage of suspension travel and displacements of y_{zmp} obtained from the test in which the truck was driven on the flat road and excited by the Toyota J-turn at speed of 10 m/s, causing both of the right wheels of the truck to lift. The vehicle parameters used to determine the displacements of y_{zmp} are in Table A.4.

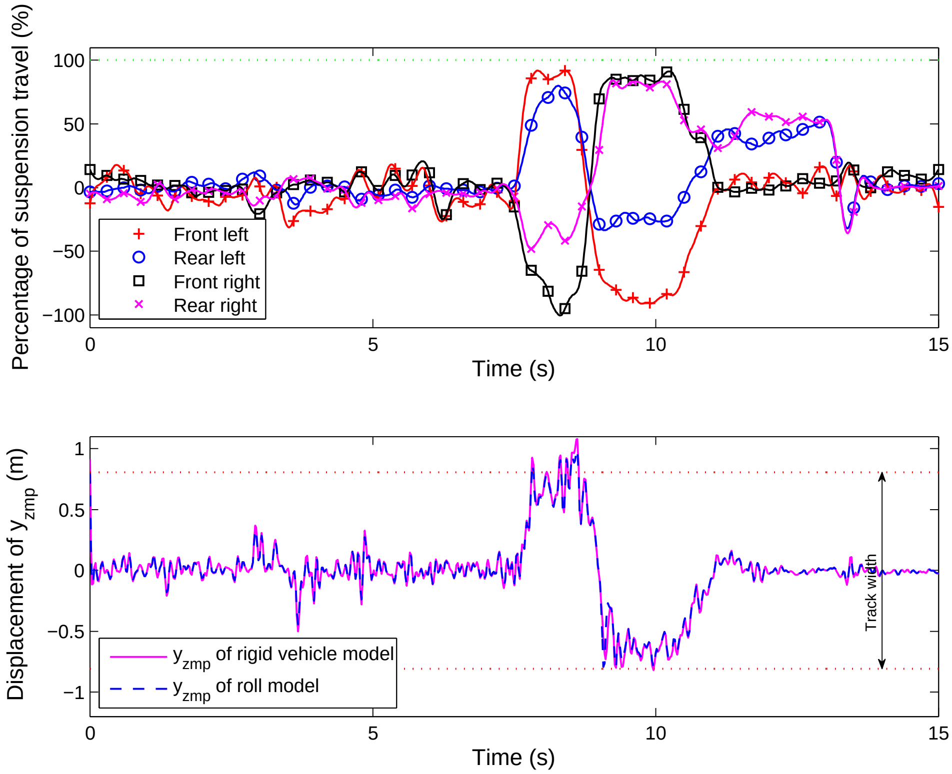

Figure B.2: Percentage of suspension travel and displacements of y_{zmp} obtained from the test in which the truck was driven on the flat road and excited by the Toyota J-turn at speed of 16 m/s, causing the truck to skid with no wheel lift. The vehicle parameters used to determine the displacements of y_{zmp} are in Table A.1.

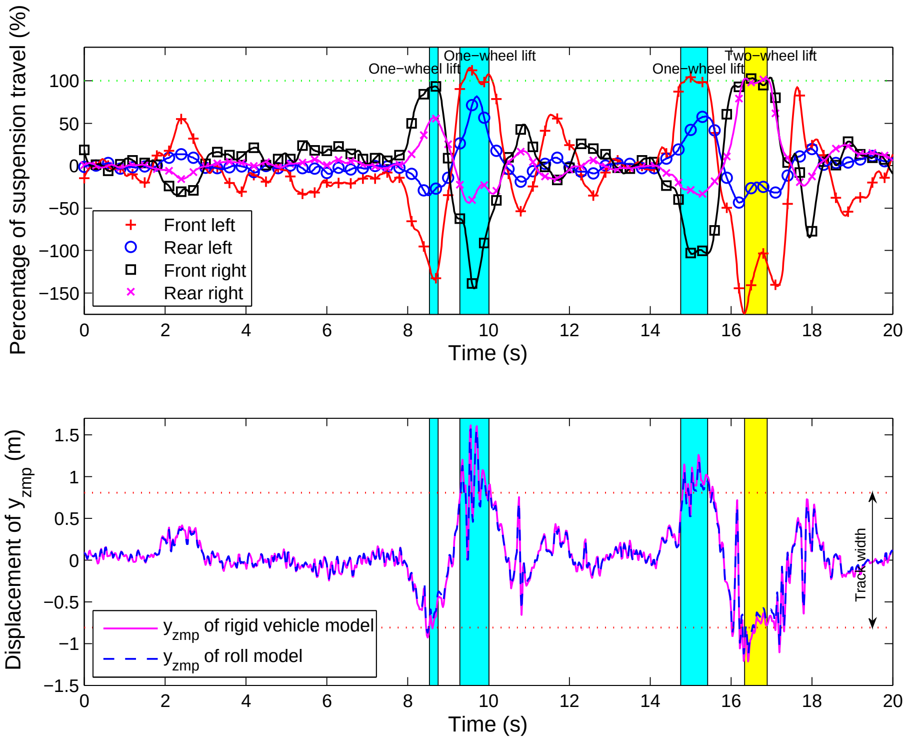

Figure B.3: Percentage of suspension travel and displacements of y_{zmp} obtained from the test in which the truck was driven on the flat road and excited by the double-lane-change maneuver at speed of 10 m/s, causing both of the right wheels of the truck to lift. The vehicle parameters used to determine the displacements of y_{zmp} are in Table A.4.

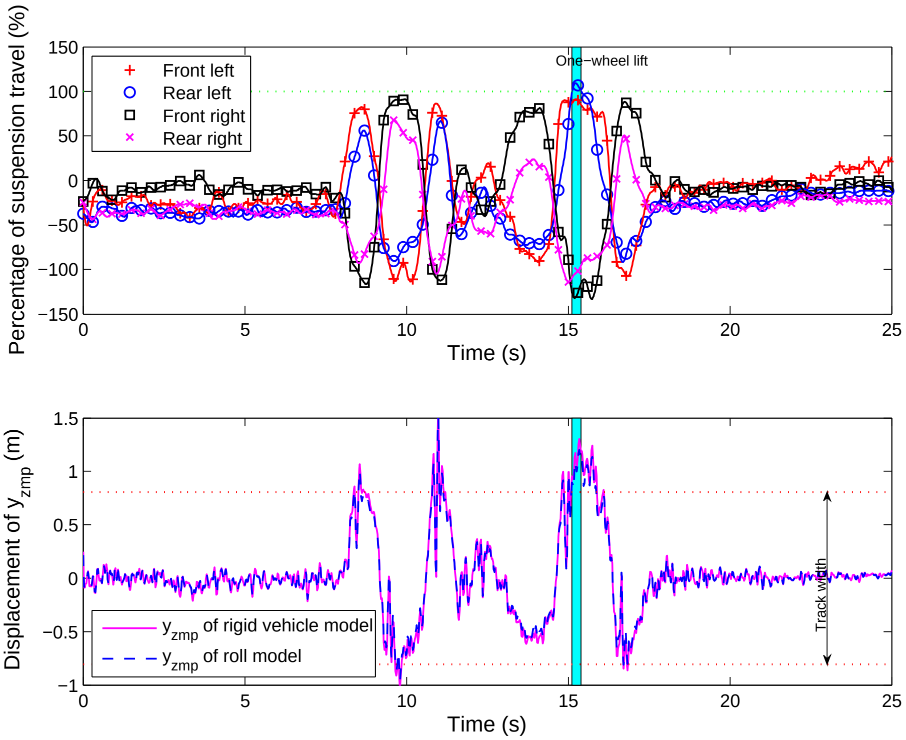

Figure B.4: Percentage of suspension travel and displacements of y_{zmp} obtained from the test in which the truck was driven on the flat road and excited by the double-lane-change maneuver at speed of 13 m/s. In the test, the truck had no wheel lift on the first turn, but the rear left wheel lifted off the ground on the second turn. The vehicle parameters used to determine the displacements of y_{zmp} are in Table A.2.

B.2 Experimental Results on Banked Road

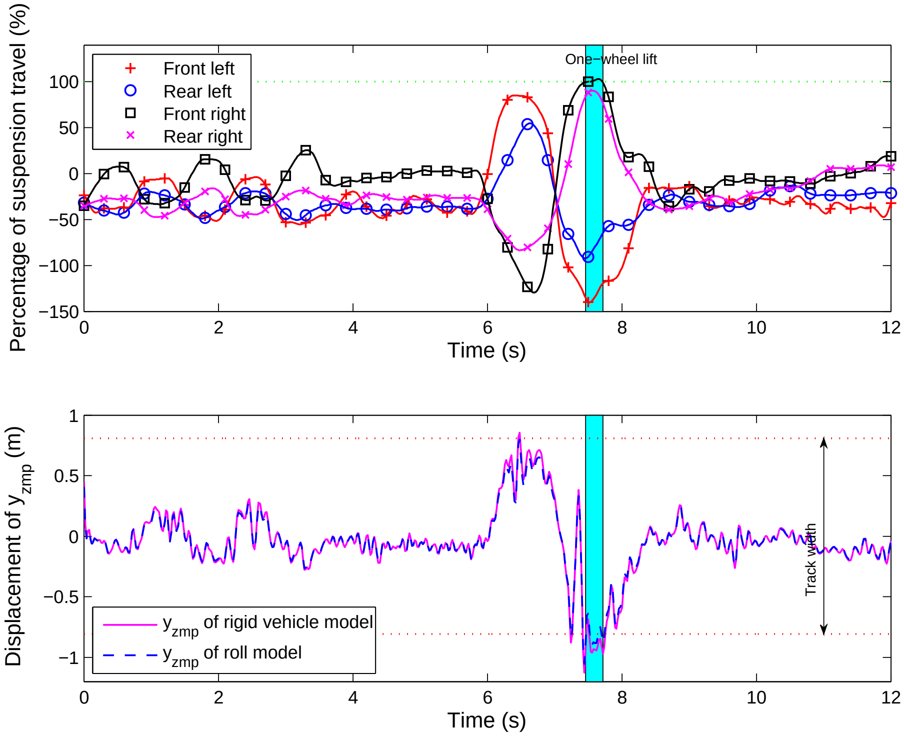

Figure B.5: Percentage of suspension travel and displacements of y_{zmp} obtained from the test in which the truck was driven on the banked road and excited by the Toyota J-turn at speed of 10 m/s, causing the front right wheel of the truck to lift. The vehicle parameters used to determine the displacements of y_{zmp} are in Table A.2.

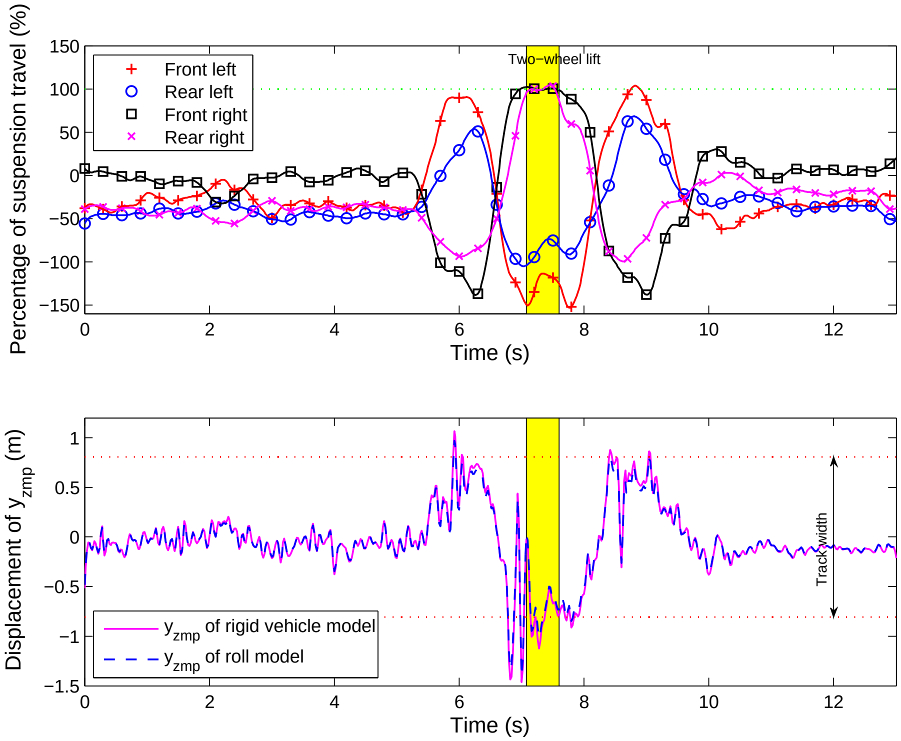

Figure B.6: Percentage of suspension travel and displacements of y_{zmp} obtained from the test in which the truck was driven on the banked road and excited by the Toyota J-turn at speed of 10 m/s, causing both of the right wheels of the truck to lift. The vehicle parameters used to determine the displacements of y_{zmp} are in Table A.3.

Bibliography

[1] Heron, M., D. L. Hoyert, S. L. Murphy, J. Xu, K. D. Kochanek, and B. Tejada-Vera "Deaths: Final Data for 2006," *National Vital Statistics Reports*, **57**(14). 2

[2] NHTSA's National Center for Statistics and Analysis, "Traffic Safety Facts: 2007 Data," DOT HS 810 993. 2

[3] Wilson, R. A. and R. R. Gannon (1972) "Rollover Testing," *SAE Tech. Paper Series*, (720495). 2

[4] Chrstos, J. P. and D. A. Guenther (1992) "The Measurement of Static Rollover Metrics," *SAE Tech. Paper Series*, (920582). 3, 4, 5, 48, 102, 151

[5] Transportation Research Board (2002) *The National Highway Traffic and Safety Administration's Rating System for Rollover Resistance*, National Academy Press, Washington, D.C. 3, 5, 10, 14, 48, 102

[6] Bickerstaff, D. J. (1976) "The Handling Properties of Light Trucks," *SAE Tech. Paper Series*, (760710). 3, 6, 50

[7] Dukkipati, R. V., J. Pang, M. S. Qatu, G. Sheng, and Z. Shuguang (2008) *Road Vehicle Dynamics*, Society of Automotive Engineers, Inc., Warrendale, PA. 3, 8, 11, 16, 52, 54, 102

[8] Gillespie, T. D. and M. K. Verma (1978) "Analysis of the Rollover Dynamics of Double-Bottom Tankers," *SAE Tech. Paper Series*, (781065). 6, 12, 50, 151

[9] Wielenga, T. J. (1999) "A Method for Reducing On-Road Rollovers–Anti-Rollover Braking," *SAE Tech. Paper Series*, (1999-01-0123). 12, 18

[10] Wielenga, T. J. and M. A. Chace (2000) "A Study in Rollover Prevention Using Anti-Rollover Braking," *SAE Tech. Paper Series*, (2000-01-1642). 12, 18

[11] Carlson, C. R. and J. C. Gerdes (2003) "Optimal Rollover Prevention with Steer By Wire and Differential Braking," in *Proc. 2003 ASME IMECE*, vol. 72 DSC, Washington, DC, pp. 345–354. 12, 18, 64

[12] Yoon, J., D. Kim, and K. Yi (2007) "Design of a Rollover Index-Based Vehicle Stability Control Scheme," *Veh. Syst. Dyn.*, **45**(5), pp. 459–475. 12, 19

[13] Lin, R. C., D. Cebon, and D. J. Cole (1996) "Active Roll Control of Articulated Vehicles," *Veh. Syst. Dyn.*, **26**(1), pp. 17–46. 12, 19, 152

[14] Sampson, D. J. M. and D. Cebon (2003) "Achievable Roll Stability of Heavy Road Vehicles," *Proc. Instn. Mech. Engrs., Part D: J. Automobile Engineering*, **217**(4), pp. 269–287. 12, 19, 152

[15] Miege, A. J. P. and D. Cebon (2005) "Optimal Roll Control of an Articulated Vehicle: Theory and Model Validation," *Veh. Syst. Dyn.*, **43**(12), pp. 867–893. 12, 19, 152

[16] Polkovics, L., A. Semsey, and E. Gerum (1999) "Roll-Over Prevention System for Commercial Vehicles–Additional Sensorless Function of the Electronic Brake System," *Veh. Syst. Dyn.*, **32**(4), pp. 285–297. 12, 19, 152

[17] Eisele, D. D. and H. Peng (2000) "Vehicle Dynamics Control with Rollover Prevention for Articulated Heavy Trucks," in *Proc. 5th Int. Symp. Advanced Vehicle Control: AVEC2000*, Ann Arbor, MI. 12, 19, 152

[18] Chen, B.-C. and H. Peng (1999) "A Real-Time Rollover Threat Index for Sport Utility Vehicle," in *Proc. Amer. Control Conf.*, vol. 2, San Diego, CA, pp. 1233–1237. 13

[19] ——— (1999) "Rollover Warning of Articulated Vehicles Based on a Time-To-Rollover Metric," in *Proc. 1999 ASME IMECE*, vol. 67 DSC, Knoxville, TN, pp. 247–254. 13, 152

[20] ——— (2000) "Rollover Prevention for Sport Utility Vehicles with Human-in-the-Loop Evaluations," in *Proc. 5th Int. Symp. Advanced Vehicle Control: AVEC2000*, Ann Arbor, MI. 13, 18

[21] ——— (2001) "Differential-Braking-Based Rollover Prevention for Sport Utility Vehicle with Human-in-the-Loop," *Veh. Syst. Dyn.*, **36**(4-5), pp. 359–389. 13, 18, 96

[22] ——— (2005) "Rollover Warning of Articulated Vehicles Based on a Time-To-Rollover Metric," *J. Dynam. Syst., Meas., and Contr. (Tran. ASME)*, **127**, pp. 406–414. 13, 152

[23] Ervin, R. D. and Y. Guy (1986) *The Influence of Weights and Dimensions on the Stability and Control of Heavy-Duty Trucks in Canada Volume I*, *Tech. Rep. UMTRI-86-35/I*, The University of Michigan Transportation Research Institute, Ann Arbor, MI. 13, 97

[24] Peters, S. C. and K. Iagnemma (2008) "Stability Measurement of High-Speed Vehicles," *Veh. Syst. Dyn.*, **47**(6), pp. 701–720. 13, 14

[25] Odenthal, D., T. Bünte, and J. Ackermann (1999) "Nonlinear Steering and Braking Control for Vehicle Rollover Avoidance," in *Proc. European Control Conf.*, Karlsruhe, Germany. 13

[26] Gaspar, P., Z. Szabo, and J. Bokor (2000) "Prediction Based Combined Control to Prevent the Rollover of Heavy Vehicles," in *Proc. 13th Mediterranean Conf. on Control and Automation*, Limassol, Cyprus, pp. 575–580. 14, 19, 152

[27] Cameron, J. T. (2005) *Vehicle Dynamic Modeling for the Prediction and Prevention of Vehicle Rollover*, Master's thesis, The Pennsylvania State University. 14, 19

[28] Jones, I. S. (1973) *Road Accident Studies with Particular Reference to the Handling and Stability Characteristics of Cars*, Ph.D. thesis, University College London. 14

[29] Lund, Y. I. and J. E. Bernard (1995) "Analysis of Simple Rollover Metrics," *SAE Tech. Paper Series*, (950306). 14

[30] Meriam, J. L. and L. G. Kraige (1997) *Engineering Mechanics: Dynamics*, fourth ed., John Wiley & Sons, Inc., New York, NY. 14, 26, 77, 79

[31] Nalecz, A. G. (1989) "Influence of Vehicle and Roadway Factors on the Dynamics of Tripped Rollover," *Int. J. Vehicle Design*, **10**(3), pp. 321–346. 16

[32] ——— (1993) "An Investigation into Dynamic Measures of Vehicle Rollover Propensity," *SAE Tech. Paper Series*, (930831). 16

[33] Choi, S. B. (2008) "Prectical Vehicle Rollover Avoidance Control Using Energy Method," *Veh. Syst. Dyn.*, **46**(4), pp. 323–337. 17

[34] Dahlberg, E. (2001) *Commercial Vehicle Stability Focusing on Rollover*, Ph.D. thesis, Royal Institute of Technology. 17, 152

[35] NHTSA's National Center for Statistics and Analysis, "Traffic Safety Facts 2005: A Compilation of Motor Vehicle Crash Data from the Fatality Analysis Reporting System and the General Estimates System," DOT HS 810 631. 17

[36] Douglas, J. W. and R. R. Modlin (1977) "The Truck Stabilizer: A Means of Preventing Rollover During Braking and Handling Test Situations," *SAE Tech. Paper Series*, (770892). 18

[37] Konik, D., R. Bartz, F. Bärnthol, H. Bruns, and M. Wimmer (2000) "Dynamic Drive–The New Active Roll Stabilization System from the BMW Group–System Description and Functional Improvements," in *Proc. 5th Int. Symp. Advanced Vehicle Control: AVEC2000*, Ann Arbor, MI. 18

[38] Woodrooffe, J. H. F., J. R. Billing, and R. L. Nisonger (1983) "Improved Stability and Handing of Truck Combinations with the Double Drawbar Dolly," *SAE Tech. Paper Series*, (831162). 19

[39] Rakheja, S. and A. Piché (1990) "Development of Directional Stability Criteria for an Early Warning Safety Device," *SAE Tech. Paper Series*, (902265). 19

[40] Dunwoody, A. B. and S. Froese (1993) "Active Roll Control of a Semi-Trailer," *SAE Tech. Paper Series*, (933045). 19

[41] Miege, A. J. P. and D. Cebon (2002) "Design and Implementation of an Active Roll Control System for Heavy Vehicles," in *Proc. 6th Int. Symp. Advanced Vehicle Control: AVEC2002*, Hiroshima, Japan. 19

[42] Vukobratović, M. and D. Juričić (1968) "Contribution to the Synthesis of Biped Gait," in *Proc. IFAC Symp. Technical and Biological Problem on Control*, Erevan, USSR. 22

[43] Vukobratović, M. and B. Borovic (1975) "Dynamic Control of Unstable Locomotion Robots," *Mathematical Biosciences*, **24**, pp. 129–157. 22

[44] Vukobratović, M., B. Borovic, D. Surla, and D. Stolić (1990) *Biped Locomotion–Dynamics, Stability, Control, and Application*, Spring-Verlag, Berlin, Germany. 22

[45] Vukobratović, M. and B. Borovic (2004) "Zero-Moment Point–Thirty Five Years of Its Life," *Int. J. Humanoid Robotics*, **1**(1), pp. 157–173. 22

[46] Hirai, K., M. Hirose, Y. Haikawa, and T. Takenaka (1998) "The Development of Honda Humanoid Robot," in *Proc. IEEE Int. Conf. on Robotics and Automation*, vol. 2, Leuven, Belgium, pp. 1321–1326. 22

[47] Sugano, S., Q. Huang, and I. Kato (1993) "Stability Criteria in Controlling Mobile Robotic Systems," in *Proc. IEEE Int. Conf. on Intelligent Robots and Systems*, Tokyo, Japan, pp. 832–838. 22

[48] Huang, Q., S. Sugano, and I. Kato (1994) "Stability Control for a Mobile Manipulator Using a Potential Method," in *Proc. IEEE Int. Conf. on Intelligent Robots and Systems*, vol. 2, Munich, Germany, pp. 839–846. 22

[49] Huang, Q. and S. Sugano (1995) "Manipulator Motion Planning for Stabilizing a Mobile-Manipulator," in *Proc. IEEE Int. Conf. on Intelligent Robots and Systems*, vol. 3, Pittsburgh, PA, pp. 467–472. 22

[50] Furuno, S., M. Yamamoto, and A. Mohri (2003) "Trajectory Planning of Mobile Manipulator with Stability Considerations," in *Proc. IEEE Int. Conf. on Robotics and Automation*, vol. 3, Taipei, Taiwan, pp. 3403–3408. 22

[51] Kim, J. and W. K. Chung (2006) "Real-Time Zero Moment Point Compensation Method Using Null Motion for Mobile Manipulators," *Advanced Robotics*, **20**(5), pp. 581–593. 22, 26

[52] Sardain, P. and G. Bessonnet (2004) "Forces Acting on a Biped Robot. Center of Pressure–Zero Moment Point," *IEEE Trans. Syst., Man, Cybern. A*, **34**(5), pp. 630–637. 22, 23

[53] Baruh, H. (1999) *Analytical Dynamics*, McGraw-Hill Book Co., Singapore. 26

[54] Dasgupta, A. and Y. Nakamura (1999) "Making Feasible Walking Motion of Humanoid Robots from Human Motion Capture Data," in *Proc. IEEE Int. Conf. on Robotics and Automation*, vol. 2, Detroit, MI, pp. 1044–1049. 26

[55] Milliken, W. F. and D. L. Milliken (1995) *Race Car Vehicle Dynamics*, Society of Automotive Engineers, Inc., Warrendale, PA. 29

[56] (1976) *Vehicle Dynamics Terminology–SAE J670e*, *Tech. rep.*, Society of Automotive Engineers, Inc., Warrendale, PA. 32

[57] Vemulapalli, P. K. and S. N. Brennan (2009) "Design and Testing of a Terrain Mapping System for Median Slope Measurement," in *Proc. 88th Annual Meeting of the Transportation Research Board*, Washington, D. C. 44

[58] Anton, H. (2005) *Elementary Linear Algebra*, ninth ed., John Wiley & Sons, Inc., Hoboken, NJ. 47

[59] Mammar, S., V. B. Baghdassarian, and L. Nouveliere (1999) "Speed Scheduled Lateral Vehicle Control," in *Proc. IEEE Conf. on Intelligent Transportation Systems*, pp. 80–85. 64

[60] Takano, S., M. Nagai, T. Taniguchi, and T. Hatano (2003) “Study on Vehicle Dynamics for Improving Roll Stability,” *JSAE Review*, **24**(2), pp. 149–156. 64

[61] Kim, H.-J. and Y.-P. Park (2004) “Investigation of Robust Roll Motion Control Considering Varying Speed and Actuator Dynamics,” *Mechatronics*, **14**(1), pp. 35–54. 64

[62] (1992) *Road Vehicles with Two Axles–Determination of Center of Gravity–ISO 10392*, *Tech. rep.*, International Organization for Standardization, Genève, Switzerland. 76, 77

[63] Heydinger, G. J. (1990) *Improved Simulation and Validation of Road Vehicle Handling Dynamics*, Ph.D. thesis, The Ohio State University. 76, 78

[64] Meriam, J. L. and L. G. Kraige (1998) *Engineering Mechanics: Statics*, fourth ed., John Wiley & Sons, Inc., New York, NY. 77

[65] Riede, Jr., P. M., R. L. Leffert, and W. A. Cobb (1984) “Typical Vehicle Parameters for Dynamics Studies Revised For the 1980s,” *SAE Tech. Paper Series*, (840561). 78

[66] Allen, R. W., H. T. Szostak, D. H. Klyde, T. J. Rosenthal, and K. J. Owens, “Vehicle Dynamic Stability and Rollover,” DOT HS 807 956. 78

[67] Wellstead, P. E. (2003) *Frequency Response Analysis*, *Tech. Rep. 10*, Solartron Instruments, Hampshire, UK. 91

[68] Laubwald, E. and M. Readman *Frequency Response Analysis*, *Tech. rep.*, Control-Ststems-Principles.co.uk, Cheshire, UK. 91

[69] Salaani, M. K., D. A. Guenther, and G. J. Heydinger (1999) “Vehicle Dynamics Modeling for the National Advanced Driving Simulator of a 1997 Jeep Cherokee,” *SAE Tech. Paper Series*, (1999-01-0121). 96

[70] National Highway Traffic Safety Administration (2001) “Consumer Information Regulations; Federal Motor Vehicle Safety Standards; Rollover Resistance,” *Federal Register*, **66**(128), pp. 35179–35193. 97

[71] Hamby, D. M. (1994) “A Review of Techniques for Parameter Sensitivity Analysis of Environmental Models,” *Environmental Monotoring and Assessment*, **32**(2), pp. 135–154. 120

[72] Camacho, E. F. and C. Birdons *Model Predictive Control*, second ed., Springer-Verlag London Limited. 148

[73] Wang, L. *Model Predictive Control System Design and Implementation Using MATLAB*, Springer-Verlag London Limited. 148, 149

[74] Rao, S. (2003) *Engineering Optimization: Theory and Practice*, third ed., New Age International (P) Limited, New Delhi, India. 149

[75] Jarossi, L., A. Matteson, and J. Woodrooffe (2010) *Trucks Involved in Fatal Accidents Factbook 2007, Tech. Rep. UMTRI-2010-4*, Center for National Truck and Bus Statistics, Ann Arbor, MI. 150

[76] Winkler, C. (200) “Rollover of Heavy Commercial Vehicles,” *UMTRI Research Review*, **31**(4), pp. 1–17. 151

[77] Ervin, R. D. (1983) “The Influence of Size and Weight Variables on the Roll Stability of Heavy Duty Trucks,” *SAE Tech. Paper Series*, (831163). 151

Vita

Sittikorn Lapapong

Education:
Ph.D. in Mechanical Engineering, *2010*
The Pennsylvania State University, University Park, PA, USA

Education:
M.S. in Mechanical Engineering, *2007*
The Pennsylvania State University, University Park, PA, USA

B.Eng. in Mechanical Engineering (First Class Honours), *2002*
King Mongkut's University of Technology Thonburi (KMUTT), Bangkok, Thailand

Professional Experience:

November 2002 -November 2004	Research Assistant, Department of Mechanical Engineering and Institute of FIeld roBOtics, King Mongkut's University of Technology Thonburi, Bangkok, Thailand
March 2001 -May 2001	Internship, Technical Department, Royal Chitralada Project, Bangkok, Thailand

Honors and Awards:
The Royal Thai Government Scholarships, *2004-2010*, Ministry of Science and Technology, The Royal Thai Government, Thailand

Gold Medal of Excellent Academic Performance, *2002*, King Mongkut's University of Technology Thonburi, Bangkok, Thailand

Certificate and Medal of Excellent Academic Performance granted by His Royal Highness Crown Prince Maha Vajiralongkorn, *2002*,
The Engineering Institute of Thailand under H.M. the King's Patronage, Bangkok, Thailand

Certificate of Excellent Academic Performance, *1999*, The Foundation of Prof. Dr. Teab Neelanithi

Certificates of Excellent Academic Performance, *1999, 2000, 2001, and, 2002*, King Mongkut's University of Technology Thonburi, Bangkok, Thailand